This is to certify that the
dissertation entitled

LOCAL STRUCTURE STUDY OF DISORDERED CRYSTALLINE MATERIALS WITH THE ATOMIC PAIR DISTRIBUTION FUNCTION METHOD

presented by

XIANGYUN QIU

has been accepted towards fulfillment
of the requirements for the

Ph.D. degree in Physics

Major Professor's Signature

8/17/04

Date

LOCAL STRUCTURE STUDY OF DISORDERED CRYSTALLINE MATERIALS WITH THE ATOMIC PAIR DISTRIBUTION FUNCTION METHOD

By

Xiangyun Qiu

A DISSERTATION

Submitted to
Michigan State University
in partial fulfillment of the requirements
for the Degree of

DOCTOR OF PHILOSOPHY

Department of Physics and Astronomy

2004

ABSTRACT

LOCAL STRUCTURE STUDY OF DISORDERED CRYSTALLINE MATERIALS WITH THE ATOMIC PAIR DISTRIBUTION FUNCTION METHOD

By

Xiangyun Qiu

The employed experimental method in this Ph.D. dissertation research is the *atomic pair distribution function* (PDF) technique specializing in high real space resolution local structure determination. The PDF is obtained via Fourier transform from powder *total* scattering data including the important local structural information in the diffuse scattering intensities underneath, and in-between, the Bragg peaks. Having long been used to study liquids and amorphous materials, the PDF technique has been recently successfully applied to highly crystalline materials owing to the advances in modern X-ray and neutron sources and computing power. An integral part of this thesis work has been to make the PDF technique accessible to a wider scientific community. We have recently developed the rapid acquisition PDF (RA-PDF) method featuring high energy X-rays coupled with an image plate area detector, allowing three to four orders of magnitude decrease of data collection time. Correspondingly in software development, I have written a complete X-ray data correction program PDFgetX2 (user friendly with GUI, 32,000+ lines). Those developments sweep away many barriers to the wide-spread application of the PDF technique in complex materials. The RA-PDF development also opens up new fields of research such as time-resolved studies, pump-probe measurements and so on, where the PDF analysis can provide unique insights. Two examples of the RA-PDF applications are described: the distorted Ti2 square nets in the new binary antimonide Ti_2Sb and *in-situ* chemical reduction of CuO to Cu.

The most intellectually enriching has been the local structure studies of the colossal magneto-resistive (CMR) manganites with intrinsic inhomogeneities. The strong

coupling between electron, spin, orbital, and lattice degrees of freedom result in extremely rich and interesting phase diagrams. We have carried out careful PDF analysis of neutron powder diffraction data to study the local MnO_6 octahedral distortions. For example, in the updoped compound $LaMnO_3$, the Jahn-Teller (JT) transition around 750 K is characterized as distorted (JT active) to undistorted MnO_6 octahedra transition by the conventional crystallographic analysis. However, our PDF results show local MnO_6 octahedral distortions persist above the JT transition, and it is their random orientations that make the existing local distortions invisible to average structure analysis. The nature of the JT transition around 750 K is orbital order to disorder. Our first local structure study of the high temperature rhombohedral phase ($T \geq 1010$ K) additionally discovered the existence of locally JT distorted MnO_6 octahedra. More significantly, the range of the orbital order in the high temperature dynamic-JT phases, estimated from the crossover from the local to the average structure, is around 16 Å (~four MnO_6 octahedra), suggesting strong nearest neighbor JT anti-ferrodistortive coupling. In the bi-layered $La_{0.92}Sr_{2.08}Mn_2O_7$, we found the shape of MnO_6 octahedron changes from oblate (4 long, 2 short Mn-O bonds) to prolate (2 long, 4 short Mn-O bonds) as the material goes from type A anti-ferromagnetic to type CE charge ordered phase. This can be understood as the $d_{x^2-y^2}$ to $d_{(x,y)^2-r^2}$ orbital occupancy transition of the Mn^{3+} e_g electrons. Evidences for nano-scale inhomogeneities in the Mn^{4+} rich region of $La_{2-2x}Sr_{1+2x}Mn_2O_7$ ($0.54 \leq x \leq 0.80$) are also discussed.

To my loving and beloved,

Acknowledgments

It's such a thrill to be in this moment. This moment wouldn't have been possible without all the loving and beloved people around me. This moment wouldn't have any meaning without them. Each one of them is so special on the way to this moment. This moment belongs to them.

No words can express my greatest appreciation and respect to S. J. L. Billinge, my Ph.D. adviser. The past four and a half years spent in his group has been invaluable and extremely beneficial. I saw unlimited patience, unsparing guidance, and unfailing trust. Above all, he always strives to help me succeed.

I am full of gratitude to my thesis committee members, P. M. Duxbury, S. Tessmer, M. Thoennessen, and W. Repko for their devoted supervision. My highest respect to each of them. Consistent encouragement from S. D. Manhanti during my studies is greatly appreciated. My Ph.D. research benefits greatly from collaborations with P. J. Chupas, C. P. Grey, J. C. Hanson, H. Kleinke, C. Kmety, P. L. Lee, and J. F. Mitchell. Special thanks to each of them. It has been a great pleasure working with them. I have fortunately received magnanimous help from D. S. Robinson, S. Short, and D. Wermeille during experiments, to whom I am very very thankful. I also like to thank C. Malliakas for his help with sample characterizations.

Deepest appreciation goes to Th. Proffen who has helped me a great deal in almost all aspects of my research. V. Petkov and I-K. Jeong are cordially thanked for their generous help with X-ray experiments and data analysis. My most sincere salute to E. Bozin who taught me neutron experiments and gave his lavish encouragements along with his amusing accompany. It has been great fun working with M. Gutmann, P. F. Peterson, J. W. Thompson, A. Masadeh, and H. J. Kim. They are all great teachers and friends.

This moment is especially for my family. My father, my mother, all my family, I should have spent all the time with you all. This moment is especially for you.

Contents

List of Figures

List of Tables

Chapter 1

Introduction

1.1 Importance of the local structure

Materials are made up of atoms with charge and spins, and all carry some properties/functions. How atoms are assembled together refers to the atomic and magnetic structure of materials. The material structure and property/function relationship proves to be very important, as well as very interesting. For example, graphite (dark, soft, cheap) and diamond (transparent, hard, precious) are dramatically different materials. However, they are both made up of the same kind of carbon atoms and the only difference is their atomic crystal structures. What is more, the buckyball (C_{60}) and nanotube are made up of the same carbon atoms too. Certainly, there are many other cases than carbon, such as SiO_2 (quartz, sand, agate, onyx, opal), Al_2O_3 (sapphire, alumina), and so on. In a word, the structure property relationship is fundamental and its in-depth understanding is vital to manipulate the material function. Thus, precise knowledge of the structure is of paramount importance.

The importance of structure is further argued here by its most relevant energy scale in modern functional materials. Among the millions of ways that materials are used nowadays, with the exception of nuclear reactions in nuclear reactors and possibly a few others, the atoms in materials always keep their original elemental

species. For example, gasoline is burned to propel automobiles, but the number of carbon, oxygen, and hydrogen atoms stays the same before and after the chemical reaction; the magnetic moment of each storage grain in the hard disk is flipped, but the atoms comprising the disk never change their types. It is the structure that is closely related to their practical function. The bonding interaction between atoms gives the relevant energy scale (order of eV per atom) to our daily energy use. The practical functions of materials are often directly expressed material's macroscopic properties, such as the mechanical characteristics, electric conductivity, thermal conductivity, etc.. Though seemingly irrelevant, the microscopic structure is the underlying origin of many macroscopic properties.

The *local structure* in this context refers to the atomic neighboring environment at the length scale of nanometers or less. When the long range overall structure can be simply constructed from the local structure by periodic assembly, this results in crystalline materials with perfect long range order; for example, diamond, quartz, and sapphire. Preparation of perfect crystals has received significant amount of efforts as they often possess astonishing properties such as mechanical strength. However, one growing modern trend is that, in many interesting functional materials, the local structure does not order perfectly long range as in crystalline materials. We are observing that modern functional materials are getting more and more structurally complex and disordered. Their properties of both scientific and technological interest are often exploited and tuned by either intrinsic disorder or extrinsic disorder induced by chemical doping, mesostructure patterning, etc.. For example, the high temperature superconducting cuprates reach the highest transition temperature with optimal levels of defects induced by chemical doping. Therefore, detailed knowledge of local structure (getting to know the neighbors) is crucial in modern times to understanding the properties of complex and disordered materials.

1.2 Experimental methods of local structure determination

Let us first look at the structure determination of crystalline materials, where the local structure is the same as the average (overall) structure. There exists in crystals a periodic box called the unit cell of the lattice. The long range ordered stacking of the unit cells makes it very convenient and effective to look at the structure's Fourier counterpart in reciprocal space. In fact, a reciprocal lattice uniquely corresponds to a specific lattice structure. Measuring the reciprocal lattice with diffraction experiments [1] will lead to solution of the crystal structure in real space. Father and son Bragg first demonstrated crystal structure solution by the means of X-ray diffraction [2, 3, 4] and won the Nobel prize in 1915 for their pioneering work. Ever since then, the analysis of Bragg peak intensities (the reciprocal lattice reflections) for crystal structure determination has become routine and the almost exclusive experimental method for this purpose, giving rise to conventional crystallographic analysis. This mature technique is still enjoying great success in areas such as the protein crystallography.

Probing the local structure in non-perfect crystalline materials proves very challenging to conventional crystallography. The assumption that Bragg peaks contain all structural information does not hold in the presence of disorder and/or local distortions. This is because the local deviations from perfect long range order result in diffuse scattering in-between and underneath the Bragg peaks in reciprocal space other than the reciprocal lattice. Neglecting those diffuse scattering intensities results in loss of the local structure information. Other experimental approaches have been invented to probe the local structure (neighboring surrounding environment, for example, the atomic pair distribution function (PDF) method [5] employed in this thesis. Let us first briefly review a few other approaches in the following.

Extended X-ray Absorption Fine Structure (EXAFS) The measured quantity in one EXAFS experiment is the sample absorption coefficient as a function of the incident X-ray energy usually ranging between 20 and 800 eV above the K or L absorption edge of one specific constituent element [6, 7]. Either the transmitted photons or the fluorescence intensities can be measured for this purpose. How the local structure information is contained in the absorption coefficient can be understood qualitatively as the following. The incident photons excite either the K or L shell core electrons into the continuum as a consequence of the photoelectric effect when the photon energy is closely above the absorption edge. The excited electron will carry some kinetic energy which is the difference between the photon energy and the absorption threshold of the probed atomic shell. As the photoelectron energy ($\geq$ 20 eV) is large compared with its interaction energy with the surrounding atoms ($\sim$ 3 eV), simple plane wave approximations can be made on those photoelectrons with the surrounding atoms taken as perturbations. The cross section of the photoelectric effect is then proportional to the wave function overlap between the photoelectron plane wave and the atomic K or L core level states. While the atomic core levels are little affected by the neighboring atomic environments, the photoelectrons are scattered by the surrounding atoms. Therefore, the final state of the photoelectron is modified by the backscattered electrons, and the backscattered electron waves can either add or subtract depending on their relative phases. As the wavelength of the photoelectron simply follows the de Broglie relation $\lambda = \frac{h}{p}$, their relative phases directly depend on the distance between the probed atom and its neighbors, i.e. half of the traveling distance of the backscattered electron. Oscillations in the sample absorption with incident photon energy are then expected, as the photoelectron energy, thus the wavelength λ, and the relative phases, are varied. To properly extract the local structure information

from EXAFS data, many other complications have to be taken into considerations, such as backscattering phase shift, finite life time of electron states, and multiple electron scattering events.

It is worthwhile to mention its surface version SEXAFS. Instead of measuring either transmitted or fluorescent photons, the photoelectron yield from the surface is measured. This also requires the experiments to be performed in ultra-high vacuum (10^{-10} Torr).

X-ray Absorption Near Edge Structure (XANES) The experimental aspects of XANES are close to EXAFS except that the covered absorption spectrum range is between the threshold and the point at which EXAFS begins [7]. This range is poorly defined, and taken usually as up to 50 eV above the threshold. The XANES method is very sensitive to local electronic state changes. As the photoelectrons in XANES measurements have low energy, the theoretical considerations are rather different. The focus has been the electronic structure of the low-lying extended excited states. The interaction between the photoelectrons and atoms is also significantly stronger, thus multiple scattering events become significant. Though the oscillating amplitude in the XANES region is generally significantly larger than in the EXAFS region, extensive theoretical efforts are still required for detailed quantitative analysis [7].

Nuclear Magnetic Resonance (NMR) Within the present context, the NMR technique probes the chemical environment of the specific nucleus under resonance. During an NMR measurement, the energy of different nuclear spin states are shifted by an amount proportional to their net spin by the external static magnetic field. Transitions between the different spin states can be initiated by a secondary oscillating magnetic field by either changing its frequency or the amplitude of the applied static magnetic field. The zero static field NMR

method is called nuclear quadrupole resonance (NQR). The important quantity coming from NMR measurements is called chemical shift, which is defined as the difference between the resonance frequency of the nucleus and a standard [8], relative to the standard. One origin of the chemical shift is from the electrons around the nucleus. The applied magnetic field also causes the electrons to circulate about the direction of the applied magnetic field. This circulation causes a small magnetic field at the nucleus which opposes the externally applied field (in some cases, it enhances the external field). This shifts the nuclear resonance frequency, which is proportional to the magnetic field strength at the nucleus. Therefore, the magnitude of the chemical shift carries information about the surrounding electrons, thus the local chemical environment, such as valence, bonding, geometry, etc.. As the probed nucleus is required to have net spin, isotope substitution is sometimes necessary.

1.3 The atomic pair distribution function technique

As suggested by its name, the atomic pair distribution function (PDF), $G(r)$, tells the probability of finding *atomic pairs* separated by the real space distance r. It should be stressed that the PDF of interest is radially averaged and is a one dimensional function. To obtain the $G(r)$ for a given a structure, we first sit on one atom i, then look out for neighbors. A peak is assigned for every atom j found at the position corresponding to the inter-atomic distance r_{ij}, and zero everywhere else. Then we repeat the same procedure over all atoms, and average all obtained curves to get the total $G(r)$ of the structure. Another way to get the $G(r)$ is to first obtain the atomic radial density function $n(\vec{r})$ with an arbitrary origin. The convolution of $n(\vec{r})$ with

itself results in the PDF. The mathematical definition of the PDF is

$$\begin{aligned} G_c(r) &= \frac{1}{r}\sum_i\sum_j\left[\frac{b_i b_j}{\langle b\rangle^2}\delta(r-r_{ij})\right] - 4\pi r\rho_0 \\ &= 4\pi r[\rho(r)-\rho_0], \end{aligned} \tag{1.1}$$

where r_{ij} is the distance between atoms i and j; the value b_i is the scattering length for atom i; $\langle b\rangle$ is the average scattering length over all atoms; and ρ_0 is the number density. The $\rho(r)$ here is equivalent to the spherical average of $\int n(\vec{r'})\cdot n(\vec{r}-\vec{r'})d\vec{r'}$. Though less intuitive than the radial density function $n(\vec{r})$, the PDF, $G(r)$, is the directly measurable quantity from powder diffraction experiments.

The path from a powder diffraction experiment to the $G(r)$ can be conceptually understood in the following way. We will first concentrate on one single grain, then do the spherical averaging. Given the radial density function $n(\vec{r})$ of the scatterer, from the kinematic scattering theory in the Born approximation, the scattered wave at momentum transfer $\vec{Q}$ takes the form of $F(\vec{Q}) = \int n(\vec{r})e^{i\vec{Q}\cdot\vec{r}}d\vec{r}$, which is actually the Fourier transform of $n(\vec{r})$. Well known as the phase problem in crystallography, the measurable quantity is the scattered intensity $I(\vec{Q}) = |F(\vec{Q})|^2$, where the phase information is lost. We cannot directly and uniquely recover the atomic density function $n(\vec{r})$. Now, we can rewrite the $I(\vec{Q})$ as $F(\vec{Q})\cdot F^*(\vec{Q})$, where $F^*(\vec{Q})$ is in fact the Fourier transform of the real function $n(-\vec{r})$. Then based on the convolution theorem, the Fourier transform of $I(\vec{Q})$ is the convolution of the Fourier transforms of $F(\vec{Q})$ and $F^*(\vec{Q})$. This is $\int n(\vec{r'})\cdot n(\vec{r'}-\vec{r})d\vec{r'}$. Then we do the spherical averaging due to the random grain orientation in powders. This will result in the one dimensional form of $G(r)$. Therefore, the PDF can be obtained by Fourier transforming the measured scattering intensities. The measured scattering intensities can be expressed

as

$$S(Q) = \int_{-\infty}^{+\infty} \frac{b_i b_j}{\langle b \rangle^2} \rho(r_{ij}) \frac{\sin(Q r_{ij})}{Q r_{ij}} d\vec{r_{ij}} = \frac{1}{2} \int_0^{\infty} \frac{b_i b_j}{\langle b \rangle^2} 4\pi r_{ij} \rho(r_{ij}) \frac{\sin(Q r_{ij})}{Q} dr_{ij} \quad (1.2)$$

from the Debye scattering equation [9]. The PDF can be directly obtained via a sine Fourier transform: $G(r) = \frac{2}{\pi} \int_0^{\infty} Q[S(Q) - 1] \sin Qr \, dQ$.

The key difference between the PDF method and conventional average structure analysis of powder diffraction data is how to treat the diffuse scattering intensities in-between and underneath the Bragg peaks. The Bragg peaks come from the long range ordered structure, while the diffuse scattering intensities come from local/temporal deviations from the long range ordered structure. The PDF technique takes into account both, as evident from the equations above, while conventional average structure analysis only looks at the Bragg peaks. Therefore, the PDF method is capable of probing both the local and average structure. This combination of local and average studies from the same scattering data represents a clear advantage for a wide range of applications. For example, with the presence of Bragg peaks in the case of crystalline materials, the PDF technique and conventional analysis are complementary while the former provides additional information about the local structure. However, in the case of nano-crystalline and non-crystalline materials, with few or no Bragg peaks, only the PDF technique is applicable.

Local structural information is intuitively contained in the low-r PDF peaks. Thus, the real space resolution is an important experimental factor to resolve closely neighboring peaks. PDF peaks are first broadened by the atomic thermal motions. Second, the finite measurement range also broadens the peaks coming from the termination effects [10]. High real space resolution requires usually extended Q range ($\geq$ 25.0 Å^{-1}) data to be collected, and low temperatures if possible. Other than identifying low-r peak positions (existing atomic pair distances), extracting the peak width and area reveals further details about the local distortions and number of neighbor-

ing atoms as well. The average structural information is usually recovered from the PDF structure model refinements using the non-linear least square regression fitting program PDFFIT [11]. The agreement between the average structure and experimental $G(r)$ provides a good check for the possible existence of local disorder, and hypothetical distorted structure models can then be fit to improve the agreement. Knowledge of the detailed local and average structures often serves as the basis of many theoretical calculations of material properties. For example, the bond valence sum can be computed to investigate the strength of chemical bondings. Electronic band structure calculations can be carried out if necessary to check whether the obtained structure gives macroscopic properties consistent with other types of measurements. For more details about the PDF technique, please turn to a recent book by Egami and Billinge [5].

1.4 Recent advances in the PDF method

Having long been used to study liquids and amorphous materials [12, 13, 14, 15], the PDF technique has been recently successfully applied on nano-crystalline and crystalline materials [16, 17], owing to advances in modern x-ray and neutron sources and much improved computing power [5]. Why does the PDF technique require those? The first is the wide Q range necessary for highly crystalline materials whose coherent scattering extends to the high Q region. The high energy high flux synchrotron sources and intense spallation sources made quantitative PDF measurements possible in a reasonable amount of data collection time. Secondly, the intensive data post-processing requires high speed computers, which have become widely available over the last decades.

PDF analysis of perfect crystalline materials, such as Si, Ni, not only obtain the average structures in quantitative agreement with conventional crystallographic methods [18], but also give additional information about the correlated motions be-

tween neighboring atoms [19, 20]. Proffen *et al.* have successfully applied the PDF method to probe the chemical short range order in Cu_3Au [21]. Complementary to the average structure analysis, Billinge *et al.* and Bozin *et al.* have applied the PDF technique extensively to study the local disorder and inhomogeneities in the highly crystalline colossal magneto-resistive manganites and high temperature superconducting cuprates [22, 23, 24, 25, 26]. When the long range crystallinity gradually fades such as in nano-crystalline and non-crystalline materials, the reciprocal space approach taken by the conventional crystallographic methods becomes less and less effective. However, this decrease of structural coherent length has little effect on the PDF technique where no long range periodicity is assumed. For example, Petkov *et al.* have shown that local and intermediate structure can be obtained from PDF data when a certain level of local atomic order is preserved [27, 28, 29, 30]. As for non-crystalline materials such as liquids, glass, and amorphous materials, the very local structure only persists and the Angstrom scale becomes the only meaningful length scale. Here, the PDF technique has been the method of choice for structure investigations [31, 1, 32]. At present, much higher real space resolution is being achieved [33, 34, 35]. Sophisticated and intensive modeling methods, such reverse Monte Carlo (RMC) and potential based regression algorithms, have also become popular to gain more insight [36, 37, 38, 39, 40].

1.5 Outline of this thesis

Investigation of the local structure employing the PDF technique is the the central theme of this thesis work, covering both technical developments and scientific applications.

Chapter 2 will describe a recent development of a new way to collect PDF data: rapid acquisition pair distribution function (RA-PDF) method, where the coupling of high energy X-ray with an area detector leads to three orders of magnitude decrease

of data collection time.

Chapters 3 and 4 focus on the high resolution PDF analysis of neutron powder diffraction data on two manganite systems: undoped $LaMnO_3$ and bi-layered $La_{2-2x}Sr_{1+2x}Mn_2O_7$, respectively. The significance of local Jahn-Teller distortions will be emphasized, and their strong influence on the electronic, and magnetic degrees of freedom will be discussed.

Chapter 5 will demonstrate a few applications of the RA-PDF method, e.g., resolving the distorted square Ti nets in Ti_2Sb, and the *in-situ* chemical reduction of CuO to Cu.

Chapter 6 summarizes the thesis and discusses some future work.

Appendix A describes the the experimental aspects and post-data processing of the RA-PDF method in detail.

Chapter 2

The Rapid Acquisition Pair Distribution Function Method

2.1 Introduction

In recent times, new materials are emerging at unprecedented rates, and one growing trend is that their structures become more and more disordered and complex. It is of great current interest to characterize those nanocrystalline material structures effectively and routinely. However, the long range structural coherence length at nanometer scales challenges conventional crystallographic analysis. As reviewed by Billinge and Kanatzidis [16], the PDF technique is a promising candidate as evidenced by its successful application to solve structures with different levels of complexities [5, 16]. However, conventional PDF measurements are very slow and generally take more than eight hours, even at a third generation synchrotron or intense spallation neutron sources. This, coupled with the novelty of the approach and the somewhat intensive data analysis requirements, has prevented widespread application of the technique in areas such as nano-materials. This chapter will introduce a recent development - the rapid acquisition PDF (RA-PDF) method where the data collection time is reduced by three to four orders of magnitude. A new program PDFgetX2 [41] will

also be briefly described as a user friendly program to obtain the PDF from X-ray powder diffraction. I will show that high-quality medium-high resolution PDFs ($Q_{max} \leq 35.5$ Å^{-1}) can be obtained in a few seconds of data collection time using a two-dimensional (2D) image plate (IP) detector with easy to use programs. These developments open the way for more widespread application of the PDF technique to study the structure of nanocrystalline materials. They also open up the possibility for experimentally demanding experiments to be carried out such as time-resolved studies of local structure.

2.2 Description of the modern PDF experiments

Let us first briefly review modern PDF experiments. As we are trying to resolve inter-atomic distances to one tenth of an Angstrom resolution, this sets the relevant wavelength of the probing wave to use. From the De-Broglie wavelength equation $\lambda = \frac{h}{p}$ with λ of 0.2 Å, the corresponding energy scales are around 60.0 keV for X-rays ($E = \frac{12.0398}{\lambda(A)}(keV)$), 2.04 eV for neutrons ($E = \frac{81.81}{\lambda^2(A)}(meV)$), and 3.76 keV for electrons ($E = \frac{150.4}{\lambda^2(A)}(eV)$). Electrons have seldom been the choice for bulk studies due to their short penetration depth (strong scattering). High energy X-rays and neutrons have much better penetrating power suitable for bulk studies, which also means their interactions with matter are rather weak. Thus most quantitative experiments need to be performed at either high flux synchrotron source or intense neutron spallation sources, and they are slow because of the weak interactions. X-rays and neutrons are complementary probes for PDF studies, providing different contrasts for the different elemental species in the structure. For example, X-rays are scattered by the electrons, thus heavy atoms with more electrons are better "seen" by X-rays [5].

2.2.1 Neutron powder diffraction

In spallation neutron sources, neutrons are first generated by bombing the target materials (mercury, tungsten, etc.) with high energy charged particles (H^+). The hot neutrons are cooled down by a constant temperature moderator (chilled water, liquid methane, etc.). The neutrons delivered to the sample consist of two major components, the thermal neutrons in equilibrium with the moderator, and the "hotter" epithermal neutrons not completely equilibrated. Therefore, you can imagine a train of neutrons with different velocities hit the sample and get scattered in all directions. The scattered neutrons are recorded by the installed detector banks covering wide solid angles. Those neutrons are also timed at the beginning and end of the flight, so that their speeds can be computed given the known traveling distances, and thus the wavelength λ via the De-Broglie wavelength equation. The momentum transfer Q simply follows from $Q = \frac{4\pi}{\lambda}\sin\theta$, where 2θ is the scattering angle. This gives the method name of neutron time of flight (TOF) method. Neutrons in spallation sources are pulsed with a repetition rate from 20 to 50 Hz. It is noteworthy that it is mostly those epithermal neutrons that give the important high Q data. The program PDFgetN [42] provides a user friendly graphic user interface (GUI) to obtain the PDF from neutron powder diffraction data.

Even with multiple detector banks, neutron experiments still take around 6 hours, and this is for a large amount of sample, more than 6 grams. Compared with X-rays, the neutron incident flux normally achieved is three orders of magnitude lower. One way to improve the data collection is to increase the covered solid angle of the detector banks, as in the upgrade of the neutron powder diffractometer (NPD) to NPDF at the Lujan center at Los Alamos National Laboratory [43]. The newly upgraded NPDF gives the state of the art PDF data collection time of around 2 to 3 hours available in the USA. We can also boost the flux of the neutron source for the same purpose. The new spallation neutron source (SNS) project, still under construction,

is expected to significantly boost the data throughput rate. However, the reduction of data collection time will be partially canceled by the smaller sample size used in future neutron studies.

2.2.2 X-ray powder diffraction

In synchrotron sources, electromagnetic radiation due to the acceleration of cycling electrons traveling at relativistic speeds give a wide energy spectrum of X-rays. Wigglers and insertion devices are used in situations to enhance the brightness at certain photon energies. Monochromaters are used to select the desired wavelength X-rays. High energy X-rays, e.g. $\geq$ 100 keV, can be routinely achieved at third generation synchrotron sources such as the Advanced Photon Source (APS) at Argonne National Laboratory. Multiple slits are used to confine the beam to dimensions in consideration of either sample sizes or other reasons such as experimental resolution, background, etc.. With monochromatic X-rays, the scattering angle 2θ is scanned step by step by moving a point solid state detector (SSD). Again from the formula $Q = \frac{4\pi}{\lambda}\sin\theta$, the scattering intensity I versus Q data are collected. Similar to neutron PDF data processing, many steps have to be performed to obtain the PDF from X-ray powder diffraction data. For this purpose, the menu driven program PDFgetX [44] has been used.

Conventional PDF X-ray measurements with a SSD normally take more than 8 hours, though the data collection time at a single 2θ point usually takes less than 10 seconds. As the wide Q range required by PDF analysis needs easily more than 2000 points, it is the step by step scanning that significantly changes the experimental data collection time scale. Considerable flux increase will be expected when the fourth generation free electron laser X-ray source becomes available. However, the data collection time then will possibly be limited by the time taken to move and stabilize the detector. One alternative approach is to use multiple point detectors, or area

detectors. Use of multiple detectors has been tested in our group and others. First, the experiment becomes rather difficult technically, e.g. even the accurate measurement of sample to detector distance is different for a point detector. And also different detector elements are found hard to work in a consistent way due to various electronic issues. Attempts with an area detector such as an image plate have also been realized in our group with the Debye-Scherrer geometry [45]. The counting rate is greatly improved. However, the limiting factor becomes the time cost to take out the image plate, scan it, and then put it back in. Also, signal-background ratio issues were never statistically resolved. The RA-PDF technique developed here makes use of a planar 2D image plate used in a transmission mode.

2.3 Use of the image plate as an X-ray detector

The detection media of an image plate (IP) is one layer of very small crystalline grains of photo-stimulable phosphor mixed with organic binders. The grain size is about 5 μm; the layer thickness is usually around 150 μm. There is usually a protective layer (about 10 μm) on the top and one support layer on the bottom (about 250 μm). A polyester backing plate is often used to make it reusable and easy to handle as a flexible plastic plate. The IP's sensitive surface can be easily identified by its all-blue-white or all-white appearance, while the backing side is usually black or gray.

2.3.1 Principle of X-ray image plate detection

The photo-stimulable phosphor used nowadays is BaF(Br,I):Eu^{2+} (previously it was BaFBr:Eu^{2+}) [46]. This material is capable of storing a fraction of the absorbed X-ray energy, and emitting photo-stimulated luminescence (PSL) later when stimulated by visible laser light. The mechanism of the PSL is illustrated by the energy level scheme of BaFBr:Eu^{2+} shown in Fig. 2.1. The energy level of interest is the Eu^{2+} ground

state, 6.5 eV below the conduction band, and the vacant $F^+(Br^+, I^+)$ centers 2.0 eV below the conduction band. The ground state has Eu^{2+} and vacant F^+ centers. The incident X-ray will pump electrons from the valence band to the conduction band. Despite being a complicated process, the X-ray irradiation results in a certain number of Eu^{3+} and F pairs proportional to the absorbed X-ray energy. The F centers are caused by the absence of halogen anions from their designated positions in the lattice. The energy trapping state of F centers is meta-stable with a long lifetime. However, the trapped electrons can be easily excited by visible light ($\geq$ 2 eV) to return to the conduction band. One of the occurring processes is the recombination of Eu^{3+} with one election to Eu^{2+}, along with the emission of a photon of 3.2 eV (blue light). A red He-Ne laser is usually used for read-out. Its wavelength (632.8 nm) is considerably separated from the PSL wavelength (390 nm). A conventional high-quantum-efficiency photo-multiplier tube (PMT) is used to collect the photo-stimulated photons. The signal is then amplified and digitalized to be processed by computers. The remaining F centers in the phosphor after read-out can be further erased by exposing to visible light. In practice, it is more efficient to bleach it with a powerful halogen lamp (500W).

2.3.2 Characteristics of image plate detectors

The performance of the image plate as an X-ray area detector has been reviewed by Amemiya and others [48, 46, 47, 49, 50, 51, 52, 53] in great detail. Here we briefly summarize those characteristics for completeness.

Detective quantum efficiency The definition of detective quantum efficiency (DQE) is $DQE = (S_o/N_o)^2/(S_i/N_i)^2$ where S is signal and N is noise (the standard deviation of the signal), and subscripts o and i refer to the output and input, respectively. As scattering events are random following the Poisson distribution, the $(S_i/N_i)^2$ term is just the S_i. The background noise level of the IP

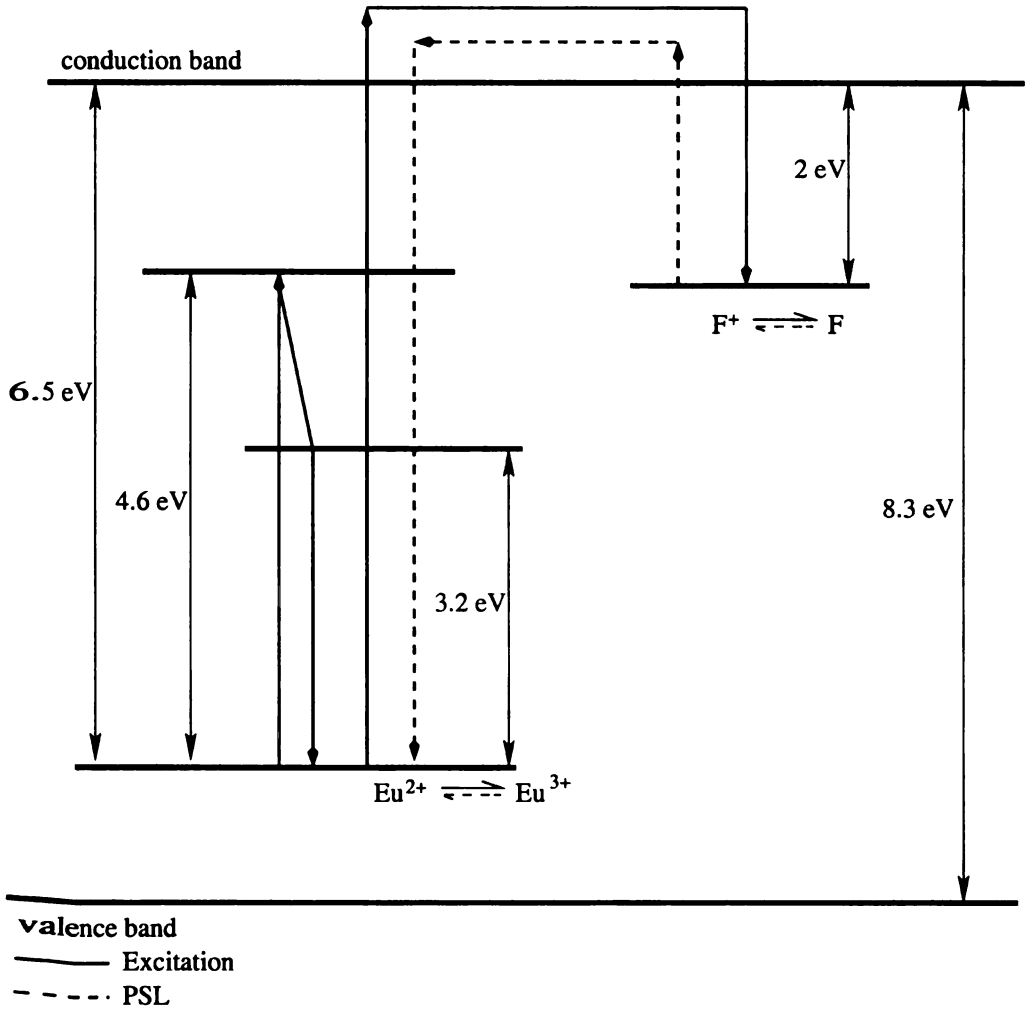

Figure 2.1: Energy level scheme of image plate phosphor material BaFBr:Eu^{2+} proposed in Ref. [47]. Arrows indicate the excitation and PSL process as suggested by Takshashi *et al.* [48].

is usually less than 3 X-ray photons/(100 μm)^2, which in practice largely depends on the noise level of the IP readout system. The relative uncertainty of the IP deviates from an ideal detector at high exposure levels ($\geq$ 100 X-ray photons/(100 μm)^2). The "system fluctuation noise" saturates the relative uncertainty of the IP results around the 1% level. The origin of the system fluctuation noise includes non-uniformity of absorption, non-uniformity of the color-center density, fluctuation of the laser intensity, non-uniformity of PSL collection, and fluctuation of the high-voltage supply to the PMT.

Dynamic range and linearity of the IP response The dynamic range refers to the detectable weakest and strongest signal with acceptable distortion. One dimensionless definition is taken as the ratio between the maximum counts in the linear regime and the lowest detectable signal (determined by the intrinsic noise of the detector system). The IP has rather good dynamic range of 10^5:1, with linear response range from 8×10^1 to 4×10^4 photons/(100 μm)^2. The error rate is less than 5%. Sometimes, two sets of PMTs are necessary to cover the entire dynamic range of the IP.

Spatial resolution and active area size The determining factor of the spatial resolution of the IP is the laser-light scattering in the phosphor during the readout. The laser-light scattering originates from a mismatching of the refractive indices at the boundaries of phosphor crystal grains. When the IP is read with a 100 μm square laser size, the spatial resolution is limited by the linear spread function with 170 μm full width at half maximum (FWHM). The point spread function of IP systems has been studied by Bourgeois *et al.* [54] in detail. The active area size of the image plate is rather important for PDF studies which need large IPs. Commercially available IPs have various standard sizes ranging from 127$\times$127 mm^2, 201$\times$252 mm^2, to 201$\times$400 mm^2. The largest automated IP system currently contains the 345 mm diameter IP disk (MAR345).

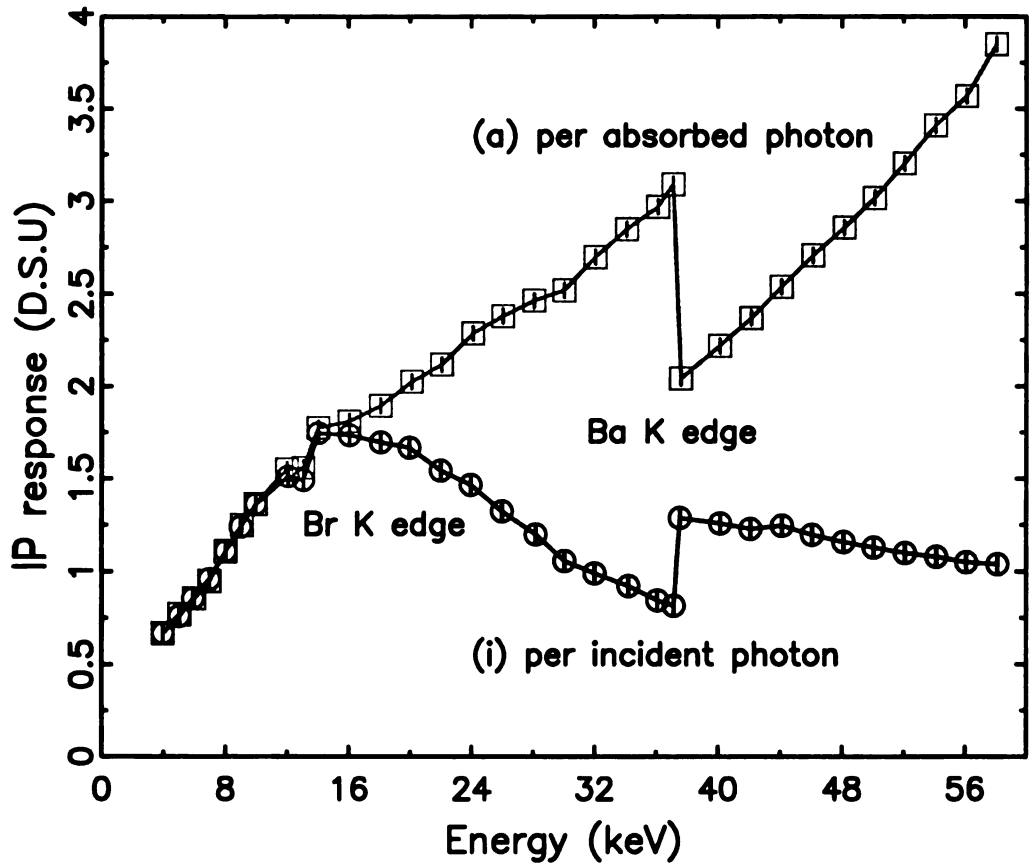

Figure 2.2: The IP response as a function the the energy of an X-ray photon. (i) is the IP response per incident X-ray photon. (a) is the IP response per absorbed X-ray photon. The unit of the ordinate corresponds toe the background noise level of the IP scanner (the data were digitized from the the corresponding figure in reference [55]).

Energy dependence The measured intensity on the IP is proportional to the deposited energy in the phosphor layer. This depends on the absorption efficiency per incident photon and the deposited energy of one absorbed photon. Unfortunately, the IP response is energy dependent, and its energy dependence is shown in Fig. 2.2 from 4.0 to 60.0 keV. We are only concerned with the IP response per incident photon (lower curve). Except for the discontinuity at the Ba K edge, the detection efficiency decreases with photon energy in the high energy regime of our interest. This necessitates an energy dependent detection efficiency correction discussed later in this chapter.

Fading and other factors The IP stores the absorbed energy in the meta-stable F centers and thus will fade with time after exposure. Exposing the IP to visible light or high temperature will expedite the fading. At room temperature, the IP is usually stable within one hour. The fading lifetime does not depend on the X-ray energy during exposure, as it is the F centers that store the energy. The surface roughness and the non-uniformity of the IP is about 1-2%. A calibration image is usually obtained by exposing the IP to a flood field from a radioactive source, and then used to correct the recored images. In principle, the IP, being an integrating-type counter, is not counting rate limited. However, extremely intense X-rays seem to cause permanent damage to the phosphor layer. With the exercise of common precautions, the IP has proved to be a very reproducible and reusable X-ray area detector.

To summarize, the IP detector system meets various requirements of X-ray area detectors. They are, high detective quantum efficiency, a wide dynamic range, a linearity of response, a high spatial resolution, a large active area size, and a high counting rate capability.

2.3.3 The IP and PDF method

Recent developments have shown the utility of 2D detector technology in scattering studies of liquids. A recent report by Crichton *et al.* [56], has made use of integrated two-dimensional IP data for *in-situ* studies of scattering from liquid $GeSe_2$. This study, and others more recently, demonstrate the feasibility of using IPs for diffuse scattering measurements though the measurements have been limited in real-space resolution, with $Q_{max} \leq 13.0$ Å^{-1} [57, 58], making them less suitable for the study of crystalline and nanocrystalline materials. Image plates have also been successfully used to study diffuse scattering from single crystals [59]. A Debye-Scherrer camera utilizing IPs has also been tested in our group and shows promise for lower energy

X-ray sources such as laboratory and second generation synchrotron sources [45].

Successful application of IP technology to the measurement of quantitatively reliable high real-space resolution PDFs requires that a number of issues be resolved. For example, it is necessary to correct for contamination of the signal from Compton and fluorescence intensities and for angle and energy dependencies of the IP detection efficiency [55, 60]. Here we show that high quality medium-high real-space resolution PDFs can be obtained by applying relatively straightforward corrections. As expected, the quality of the PDFs is lower in samples comprising predominantly low atomic-number elements. Nonetheless, even the PDFs of these samples prove adequate. Further quality studies were also carried out to investigate the RA-PDF capabilities. We also compared the IP data with the conventional solid state detector data to verify that quantitatively reliable structure information can be obtained from the RA-PDF method.

2.4 RA-PDF experiment

Our first PDF experiment with an IP detector took place in October, 2002. Two essential components were key to the success of this first experiment. One was the experience with the online image plate detector, mainly from Dr. Peter Chupas in Prof. Clare Grey's group at Stony Brook University, Dr. Jon Hanson from Brookhaven National Lab, and Dr. Peter Lee from Argonne National Lab. The other was the expertise with the PDF technique from our group. Part of the results have been published [61]. Technical descriptions, together with the experimental setup diagram, can be found in Appendix A.

2.5 The proof of principle study

2.5.1 Description of the experiments

All diffraction experiments for our first study were performed at the 1-ID beam line at the Advanced Photon Source (APS) located at Argonne National Laboratory, Argonne, IL (USA). High energy X-rays were delivered to the experimental hutch using a double bent Laue monochromator capable of providing a flux of 10^{12} photons/second and operating with X-rays in the energy range of 80-100 keV [62]. Two energies of X-rays were used for the experiments, 80.725 keV (0.15359 Å) and 97.572 keV (0.12707 Å), with the 80.725 keV experiments being performed first. In the optics hutch, a gold foil was installed after the monochromator between two ion chambers, attenuating the flux of the beam by approximately 30%. Calibration of energy at 80.725 keV was achieved using the gold absorption edge as the reference.

A Mar345 image plate camera, a round disk with a usable diameter of 345 mm, was mounted orthogonal to the beam path, with the beam centered on the IP. When operating with 80.725 keV X-rays, a LaB_6 standard was used to calibrate the sample to detector distance and the tilt of the IP relative to the beam path, using the software Fit2D [63, 64]. For calibration of the IP, the wavelength was fixed to represent the gold absorption edge, 0.15359 Å, at 80.725 keV. When the X-ray energy was increased from 80.725 to 97.572 keV, the sample to detector distance was first fixed at the value determined at the Au edge and the wavelength was calibrated using the standard LaB_6. The IP camera was then moved closer to the sample and the new sample to detector distance was obtained from refinement by fixing the wavelength at 0.12707 Å. Sample to detector distances of 317.28 and 242.12 mm were used for collection of data with measured Q_{max} of 21.0 $Å^{-1}$ and 30.0 $Å^{-1}$, respectively. In practice, Q_{max} of 18.5 $Å^{-1}$ and 28.5 $Å^{-1}$ were used due to the corrupted data near the IP edges. The beam stop is a solid tantalum cylinder (diameter 3.1 mm), with an

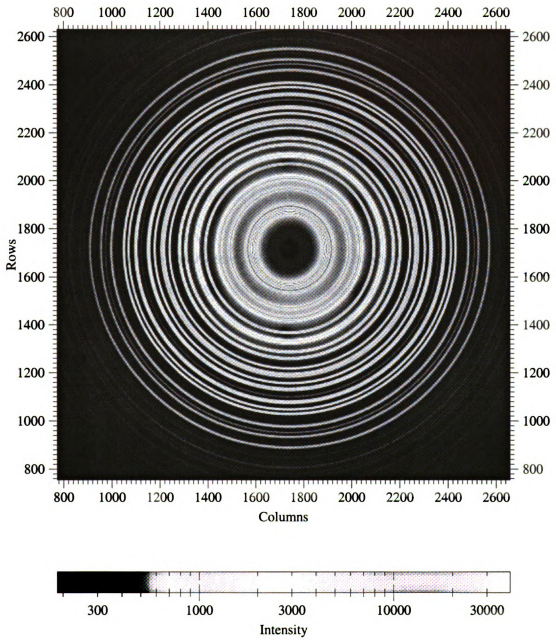

Figure 2.3: (color) Two dimensional contour plot from the Mar345 Image Plate Detector. The data are from nickel powder measured at room temperature with 97.572 keV incident X-rays. The concentric circles are where Debye-Scherrer cones intersect the area detector.

indentation machined to a depth of approximately 2 mm to accept the beam. With a beam stop to sample distance of approximately 150 mm, the scattering angle blocked by the beam stop is less than 1 degree, dependent upon sample to detector distance. This gives a Q_{min} limited to approximately 1 $Å^{-1}$. With our beam stop to sample distance of approximately 150 mm, the scattering angle blocked by the beam stop is less than 1 degree. This gives the energy dependent Q_{min} limited to approximately 0.6 $Å^{-1}$ with 80.725 keV X-rays. In many crystalline materials with small unit cells this is not a problem. When Bragg-peaks are lost at low-Q due to this limit, a weak, long-wavelength oscillation results in $G(r)$, which is not fatal but, ideally, is to be avoided.

The methods used to synthesize α-AlF_3, $Bi_4V_2O_{11}$ and $Bi_4V_{1.7}Ti_{0.3}O_{10.85}$ have been reported elsewhere [65, 66]. Ni was purchased from Alfa Aesar (99.9%, 300 mesh) and was used as received. Fine powders of all the samples were measured in flat plate transmission geometry, with thickness of 1.3 mm packed between kapton foils. The beam size on the sample as defined by the final slits before the goniometer was 0.4 mm $\times$ 0.4 mm. Lead shielding before the goniometer, with a small opening for the incident beam, was used to reduce background. All raw data were integrated using the software Fit2D and converted to intensity versus 2θ (the angle between incident and scattered X-rays). An example of the data from nickel measured at 97.572 keV is shown in Fig. 2.3. The integrated data were then transferred to a home-written program, PDFgetX2 [41], to obtain the PDF.

Distortions in intensities when using flat IPs have been addressed in single crystal crystallography, and arise from the fact that IPs are of a finite thickness, often between 100-200 microns [60, 67]. At the high energies ($\geq$ 60 keV) needed to measure $S(Q)$ to a high value of Q with commercial IP cameras, absorption of the X-ray photons by the phosphor is very small and most of the X-rays travel straight through the phosphor. The absorption, and thus the measured intensity, is then dependent on the path

length of the beam through the IP phosphor at all incident angles and can easily be corrected [60]. This oblique incidence correction assumes that the correction is equal in all directions, thus, care was taken to ensure the IP was mounted orthogonal to the beam. The attenuation of scattered photons after the sample, due to air absorption, is angle dependent. This effect is negligible due to the very small absorption of the high energy X-rays between the sample and the detector and is ignored. The count time is always adjusted to ensure that there are no saturated pixels in the detector. Standard corrections for multiple scattering, polarization, absorption, Compton scattering, and Laue diffuse scattering were also applied to the integrated data to obtain the reduced structure function $F(Q)$ (Fig. 2.4(a)). Direct Fourier transformation gives the pair distribution function $G(r)$ (Fig. 2.4(b)). The average structure models were refined using the profile fitting least-squares regression program, PDFFIT [11]. Rietveld refinements of the data were performed with GSAS [68].

2.5.2 Early results

All the experimental data from samples Ni, α-AlF_3, $Bi_4V_2O_{11}$ and $Bi_4V_{1.7}Ti_{0.3}O_{10.85}$ show excellent counting statistics over the entire Q range, reflecting the significant advantage obtained by extracting 1D data sets by integration of a 2D area detector. Image plate exposure time, ranging from one second (Ni) to 10 seconds (α-AlF_3), was chosen carefully for each sample to maximize the dynamic range of the IP without saturating the phosphor on the Bragg peaks. Data collection was repeated a number of times until acceptable statistical errors were observed at high-Q in the reduced structure functions, as shown in Figures 2.4(a), 2.5(a), and 2.6(a). All the PDFs, $G(r)$, show either superior or acceptable qualities.

The first example, shown in Fig. 2.4, is from standard Ni powder with Q_{max} of 28.5 $Å^{-1}$. The Ni PDF, $G(r)$, in Fig. 2.4 (b) appears to have minimal systematic errors which appear as the small ripples before the first PDF peak at $r = 2.4$ Å. These result

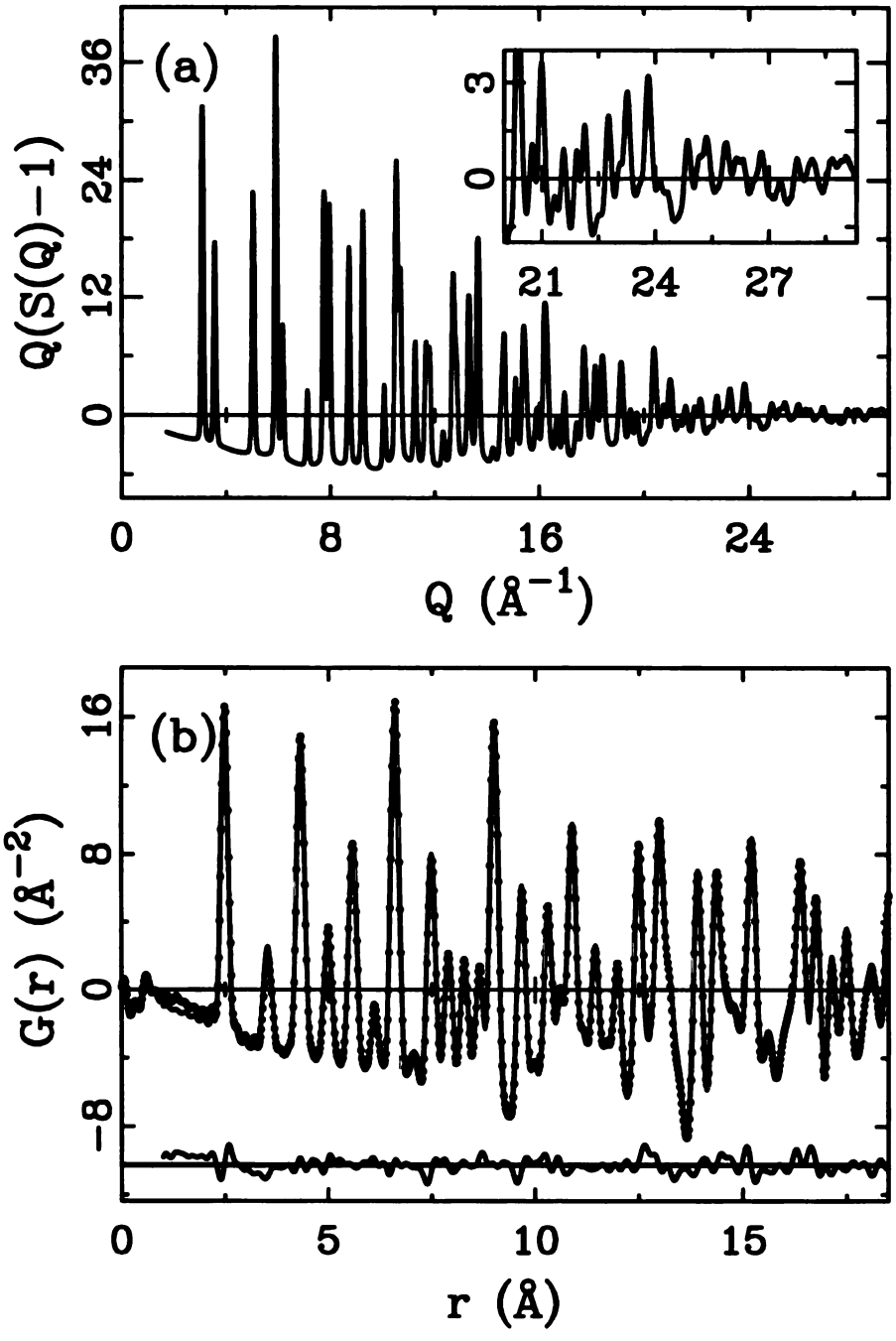

Figure 2.4: (a) The experimental reduced structure function $F(Q) = Q * (S(Q) - 1)$ of Ni powder. The inset is a zoom in of high Q region showing the excellent signal to noise. (b) The experimental $G(r)$ (solid dots) and the calculated PDF from refined structural model (solid line). The difference curve is shown offset below.

from imperfect data corrections and their small amplitude is a good indication of the high quality of the data. A structural model (space group $Fm\bar{3}m$) was readily refined, and gave excellent agreement with the data as shown in Fig. 2.4(b). The lattice parameter (3.5346(2) Å) and an isotropic thermal displacement parameter (U = 0.005184(6) Å^2) were refined. The lattice parameters reproduce the expected values given in previously published data [18]. In spite of the simplicity of the Ni crystal structure, the exceptional quality of both the experimental Ni PDF and refinement indicates that the necessary data corrections of image plate data with high Q range (28.5 Å^{-1} in this case) can be carried out properly and with an acceptable level of accuracy.

The weakly scattering α-AlF_3 compound, in addition to a slightly more complex structure than Ni, presents a greater challenge to proper data correction due to the majority contribution of Compton scattering in the high Q region. The reduced structure function and resulting PDF are shown in Fig. 2.5. The data were successfully refined using a previously reported model from the literature (space group $R\bar{3}c$) [69]. The fit is shown in Fig. 2.5(b). The overall quality of the fit is good with a weighted profile agreement factor [11] of 3 percent. The refined lattice parameters are a = b = 4.9420(3) Å, c = 12.4365(2) Å. The fractional coordinate of the F atom is x = 0.4267(4). These numbers are consistent with the Rietveld refinement of the same data, which produced refined lattice parameters of a = b = 4.9383(4) Å and c = 12.4271(1) Å, and a fractional coordinate, x = 0.4287(4), for the F atom. Both refinements are consistent with the published data of 4.9381(5) Å, 12.4240(3) Å, and 0.4309(4), respectively [65]. The successful application of PDF analysis of α-AlF_3 data indicates this technique is capable of handling weakly scattering materials and still gives reliable information.

In addition to the highly crystalline and rather simple nickel and α-AlF_3 structures, the more complex and disordered layered Aurivillius type oxide anion conduc-

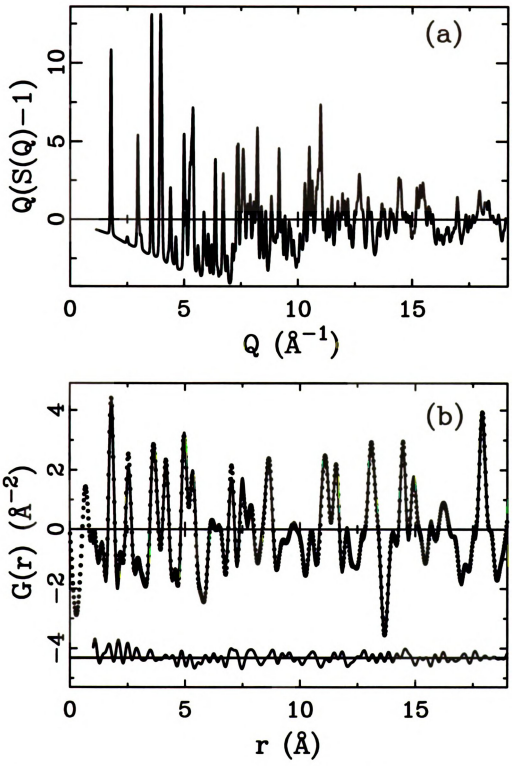

Figure 2.5: (a) Experimental reduced structure function $F(Q) = Q * (S(Q) - 1)$ of α-AlF_3, (b) $G(r)$ and modeled PDF of α-AlF_3, notations as in Fig. 2.4.

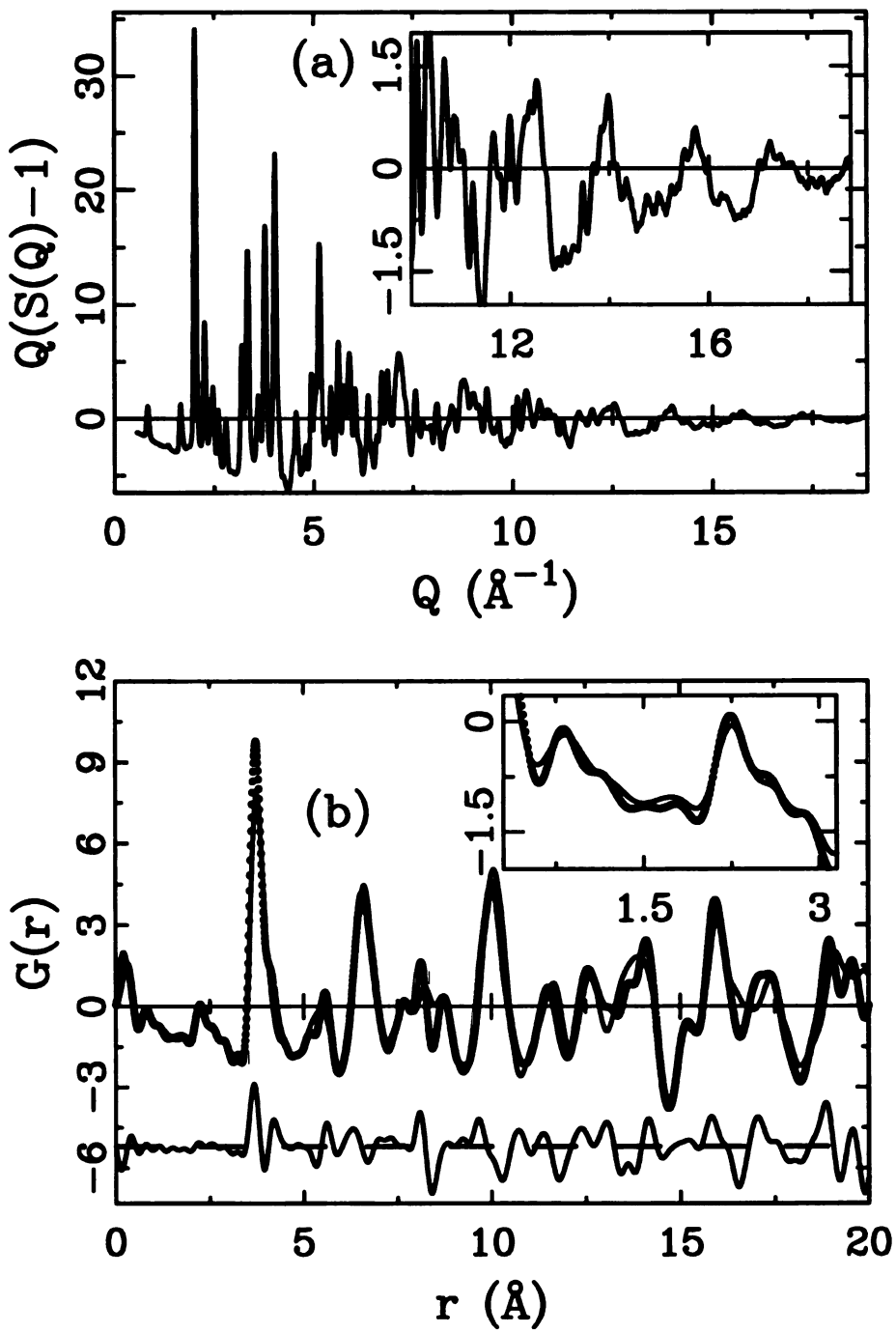

Figure 2.6: (a) Reduced structure function F(Q) of $Bi_4V_2O_{11}$, (b) Experimentally obtained $G(r)$'s of $Bi_4V_2O_{11}$ (solid dots) and $Bi_4V_{1.7}Ti_{0.3}O_{10.85}$ (solid line). The differences between them are plotted below with an offset, noting the high reproducibility in the low r region (also shown in the inset).

tors $Bi_4V_2O_{11}$ and $Bi_4V_{1.7}Ti_{0.3}O_{10.85}$ were examined. The structure is derived from the ordered $Bi_4Mo_2O_{12}$ structure, which contains alternating $Bi_2O_2^{2+}$ layers spaced by corner sharing perovskite MoO_6 layers [66, 70]. The vanadium analogues contain significant disorder in the vanadium layers due to oxygen vacancies. Vanadium can exist in 4, 5, and 6 coordinate environments, inducing significant static disorder in these layers, which is further complicated by dynamic disorder resulting from the high anionic conductivity of these materials. Titanium substitution on the vanadium sites leads to the stabilization of the high temperature γ-phase. The experimentally obtained reduced structure function, F(Q), of $Bi_4V_2O_{11}$ is shown in Fig. 2.6(a). A combined PDF and Rietveld analysis was carried out on the same data set and detailed results will be reported elsewhere. To examine the reproducibility of the systematic errors in the IP data analysis, the measured data for the compounds $Bi_4V_2O_{11}$ and $Bi_4V_{1.7}Ti_{0.3}O_{10.85}$ were compared (Fig. 2.6(b)). Clearly, the ripples in the low r regions are rather small and highly reproducible, implying the high reliability of the PDF data especially for comparative studies. For example, very small differences exist around the first V-O bond length of 1.80 Å, as evident in the inset of Fig. 2.6(b). The significant differences beyond the first peak reveal the somewhat drastic structural changes on longer length scales. This also shows that RA-PDF is capable of capturing structural changes where they exist, reproducing local structures if unchanged.

Medium-high real-space resolution PDF data analysis from crystalline materials was performed by using image plate data and shows promising results. Comparable or even better statistics than from conventional X-ray measurements can be achieved with significantly shorter counting times. The new combination of a real space probe and fast counting time opens up a broad field for future applications to a wide variety of materials of both scientific and technological interest. For example, PDF methods could be used to study structural changes under *in situ* conditions [71] and the time development of chemical reactions and biological systems over short time scales of

seconds may be studied.

2.6 Comparison of the RA-PDF with conventional X-ray PDF method

The use of an image plate area detector for quantitative PDF analysis needs to be properly validated due to the experimental uncertainties described in early sections. For example, the lack of energy resolution intrinsic to the IP, and the energy dependence of the IP response. Therefore, we quantitatively compare the X-ray Data collected with the IP with that from energy resolved solid state detector (SSD).

2.6.1 Description of the experiments

A powdered sample α-AlF_3 was measured with the IP and SSD detectors under *the same* experimental conditions at the 1-ID beam line at the Advanced Photon Source (APS) located at Argonne National Laboratory, Argonne, IL (USA). The X-ray energy used is 99.8 keV, with beam size of 0.4 by 0.4 mm. The sample was loaded into a quartz capillary with diameter of 1 mm. The beam stop is a solid tantalum cylinder (diameter 3.1 mm), with an indentation machined to a depth of approximately 2 mm to accept the beam. Data collection with the IP detector was performed first. A Mar345 image plate camera was mounted orthogonal to the beam path, with the beam centered on the IP. Experimental calibration measurement such as the sample to detector distance is the same as described elsewhere [61]. A single exposure of 20 seconds was collected. Then, an SSD was used by moving the IP out and keeping all other setups. The Ge SSD detector (Canberra GL 0110S) was mounted on the 2θ arm for an angle dispersive scan over the same 2θ range as in the IP measurement ($\approx$ 35 degrees). The energy window of the single channel analyzer was set to include only elastic and Compton intensities. Two 2θ scans were made

with the same step size of 0.02°. The first is from 0.8 to 15.0 for 4 seconds at each point; the second is from 15.0 to 35.0 for 6 seconds. The total measurement time was around 10 hours. Scattering from the an empty capillary was also collected with both detectors for background subtraction. The program PDFgetX2 [41] was used to process the X-ray powder diffraction data with details described earlier. Structure model refinements with experimental PDFs were carried out with PDFFIT [11], a profile fitting least-squares regression program. The powder diffraction data are also analyzed by reciprocal space Rietveld refinements with program GSAS [68].

2.6.2 Results

Fig. 2.7(a-1) and (a-2) show the respective reduced structure factor function $F(Q)$ with Q_{max} of 21.0 Å^{-1}. The smaller scale of the IP data in (a-1) comes from its lower Q space resolution than the SSD data. A more significant difference is the counting statistics in the high Q region. The IP data with 20 seconds collection time appear to show much better signal to noise ratio than the SSD data (10 hours) in the high Q region. The corresponding $G(r)$s are shown in Fig. 2.7(b-1) and (b-2) as filled circles. The Al-F bond length around 1.80 Å gives the first physical PDF peak. The high frequency spurious ripples below 1.80 Å serve as a good indicator of the level of experimental uncertainties coming from systematic errors. Both PDFs show comparably high qualities with those ripples being rather small. It is noteworthy that the somewhat expected high ripple levels in SSD data from the significantly worse counting statistics is absent in the $G(r)$. As a direct comparison of the two experimental PDFs subject to different experimental Q space resolutions, the crystal structure (space group $R\bar{3}c$ [69]) of α-AlF_3 is then fitted to both PDFs to see whether the same structural information can be obtained. The calculated PDFs from refined crystal structures are shown in Fig. 2.7(b-1) and (b-2) as solid lines accordingly with the difference curves plotted below. Both fits show excellent agreement with the

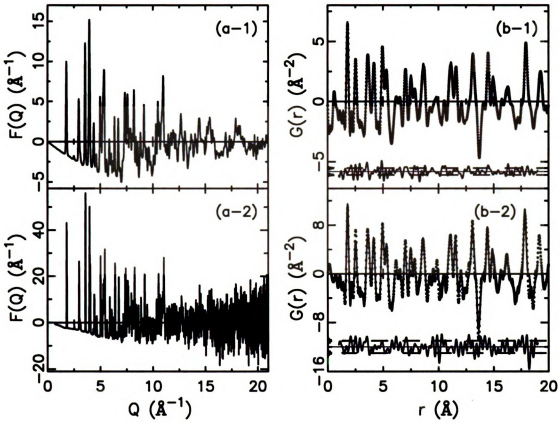

Figure 2.7: (a-1) and (a-2) show the experimental reduced structure function $F(Q) = Q(S(Q) - 1)$ of α-AlF_3 from IP and SSD, respectively. (b-1) and (b-2) show the **corre**sponding $G(r)$ obtained via a sine Fourier transform of (a-1) and (a-2) in filled **circle**s. The solid curve on top of each experimental $G(r)$ is the calculated PDF **from** the refined crystal structure, with the difference curve show below offset. The **horiz**ontal dashed lines indicate the $G(r)$ uncertainties at 1 σ level.

weighted residual factor R_{wp} of 15% and 26% for IP and SSD data, respectively. The **origin** of both difference curves (random noise like) appears to be determined by the **experi**mental statistical noise, and the fact of higher statistical noise level in SSD data **becom**es rather apparent. To see how the refined crystal structures differ from each **other**, we calculated PDFs from them with the same experimental factors, and show **the two** calculated PDFs in Fig. 2.8. Their minimal differences evidenced from their **differe**nce curve shown below indicates the two refined models contain quantitatively **the same** structure information. Rietveld refinement of both the IP and SSD data **were** also carried out. Table 2.1 shows the obtained lattice parameters from PDF and

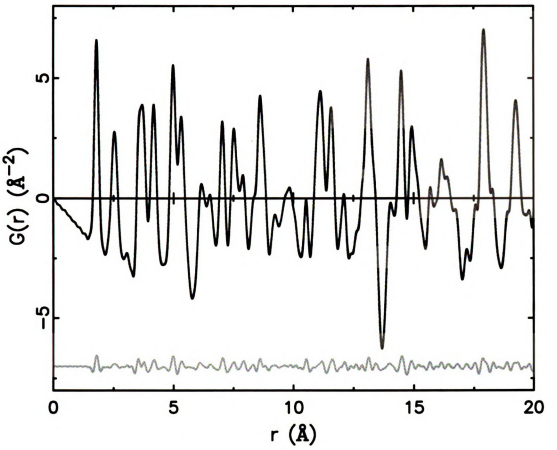

Figure 2.8: Calculated PDFs from the refined crystal structures with the IP and SSD $G(r)$s. Their difference is shown offset below.

Rietveld refinements of both IP and SSD data. The IP and SSD data refinements result in somewhat large deviations on the lattice constants. One possible reason could be the large uncertainties during our experimental calibrations. In addition, the different instrumental resolution functions of the IP and SSD also contribute to the deviations in lattice constants, which is discussed in detail in [10]. We would like to point out that other lattice parameters from PDF refinements of both data sets are in very good agreement, while the Rietveld refinements give rather different thermal factors.

	IP (PDF)	IP (Rietveld)	SSD (PDF)	SSD (Rietveld)
$a = b$ (Å)	4.9468(3)	4.9381(3)	4.9221(5)	4.9216(2)
c (Å)	12.4610(17)	12.4443(14)	12.3911(28)	12.4000(10)
F x	0.4257(3)	0.4281(2)	0.4267(5)	0.4277(3)
Al U_{iso} (Å^2)	0.0034(1)	0.0010(1)	0.0027(1)	0.0060(6)
F U_{iso} (Å^2)	0.0100(1)	0.0010(1)	0.0097(1)	0.0059(6)
R_{wp}	0.15	0.04	0.26	0.10

Table 2.1: Lattice parameters of α-AlF_3 from PDF and Rietveld refinements of both IP and SSD data. The estimated standard deviations are shown in the parenthesis immediately following the values.

2.7 New data analysis program: PDFgetX2

PDFgetX2 is a GUI driven program to obtain the pair distribution function from X-ray powder diffraction data. All codes used now are written by me under the guidance of Prof. Simon Billinge. All source codes amount to more than 40,000 lines.

2.7.1 The crystallographic problem

The pair distribution function (PDF) reveals directly in real space the inter-atomic distances in a material. Recent applications have proved the PDF technique as a powerful local structural probe of nanostructured materials [5, 16], as well as its traditional use to study liquids and glasses [31, 32]. The experimental PDF is obtained by a sine Fourier transformation of the total-scattering structure function $S(Q)$, where Q is the magnitude of the scattering vector. To obtain the $S(Q)$ from raw scattering intensities many corrections have to be made to account for various instrument and sample effects. Adding to this complexity, most existing X-ray data PDF analysis softwares are menu driven and less user-friendly. Reproducing an earlier data analysis has been difficult because data processing parameters are usually kept in the notebook other than with the data. Cross-platform compatibility has also been an issue.

2.7.2 Method of solution

In program PDFgetX2, a user-friendly graphical user interface (GUI) has been built to facilitate user interactions with data. Standard corrections [5] due to background subtraction, sample absorption, polarization, and Compton intensities are available. Particularly, for the recent RA-PDF development [61], oblique incident angle correction and and empirical energy dependence of the detection efficiency are also implemented. Standard uncertainties due to finite counting statistics are estimated and propagated in all steps. The final $S(Q)$ and $G(r)$ data files are multiple-column ASCII files with the processing parameters in the header. The $S(Q)$ data also contain the Faber-Ziman coefficients for all partial structure factors as additional columns. The $G(r)$ file format is compatible with the PDF modeling programs PDFFIT and DISCUS [11, 72]. The interactive data language (IDL[1]) is chosen as the software environment, ensuring cross-platform compatibility. In comparison with our menu driven program PDFgetX [44] (no longer supported by us), the PDFgetX2 offers numerous new features and expanded capabilities.

2.7.3 Software and hardware environment

The commercial IDL licensed distribution (version 6.0 or higher), or the freely downloadable IDL Virtual Machine (IDL^{VM}), is the only prerequisite to run PDFgetX2. The IDL^{VM} is freely available from the download section of the IDL website at http://www.rsinc.com/download/. Platforms supported by IDL include Linux/UNIX, WINDOWS, and MACINTOSH. No specific hardware is used by PDFgetX2. Installation of IDL may use up to 200 MB hard disk space, while the current PDFgetX2 distribution takes about 17 MB disk space.

[1] IDL is a registered trademark of Research Systems, Inc. for their Interactive Data Language software

2.7.4 Program specification

Program PDFgetX2 should run in the same way on all supported platforms as the same source is used. The look and feel of the GUI may vary slightly. The program offers flexible choices of data corrections. Essentially all processing parameters are accessible from the GUI. Most intermediate data during correction steps can be directly visualized for quick problem diagnosis. The $S(Q)$ and $G(r)$ data are automatically saved by default.

2.7.5 Documentation and availability

A short tutorial with example data sets can be found in the PDFgetX2 manual that is distributed with the main program, which also includes a reference guide. Program executable and related help files are downloadable from PDFgetX2 web page at http://www.pa.msu.edu/cmp/billinge-group/programs/PDFgetX2/.

2.8 Conclusions

The RA-PDF method features high energy X-rays coupled with an area detector. Use of high energy X-rays provides enough Q space range for quantitative PDF analysis. Use of an area detector offers three to four orders of magnitude reduction of data collection time. The new data analysis program PDFgetX2 implements necessary corrections to account for the characteristics of the IP detector used. We have shown with convincing examples that high quality medium-high resolution PDFs can be obtained from wide range of materials. The RA-PDF method and easy to use program PDFgetX2 expect to significantly lower the barrier for wide-spread PDF applications to a broad scope of crystalline and nano-crystalline materials. For example, more samples can be measured, more detailed phase diagrams can be mapped out with quicker data collection.

The PDF technique can now be introduced to new types of experiments. Time resolution of the RA-PDF method is around 2 minutes, which is limited by the read-out and erasing time. Attempts with the use of solid state area detectors (18 frames per second) have also been made in our collaborations. A large fraction of time resolved experiments can benefit from high real space resolution PDF local structure analysis simply by moving the detector closer to the sample and using high X-ray energies. The overall experimental setup is also significantly simplified with no moving parts during data collection. Systems at transient states can be probed with RA-PDF method as well. This puts much less stringent requirements on sample conditions. Materials under extreme conditions such as high pressure, high temperature become possible for PDF studies. Chapter 5 describes some recent RA-PDF applications.

Chapter 3

Orbital Correlations in the Pseudo-cubic *O* and Rhombohedral *R* Phase of Undoped $LaMnO_3$

3.1 Introduction to manganites

Manganites here refer to a family of manganese oxides known to show the colossal magneto-resistive (CMR) effect, where the electric resistivity changes drastically under relatively weak magnetic fields. Partially driven by their potential technological applications in magnetic field sensors and magnetic read-write heads, the CMR manganites have received extensive studies both theoretically and experimentally over the past decades. Maybe, even greater interest in manganites is propelled by their challenge to our current knowledge of condensed matter physics. Of the family of manganites, the very rich phase diagram and fascinating properties provide excellent playground for scientific exploration. The manganite compounds represent one of the best examples of strongly correlated electron systems, a dominant theme of current times.

3.1.1 Earlier studies

The name "manganites" was first given by Jonker and Van Santen in 1950 [73], whose work is the first on the family of manganites. The starting material was $LaMnO_3$ which crystallizes in the cubic structure of the mineral perovskite[1] $CaTiO_3$. The perovskite structure for a generic compound ABO_3 is shown in Fig. 3.1. The important structural motif is the corner shared BO_6 octahedron, i.e., MnO_6 in the manganites. In their pioneering experiments [73, 74], the trivalent La atoms were substituted by divalent Ca, Sr, or Ba atoms to obtain polycrystalline samples of $(La,Ca)MnO_3$, $(La,Sr)MnO_3$, or $(La,Ba)MnO_3$. One of the most intriguing observations was the striking correlation between the ferromagnetism (FM) and electrical conductivity: concomitants of paramagnetism to FM and insulator to metal (IM) transition driven by either doping or temperature.

The origin of the ferromagnetic phase was first attributed to a positive indirect-exchange interaction. This view was soon replaced by the so called "double exchange" mechanism proposed by Zener in 1951, which still remains at the core of our understanding of these magnetic oxides. In a series of seminal papers [75, 76, 77], Zener "interpreted the ferro-magnetism as arising from the indirect coupling between incomplete d-shells via the conducting electrons". A quantitative relationship between electrical conductivity σ and the Curie temperature (T_c) was also developed: $\sigma \cong (xe^2/ah)(T_c/T)$, where x is the fraction of Mn^{4+} among all Mn ions and a is the lattice constant. Excellent agreement with the data of Jonker and Van Santan was found within a factor of 2. Another corner stone of double exchange theory came from Anderson and Hasegawa [78]. Their perturbative approach deduced that the effective hopping amplitude between neighboring Mn ions is proportional to $\cos(\theta/2)$, where θ is the classical angle between the core spins of neighboring Mn ions.

In 1955, the structure of magnetic ordering over the entire composition range of

[1] Perovskite is named for a Russian mineralogist, Count Lev Aleksevich von Perovski

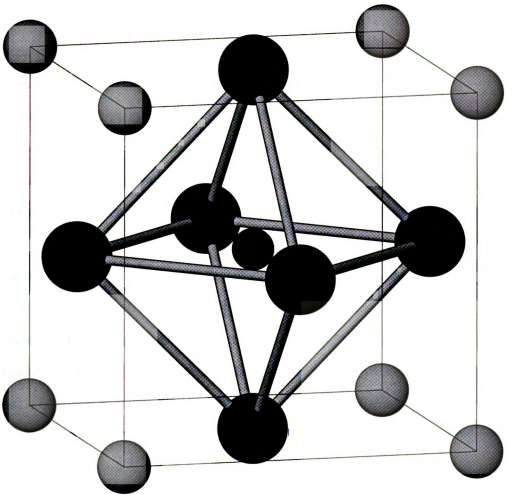

Figure 3.1: Crystallographic representation of the perovskite structure with chemical formula ABO_3. A is the cation on the corner, B is the cation in center of the O_6 octahedron, O atoms lie on the face centers.

$La_{1-x}Ca_xMnO_3$ was discovered in a remarkable early neutron diffraction studies by Wollan and Koehler [79] from Oak Ridge National Laboratory. The early magnetic phase diagram obtained by the neutron scattering technique closely matches the modern version coming 50 years later [80]. As a function of Ca doping, many interesting ferromagnetic and anti ferromagnetic phases were found. It is worth noting that evidence of charge ordering was also reported in the anti ferromagnetic phases. Lattice distortion was also studied with X-ray diffraction measurements in these early experiments.

Following the paper by Wollan and Koehler, Goodenough presented a theory of semi-covalent exchange [81], and successfully explained the observed rich magnetic and structural phase diagram. Kanamori revisited this problem, and compiled the still widely used Goodenough-Kanamori rules [82, 83]. More details will be discussed later.

In the following years, not much attention was given to manganites. Only to mention a few, Morrish *et al.* in 1969 [84] found a way to grow high quality millimeter long single crystal manganites with composition (La,Pb)MnO_3. The results of previous studies on polycrystalline materials were confirmed. Searle and Wang [85, 86] proposed a phenomenological model based on a strongly spin-polarized conduction band to explain the ferromagnetism. Nonetheless, the family of manganites enjoyed a greatly renewed interest since the discovery of the colossal magneto-resistive (CMR) effects.

3.2 The colossal magneto-resistive effect

The earliest account of magneto-resistance (MR) data was reported by Volger in as early as 1954 [87]. The observed decrease of resistivity in magnetic fields in the ferromagnetic phase was puzzling, but the true size of this effect was not appreciated. About 45 years later, notably large MR effects were found in $Nd_{0.5}Pb_{0.5}MnO_3$ bulk

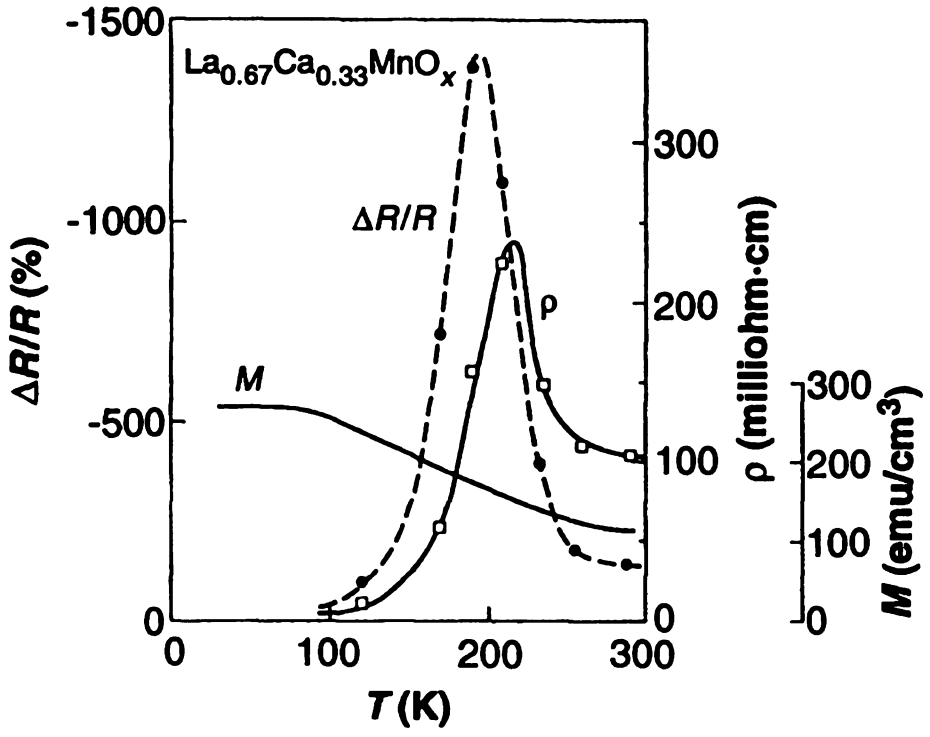

Figure 3.2: The MR ratio $\Delta R/R$ (dashed line) as a function of temperature for thin films $La_{1-x}Ca_xMnO_3$ at x=0.33 after 750°C treatment for 0.5 hour. The electric resistivity ρ and magnetic susceptibility M are also shown. Taken from Ref. [92].

samples [88] (Kusters *et al.* , 1989) and $La_{2/3}Ba_{1/3}MnO_3$ thin films [89] (von Helmolt *et al.* , 1993). Similar observations were also published by Chahara *et al.* [90] and Ju *et al.* [91]. However, the name "colossal" was not coined till the truly colossal MR ratios reported by Jin *et al.* [92] in 1994 on films of $La_{2/3}Ca_{1/3}MnO_3$. In Jin *et al.* 's paper, the MR ratio is defined as $\Delta R/R = (R_H - R_0)/R_H$, where R_0 is the resistance with zero magnetic field strength, and R_H is the resistance in a magnetic field of 6 T. Fig. 3.2 shows the temperature dependence of the MR ratio $\Delta R/R$ directly taken from the original paper. The largest MR ratio in Fig. 3.2 occurs at 200 K, reaching close to 1500%, which is much larger than any previously reported value in any system. They also succeeded in accomplishing the largest MR ratio over 100 000% after some optimization treatment of the films. A rather exhaustive literature search found that the record value of MR ratio is approximately 100 000 000% observed on

$La_{0.5}Ca_{0.5}MnO_3$ films at 57 K by Gong *et al.* [93].

The enormous magnitude of the MR found in manganites should be distinguished from the previously discovered giant magneto-resistance (GMR). GMR materials are multi-layer metallic films showing a relatively large sensitivity to magnetic fields. The mechanism in these films is largely due to what is known as the spin-valve effect between spin polarized metals. If an electron in a regular metal is forced to move across a spin-polarized metallic layer (or between spin-polarized layers) it will suffer spin-dependent scattering. If the electron was initially polarized parallel to that of the layer the scattering rate is relatively low; if initially polarized anti-parallel to that of the layer the scattering is high. The effect of an external field is to increase the ratio of the former events to the latter by aligning the polarization of the magnetic-layer along the direction of the external field. This effect has the very important advantage of not being limited to low temperatures. Another important difference from CMR is that usually only several tenths of a Tesla magnetic field is necessary, while the CMR materials may require a field of over 5 T.

The CMR effect in manganites can be thought of as a magnetic field driven insulator to metal (IM) transition. This has great similarity to the temperature driven IM transition concomitant with the PM to FM magnetic phase transition. Qualitatively, the observed CMR effect can be explained within the context of theory of double exchange. The external magnetic field will drive the material from PM to FM phase when sufficiently large. This would induce the insulator to metal transition. However, the enormous size of the CMR effect cannot be explained quantitatively by double exchange only [94]. Significant theoretical developments over the past decade have greatly improved our understanding of the physics of manganites.

3.3 Physics of manganites

In the chemical formula $AMnO_3$, oxygen has valence of -2. Thus manganese is trivalent when the ion on A site is +3 valenced, e.g. La^{3+}. Substitution of ions on A sites by divalent ions (Ca^{2+}, Sr^{2+}, etc) results in mixed valenced manganese ions: Mn^{3+} and Mn^{4+}. The trivalent and tetravalent Mn ions have very different properties in the lattice. The electronic configuration of a Mn^{3+} ion is $1s^2 2s^2 2p^6 3s^2 3p^6 3d^4$. Therefore, the $3d$ shell, being the only partially filled shell, is of interest. When placing the 4 electrons in the five $3d$ (l=2, m_l=$-2, -1, 0, 1, 2$) orbitals, a few relevant interactions, within current context, need to be considered. The first is the on-site Coulomb repulsion energy U between electrons on the same site and same orbital (same m_l). U was estimated to be 5.2±0.3 eV and 3.5±0.3 eV for $CaMnO_3$ and $LaMnO_3$ respectively, by Park *et al.* [95], using photo-emission techniques. The second is the Hund (ferromagnetic) coupling between electrons on different orbitals. The exchange constant J_H was suggested to be larger than 1 eV from both experimental and theoretical studies [96, 97, 98]. Thus, as a result of the strong on-site coulomb repulsion, the four $3d$ electrons will have their spins lined up in parallel, and occupy 4 of the 5 orbitals, resulting in a total spin of S=2. In the case of Mn^{4+}, we can simply remove one of the four electrons, resulting a total spin of S=3/2.

3.3.1 Crystal field effect

Mn ions sit in the center of the octahedral cage formed by six O^{2-} ions. Let us first assume that the octahedral cage has normal shape, meaning six equi-distant Mn-O bond lengths. As a consequence, the spherical symmetry of the Mn ions is broken; the degeneracy of the five $l = 2$ $3d$ orbitals is also broken. This is known as the crystal field effect, though most times only the influence of neighboring O^{2-} ions is considered. Considering the cubic symmetry of the surrounding O^{2-} ions, the split

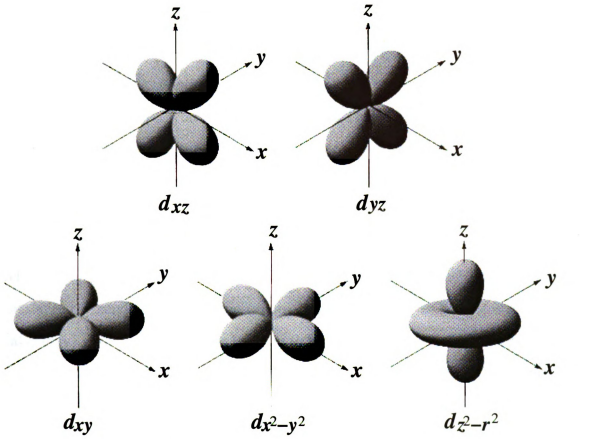

Figure 3.3: Contour visualization of the five 3*d* atomic electron orbitals. Shown are the electron equi-density surfaces.

of the five d-shell orbitals results in two groups, the π bonding orbitals d_{xy}, d_{yz}, d_{zx} with symmetry class t_{2g}, and the σ bonding orbitals $d_{3z^2-r^2}$, $d_{x^2-y^2}$ with symmetry class e_g. The five 3*d* orbitals are visualized in Fig. 3.3. e_g orbitals have higher energy than t_{2g} orbitals. This can be understood qualitatively as electrons in e_g orbitals feel more repulsion from the O^{2-} ions than in t_{2g} orbitals (e_g orbitals project toward neighboring O^{2-} ions, while t_{2g} orbitals points into the empty space in between O^{2-} ions). The actual energy split can be calculated to be $\Delta = \frac{5Zq}{3a^5}\langle r^4 \rangle$, where Zq is the charge of the oxygen ion, a is the Mn-O distance, r is the distance of the electron to the centering Mn ion [99]. In practice, the gap Δ typically varies between 1 and 2 eV.

3.3.2 Jahn-Teller distortion

Let us now review how the four 3d electrons of an Mn^{3+} ion would occupy those five orbitals. Since the largest energy scale is still the on-site coulombic repulsion, no double occupancy of a single orbital would be allowed. Therefore, the triplet t_{2g} orbitals have one electron in each orbital. The fourth electron becomes the *single* e_g electron. We need to recall that the results of e_g doublet and t_{2g} triplet are obtained assuming a cubic symmetry, i.e. in a normal shape MnO_6 octahedron. Though all t_{2g} orbitals are singularly occupied, the two e_g orbitals have only *one* electron. Further energy level splitting due to lattice distortion will be favored by the one electron occupied e_g orbitals, as the single e_g electron can occupy the lower energy orbital (thus lower the total energy). This energy splitting is found to be linear to the lattice distortion, while the energy compensation of lattice distortion grows quadratically with the distortion (when the distortion is small). Thus, a symmetry lowering lattice distortion becomes spontaneously energetically favorable. This is known as the Jahn-Teller (JT) effect resulting in the lifting of degeneracy due to the orbital-lattice interaction.

Even when only one MnO_6 octahedron is considered, the possible JT distortions become non-trivial, as there are 21 degrees of freedom (seven atoms: one Mn and six O). The following simplifications will be made. First, translational degrees of freedom of the octahedron as a whole can be thrown away (-3). Second, the rotation of the octahedron is ignored since it does not contribute to the energy splitting within one octahedron, and the orthogonality of the octahedron is maintained (-12). Then only 6 degrees of freedom are left. At last the Mn ion is always constrained to be in the center of the octahedron (-3). Now we have 3 degrees of freedom. Borrowing the notation used by Kanamori [82], the normal modes of our interest are Q1, Q2, Q3. They are depicted in Fig. 3.4 for one MnO_6 octahedron. Under the influence of mode Q1, the octahedral shape is kept normal, it only expands or shrinks as a whole, mimicking the movement of breathing. Q1 mode is thus sometimes called the

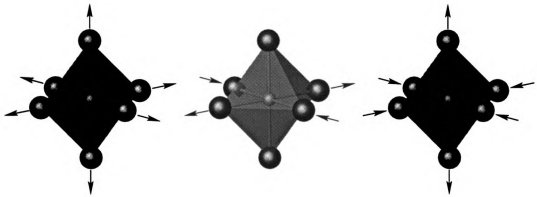

Figure 3.4: Schematic plot of the Q1, Q2, and Q3 (from left to right) Jahn-Teller distortion modes of one MnO_6 octahedron. Arrows point to the moving direction of oxygen atoms relative to a normal octahedron.

breathing mode. Mode Q2 will distort the octahedron, resulting in two long, two short, and two medium Mn-O bonds. The Q3 mode also distorts the octahedron, resulting in two long, four short (or four long, two short) Mn-O bonds. The observed JT distortion would presumably be a linear combination of the normal modes Q1, Q2, Q3. In practice, Q3 is the dominant mode, usually together with some degree of the Q2 mode.

The magnitude of the JT distortion is determined by the balance of the degeneracy lifting of e_g orbitals and the lattice strain energy compensation. The corresponding eigenenergy E_{JT} of this electron-lattice coupling is estimated to be around 0.25 eV by Dessau and Shen [100]. Relevant to this study, this static Jahn-Teller energy E_{JT} corresponds to a temperature of 2,901 K, much higher than normally probed temperature range. As MnO_6 octahedra share their corner O^{2-} atoms, the JT distortions between the neighboring octahedra are directly correlated, giving rise to a strong anti-ferrodistorsive coupling. We would like to point out that the ignored rotation of MnO_6 octahedron leads to the *buckling* mode, which may play a significant role in releasing the lattice strain. However, most theoretical calculations have simply ignored this lattice stiffness effect.

One very important result that should be kept in mind is that the $Mn^{4+}O_6$ octahe-

dron does *not* subject to the JT distortion. The reason is the absence of e_g electrons, and its t_{2g} orbitals all have single occupancy. Thus, its total energy is not sensitive to the lifting of degeneracy of e_g or t_{2g} orbitals induced by JT distortions.

3.3.3 Double exchange mechanism

The version of the theory of double exchange introduced by Zener [75, 76, 77] offered a qualitative and descriptive understanding of the origin of ferro-magnetism. It states that the conducting electrons will remember their spin orientations when wandering around. In transition metal oxides, those electrons come from the incomplete d−shells. Suppose we have one Mn^{3+} and one Mn^{4+} bridged by an O^{2-} ion, the e_g electron on Mn^{3+} is contributing to the electric conductivity. The spin of this e_g electron will first be parallel to the spins of core electrons on the t_{2g} orbitals. When this electron moves to the Mn^{4+} via the bridging O^{2-}, the total energy of the system would increase due to the Hund coupling if Mn^{4+} has a different spin orientation. Thus, high conductivity is expected when the neighboring Mn ions have their spins aligned in parallel. On the other hand, increasing the mobility of the e_g electron helps to lower its kinetic energy. One way to understand this is the following: the more mobile an electron is, the broader its wave function is, the smoother its wave function becomes. The kinetic energy of the electron is related to the second derivative of the wave function, thus the kinetic energy is reduced with increased mobility. The result of this interaction is that the conducting electrons favor ferromagnetism to lower their kinetic energy. Thus, the anomaly of electrical conductivity in the ferromagnetic phase [73] is successfully explained.

The name "double exchange" originated from the proposed scenario of charge transfer by Zener [75]. The e_g electron hopping from Mn^{3+} to Mn^{4+} was first considered to be a one-step process. Direct hopping is not very likely due to the presence of bridging O^{2-} atoms. Zener then suggested that the process can be completed

by simultaneous charge transfer from the O^{2-} to Mn^{4+}, and from Mn^{3+} to O^{2-}. It is a *double exchange* of electrons with the same spin, though it is hard to imagine how it actually occurs in real systems. A more quantitative study by Anderson and Hasawaga [78] took a perturbative approach with the introduction of the hopping amplitude t reflecting the electron mobility. They proposed that the transfer of electrons from Mn^{3+} to Mn^{4+} occurs one by one, not simultaneously as believed by Zener. One fundamental result is the dependence of effective hopping amplitude on the angle θ between the classic spins of core electrons (t_{2g} electrons) of the neighboring Mn ions: $t_{eff} = t \cdot cos(\theta/2)$. The value of the hopping amplitude t is not well estimated from either experiments or theories. Dessau and Shen [100] have reported a value as large as 1 eV, while a magnitude between 0.2 and 0.5 eV is suggested by Arima *et al.* [101, 102]. Nevertheless, the fairly widely accepted value is a fraction of 1 eV [103, 104].

The $2p$ orbitals of oxygen atoms are the intermediate medium of the electron transfers from Mn to Mn. Thus the hopping amplitude should also depend on the Mn-O-Mn bond angle ϕ, as the efficiency of electron transfer relies on the wave function overlap between the involved orbitals. The overlap is maximized when ϕ is 180 degrees due to the linearity of the 2p orbitals. The significance of angle ϕ leads to the important geometrical factor, *tolerance factor*, defined as $\Gamma = d_{A-O}/(\sqrt{2}d_{Mn-O})$. Here d_{A-O} is the nearest neighbor distance between ions on the perovskite A site and oxygens; d_{Mn-O} is the Mn-O bond length. Generally, localization (insulating) and delocalization (conducting) of the e_g electrons affects the tolerance factor by changing the average Mn-O bond length. More effectively, chemical substitution modifies the lattice due to different ionic sizes. The order of some commonly used ions with increasing size is Mn^{4+} (0.52 Å), Mn^{3+} (0.70 Å), Ca^{2+} (1.06 Å), La^{3+} (1.22 Å), Sr^{2+} (1.27 Å), O^{2-} (1.32 Å), and Ba^{2+} (1.43 Å). A perfect cubic system results in a tolerance factor of 1, and ϕ of 180 degree. When the A site ion is too small and

demands a small d_{A-O}, the dominant effect is the decrease of angle ϕ (octahedral tilt), along with a relatively small decrease of d_{Mn-O}. As discussed before, this would cause the hopping amplitude to decrease, as observed experimentally [92, 80, 105, 106].

3.3.4 Semi-covalent exchange and the Goodenough-Kanamori rule

Semi-covalence originates from the strong overlap between the empty cation (Mn^{3+} or Mn^{4+}) orbitals and the filled orbitals of neighboring anions (O^{2-}). Then electrons will be shared by the empty cation orbitals and the anion orbitals (oxygen $2p$). Those empty cation orbitals are lattice-orbitals that are nearly degenerate with the atomic $3d$ orbitals. It is assumed that the energy difference between the lattice-orbitals and the atomic d shells is smaller than the exchange energy between the shared electron and the cation d shell electrons. Under the above conditions, due to strong exchange forces, the electron whose spin is parallel to the net cation spin will be more preferably shared than the one whose spin is anti-parallel. In this scenario, only one electron contributes to the "covalent" bond, giving the name "semi-covalence". Though the semi-covalence only directly acts on neighboring cations (magnetic) and anions (non-magnetic), magnetic interactions between neighboring magnetic cations can be initiated through the semi-covalent exchange via the bridging anions. In the case of manganites, Fig. 3.5 shows the schematic electron-spin configuration of Mn-Mn magnetic exchange. In manganites, the Mn-O-Mn bond is approximately linear, thus the same oxygen $2p$ orbital (linear) mediates the exchange interaction with the two bridged Mn atoms. The two electrons in one $2p$ orbital have opposite spins. Thus, anti ferromagnetic Mn-Mn coupling will result if each $2p$ electron forms a semi-covalent bond with each Mn atom. This gives the configuration No.1 of Fig. 3.5. If only one of the electron initiates semi-covalence, the O atom will have a net spin anti-parallel to this election. The direct exchange between the O atom and the other

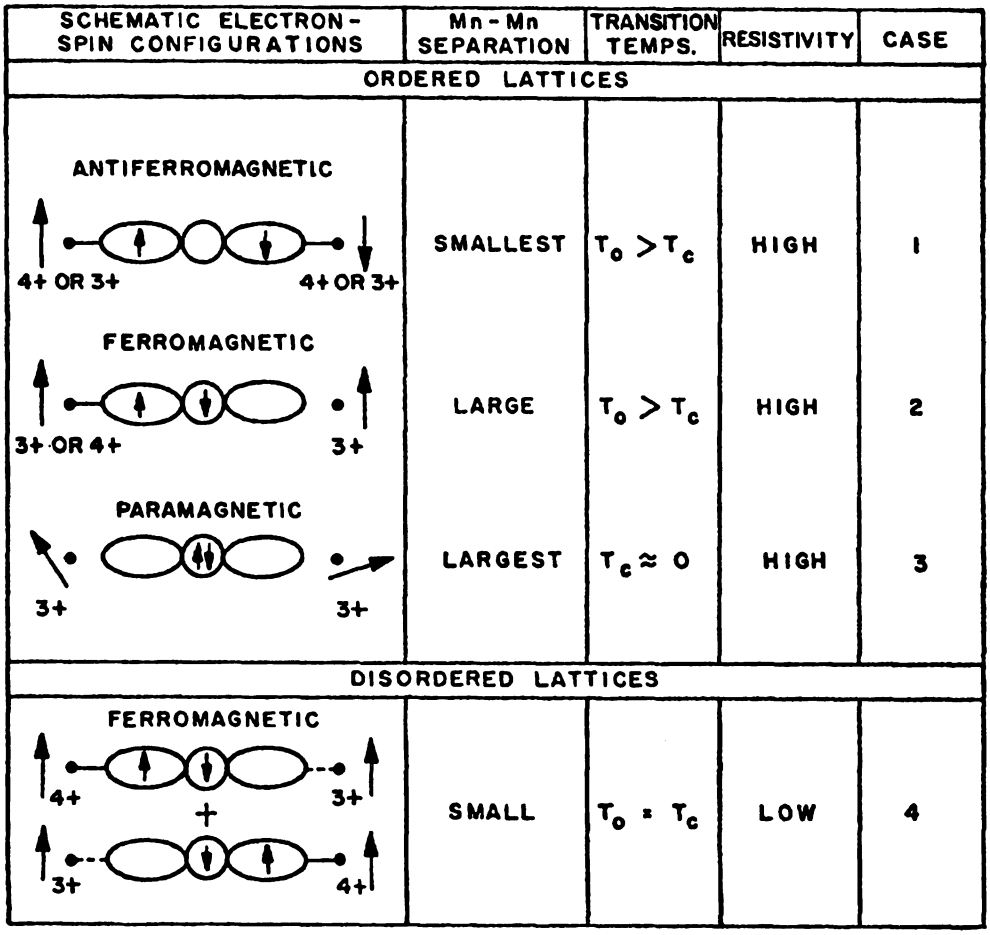

Figure 3.5: The schematic configuration of the Mn-Mn magnetic exchange interaction in consideration of the theory of semi-covalence exchange. Taken from Ref. [81].

Mn atom (ionic bond) causes their spins to be anti parallel. Therefore, the Mn-Mn magnetic coupling becomes parallel (case No.2 in Fig. 3.5). There is no semi-covalence in the paramagnetic state. The most interesting case takes place in the disordered lattice where a metallic-like bond forms if an O^{2-} is between a Mn^{3+} and Mn^{4+} ion (the last two cases in Fig. 3.5).

Though theoretical treatment of manganites is elegant and powerful, the resulting physical pictures can not be obtained without extensive scientific computation. Here we introduce an intuitive phenomenological rule for qualitatively understanding the experimental phase diagram. The Goodenough-Kanamori (GK) rules make a correspondence between the magnetic structure and charge and orbital arrangements of

the Mn ions. It is based on the semi-covalence exchange mechanism first proposed by Goodenough [81, 82] to describe the non ionic bonding nature between Mn and O atoms. In 1961, Kanamori [82] compiled the GK rules after revisiting the relation between electronic, magnetic, and lattice structures. It states that, for neighboring Mn ions bridged by an oxygen atom, if one and only one of the anti bonding e_g orbitals with respect to the oxygen atom is filled, ferromagnetic coupling between Mn ions will result. Anti-ferromagnetic coupling is resulted in all other cases. Together with the consideration of lattice elastic energy, the GK rules have successfully predicted the magnetic and structural phase diagram of the cubic perovskite manganites [79, 81]. Though simple, even now, the GK rules are a useful intuitive guide to manganite properties.

It might be useful to distinguish the semi-covalence exchange from the superexchange commonly occurring also via the non-magnetic anions. In the superexchange model based on the non-ionic character of the lattice as well, it is assumed that the exchange energy is smaller than the energy difference between the lattice-orbitals and the cation *d* orbitals. Thus the interaction is through virtual hopping of the anion electrons. Another assumption is that *only one* electron can be excited from the anion orbital to neighboring cation *d* orbitals at one time, and the hopping probability depends on the electron spin due to its coupling with the cation *d* orbital electron spins following the Hund rules. As a result of both virtual hoping and anti ferromagnetic direct exchange of the uncompensated anion spin with the other cation, the magnetic coupling between the cations is ferromagnetic when the cation *d* orbitals are less than half filled, and anti-ferromagnetic when half, or more than half, filled. Therefore, in the case of manganites, the superexchange model will always lead to ferromagnetism, which apparently can not explain the anti ferromagnetic phase observed in manganites.

3.3.5 Summary

The heart of the physics of manganites lies in the intricate competition between electron, spin, and lattice degrees of freedom, resulting in a very rich and intriguing magnetic, structural, and electronic phase diagram. A realistic physical model of manganites needs to include the on-site coulombic repulsion, strong Hund's coupling, electron hopping, and electron-phonon coupling, and maybe more. However, even with some high level of approximation, the Hamiltonian still usually proves too hard to be solved analytically. One important tool employed rather extensively is the large scale physical model computation, such as Monte Carlo simulations and dynamic mean field calculations [107, 108, 99]. Nevertheless, extensive theoretical and experimental efforts to understand the physics of manganites have greatly improved our understanding of strongly correlated electrons systems.

3.4 Phase diagram of $La_{1-x}Ca_xMnO_3$ as an example

The richness of the manganite phase diagram will be briefly illustrated by the example of $La_{1-x}Ca_xMnO_3$, one of the most extensively studied, due to its robust CMR effect and full range of possible doping levels [80, 109, 110, 99, 111, 112]. The phase diagram of $La_{1-x}Ca_xMnO_3$ is indeed very rich and interesting as shown in Fig. 3.6 as a function of Ca concentration x and temperature. The metallic phase only exists over a narrow range of $0.17 \leq x \leq 0.50$, where the important CMR effect is observed. At low doping levels, the lattice structure in ground state is orthorhombic, and the magnetic structure is type-A anti ferromagnetic [80]. This magnetic structure can be considered as ferromagnetic planes coupled anti ferromagnetically. The proposed canted anti ferromagnetism (CAF) is nowadays considered as coming from phase separation at nano-meter scales [99]. It is very interesting to note the coexistence

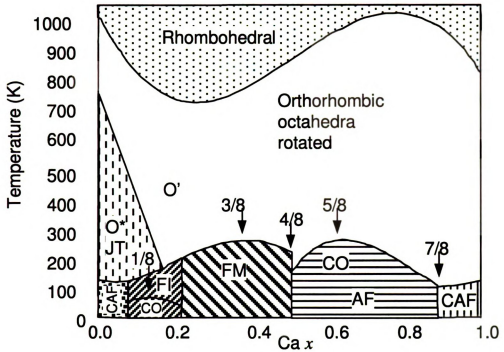

Figure 3.6: Phase diagram of $La_{1-x}Ca_xMnO_3$ as a function of temperature and Ca doping x, after Cheong *et al.* [115].

of the ferromagnetic and insulating phases (FI) between 0.1 and 0.17. At rational doping of $x = 3/8$, the highest curie temperature ($\sim$ 260 K) is observed. The 50% doping presents one particularly interesting case where the type CE charge ordering (CO) [113, 114] is the stable ground state (discussed in more detail in Chapter 4). The highly doped $La_{1-x}Ca_xMnO_3$ ($x > 0.5$) shows various types of anti ferromagnetism. The end member $CaMnO_3$ has a perfect cubic lattice structure and type G anti ferromagnetic (AF) structure where every Mn^{4+} is coupled anti ferromagnetically with its six neighboring Mn^{4+} ions [80]. There is no JT distortion in $CaMnO_3$ because all octahedra are $Mn^{4+}O_6$ octahedra.

Other than changing doping or temperature, external pressure and isotope substitution also considerably modify the phase diagram. Most studies have focused on the effects on the resistivity and Curie temperature [116, 117, 106, 118, 119, 120, 121, 122, 123, 124, 125]. Interestingly, the electric resistivity drastically decreases

and the T_C increases with pressure, which is still not understood [99]. Within current understanding, increasing the pressure will reduce the lattice constants, thus bend more the Mn-O-Mn angle. The hopping amplitude t is reduced by bending the Mn-O-Mn angle. Therefore, we would expect the electric resistivity to increase with pressure. One suggestion by this author, though this remains to be verified, is that the pressure may modify the density of states near the Fermi surface as well. Isotope substitution of ^{16}O with ^{18}O results in change of the T_C of 20 K, which is much larger than observed than in other oxides. These experimental findings clearly indicate the significant involvement of lattice phonons in the important CMR effect.

3.5 Introduction to the question: high temperature phases of the undoped $LaMnO_3$

The perovskite manganites related to $LaMnO_3$ continue to yield puzzling and surprising results despite intensive study since the 1950's [110, 111, 99]. The pervading interest comes from the delicate balance between electronic, spin and lattice degrees of freedom coupled with strong electron correlations. Remarkably, controversy still exists about the nature of the undoped endmember material, $LaMnO_3$, where every manganese ion has a nominal charge of 3+ and no hole doping exists. The ground-state is well understood as an A-type antiferromagnet with long-range ordered, Jahn-Teller (JT) distorted, MnO_6 octahedra [79, 126] that have four shorter and two longer bonds [127]. The elongated occupied e_g orbitals lie pointing down in the xy-plane and alternate between along x and y directions, the so-called O' structural phase [79, 126]. Fig. 3.7 shows the orbital ordering (OO) of the occupied e_g orbitals in the ab plane. Here the MnO_6 octahedra are tilted, giving the crystal structure as shown in Fig. 3.8.

At $T_{JT} \sim 750$ K the sample has a first-order structural phase transition to the

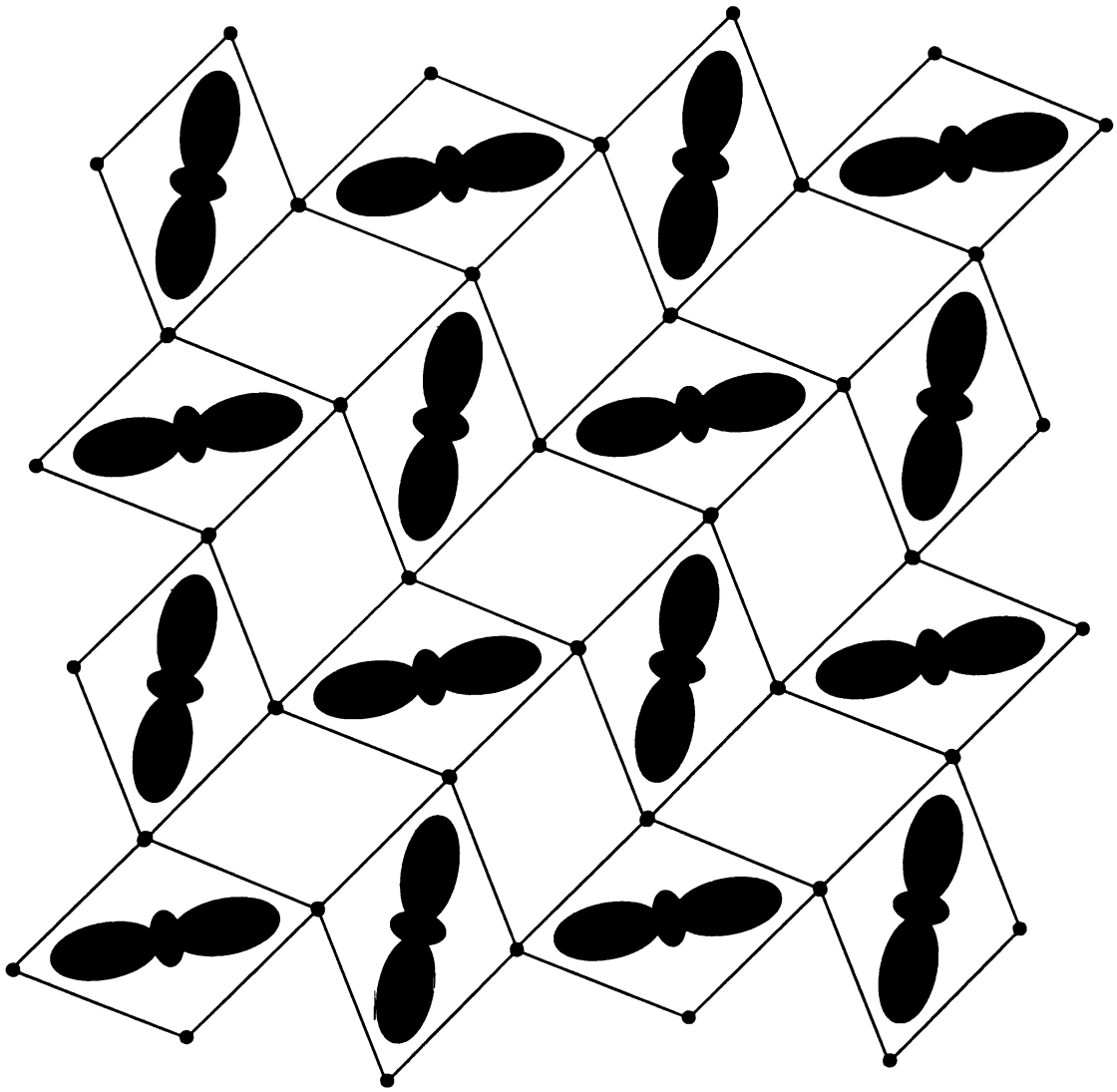

Figure 3.7: Cartoon view of the orbital ordering (OO) in one $LaMnO_3$ plane. Only the occupied e_g orbitals are shown.

O phase that formally retains the same symmetry but is pseudo-cubic with almost regular MnO_6 octahedra (six almost equal bond-lengths). In this phase the cooperative JT distortion has essentially disappeared. It is the nature of this *O* phase that is unclear. The *O*-phase has special importance since it is the phase from which ferromagnetism and colossal magnetoresistance appears at low temperature at Ca, Sr dopings > 0.2 [79].

The additional complication of disorder due to the presence of alkali-earth dopant ions, and the doped-holes on manganese sites, is absent in $LaMnO_3$. However, there

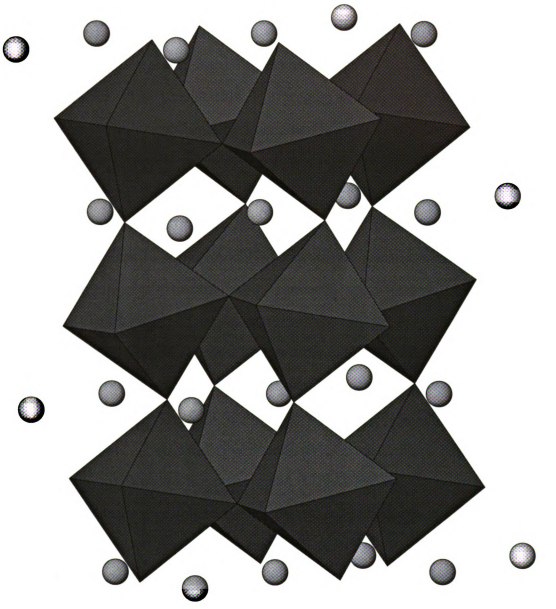

Figure 3.8: Crystal structure of $LaMnO_3$. The MnO_6 octahedron is shown as one unit, noting its tilting.

is still disagreement about the precise nature of the O-phase in this simple case. In 1996 Millis [128], based on fits to data of a classical model that included JT and lattice terms, estimated the energy of the JT splitting to be $\gtrsim$ 0.4 eV and possibly as high as 2.4 eV. This high energy scale clearly implies that the JT distortions are not destroyed by thermal excitation at 750 K and the O'- O transition is an order-disorder transition where local JT octahedra survive but lose their long-range spatial correlations. The barrier that is overcome at this transition is the lattice stiffness that serves to orientationally order the distorted octahedra. This picture is supported by some probes sensitive to local structure, for example XAFS [129, 130] and Raman scattering [131], each of which present evidence that structural distortions consistent with local JT effects survive above T_{JT}. However while compelling, this picture seems hard to reconcile with the electronic and magnetic properties. In the O-phase the material's conductivity increases (despite being at higher temperature and more disordered), and becomes rather temperature independent [132], and the ferromagnetic correlations become stronger compared to the O'-phase [132, 133]. These results clearly imply greater electronic mobility in the O-phase, which appears at odds with the persistence of JT distortions above T_{JT} that are becoming orientationally disordered. The disordering should result in more carrier scattering and higher resistivity, contrary to the observation [132]. Furthermore, a sharp decrease in the unit cell volume at T_{JT} has been reported [134], which mimics the behavior observed when electrons delocalize and become mobile at T_c in the doped materials [135]. The authors of Ref. [134] reconcile this observation with the order-disorder picture of the phase transition by analogy with the volume drop on melting of ice, though the connection seems somewhat tenuous.

3.6 Experimental methods

Two $LaMnO_3$ samples with slightly different oxygen stoichiometry were measured. The first sample, referred to as $LaMnO_3$(A), is nearly perfect stoichiometric with negligible excess oxygen content, while the other sample, refereed as $LaMnO_3$(B), has small but non-negligible amount of excess oxygen content. We will show that the two samples give qualitatively the *same* results.

3.6.1 Sample preparation

Powder $LaMnO_3$(A) sample of $\sim$ 6 g was prepared from high purity MnO_2 and La_2O_3; the latter was pre-fired at 1000 °C to remove moisture and carbon dioxide. Final firing conditions were chosen to optimize the oxygen stoichiometry at 3.00. The crystallographic behavior was confirmed by a Rietveld refinement of the same data used in the PDF, using program GSAS [68]. Both the differential thermal analysis (DTA) and Rietveld measurements estimated the same phase transition temperature of $T_{JT}\sim$ 735 K and $T_R \sim$ 1010 K (discussed in detail later). These values indicate that the sample is highly stoichiometric, e.g. T_{JT}=750 K for perfectly stoichiometric sample and around $T_{JT}\sim$ 600 K reported for 0.005 excess oxygen per chemical formula unit [136, 126].

The $LaMnO_3$(B) sample was prepared using standard solid state reaction methods. Stoichiometric amounts of La_2O_3 (Alfa Aesar Reacton 99.99%) and MnO_2 (Alfa Aesar Puratronic 99.999%) were ground in an Al_2O_3 mortar and pestle under acetone until well mixed. The powder sample was loaded into a 3/4" diameter die and uniaxially pressed at 1000 lbs. The pellet was placed into an Al_2O_3 boat and fired under pure oxygen for 12 hours at 1200-1250 °C. The sample was cooled to 800 °C and removed, reground, repelletized, and refired at 1200-1250 °C for an additional 24 hours. This process was repeated until a single phase, rhombohedral, X-ray diffraction pattern

was obtained. Total reaction time was approximately 5 days. Thermogravimetric analysis (TGA) indicated that the as-prepared sample had an oxygen stoichiometry of about $LaMnO_{3.10}$. The $LaMnO_{3.10}$ sample was ground, left in powder form, and placed into an Al_2O_3 boat. The sample was post-annealed in ultra high purity Ar at 1000 °C for 24 hours then quenched to room temperature. The oxygen stoichiometry was again determined using TGA under forming gas. The final oxygen stoichiometry was 3.006.

3.6.2 Differential thermal analysis

Differential Thermal Analysis (DTA) data collection: The main goal of the DTA measurement was to find the phase transition temperatures T_{JT} and T_R, which would be used to guide the later neutron powder diffraction experiments. Sample $LaMnO_3$(A) of 0.1033 gram was sealed under vacuum in one quartz tube end of spherical shape. The standard reference material used is Al_2O_3 of about 0.0500 gram. The differential thermal measurement was performed on a Shimadzu DMA-50 from 283 to 1373 K, with temperature ramping rate of ten degree per minute and holding time of one minute. Two heating and cooling cycles were run to check reproducibility. About 0.0583 gram of $LaMnO_3$(B) sample was also measured with similar settings.

Qualitative results: Fig. 3.9 shows the raw data from DTA measurements on both samples. Sample $LaMnO_3$(A) shows rather pronounced thermal peaks across the JT transition ($\approx$ 735 K), and nonetheless distinguishable peaks across the orthorhombic to rhombohedral (OR) phase transition around $T_R\sim$ 1010 K. In contrast, the $LaMnO_3$(B) response from the JT transition appears around 660 K, and the peaks are rather weak and broad. No identifiable feature is visible across the expected second OR phase transition around 800 K. The phase transition temperature was estimated as the mean of the thermal peak positions during heating and colling [2]. By

[2]noting only qualitative analysis was carried out while proper DTA data analysis will require considerations of experimental factors such as the relative weight and specific heat of the reference

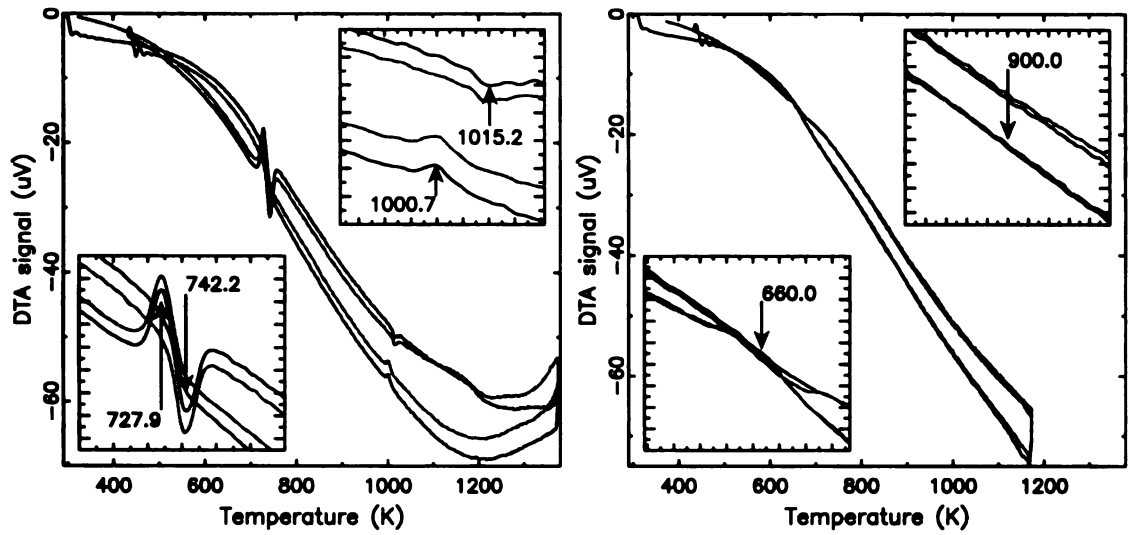

Figure 3.9: The DTA measurement data from sample $LaMnO_3$(A) (left panel) and $LaMnO_3$(B) (right panel).

doing this, we found the T_{JT} of $LaMnO_3$(A) sample is around 735 K, which is very close to the 750 K for the "perfect" stoichiometric sample. The T_R is around 1010 K, about the same as reported in the literature for the "perfect" stoichiometric sample. The quite weak signals from $LaMnO_3$(B) sample are somewhat surprising (as the excess O content is rather small, ≤ 0.006), suggesting the Mn^{4+} contents (due to excess oxygen) drastically affect both phase transitions. Those transition temperatures were further confirmed by our neutron powder diffraction experiments discussed later.

To summarize, the DTA measurements successfully located the two phase transition temperatures. The $LaMnO_3$(A) sample is shown to be very close to be stoichiometric, and the presence of small amount of Mn^{4+} should not compromise our studies. The $LaMnO_3$(B) sample appears to be less stoichiometric as expected. Still, it is very interesting to see how our microscopic structure results depend on the slight excess oxygen content.

material, the cooling rate, holding time, etc.

3.6.3 Neutron powder diffraction

To reliably determine the oxygen atom positions, i.e. Mn-O bond lengths, neutron powder diffraction data were collected, because of the much improved oxygen atom contrast compared to X-rays [5].

Sample $LaMnO_3$(A) was measured on the newly upgraded Neutron Powder Diffractometer (NPDF) [43] at Los Alamos Neutron Science Center (LANSCE) at Los Alamos National Laboratory. Powder sample of about 6 gram was sealed in a vanadium can suitable for high temperature measurements. A high temperature furnace was used to collect data at temperatures in the order of 300, 650, 700, 720, 730, 740, 750, 800, 880, 980, 1050, 1100, 1150, and 550 K. An additional data set at 300 K after the high temperature measurement was also collected in the displex to check for possible change of the sample after reaching as high as 1150 K. Each temperature point was measured for 3 hours which is found sufficient to provide good counting statistics. Sample $LaMnO_3$(B) was measured on the Special Environment Powder Diffractometer (SEPD) at the Intense Pulsed Neutron Source (IPNS) at Argonne National Laboratory (ANL). Powdered sample of about 10 gram was sealed in a cylindrical vanadium tube with helium exchange gas. Data were collected from 20 K to room temperature in a closed cycle helium refrigerator, and from room temperature to 805 K in a Howel furnance. Each temperature point was measured for 6 hours. In both experiments, calibrations runs such as the empty diffractometer, empty sample container can, and a vanadium rod standard were also measured for proper corrections of sample data.

3.6.4 Obtaining experimental PDFs

Program PDFgetN [42] was used to carry out many correction steps, such as the detector deadtime and efficiency, scattering background, sample absorption, multiple scattering, in-elasticity effects, and normalization by the incident flux and the total

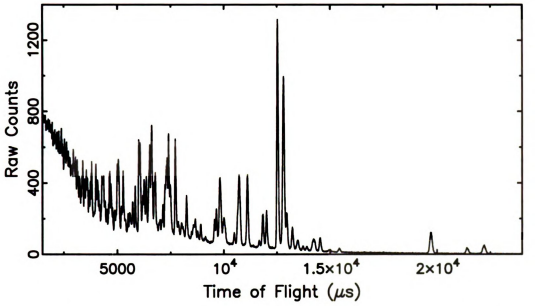

Figure 3.10: One example of experimental raw data from neutron powder diffraction. The x axis is the neutron time of flight (TOF), and y axis denotes the measured intensity.

sample scattering cross-section, to yield the total scattering structure function, $S(Q)$, where Q is the magnitude of the scattering vector. The PDF, $G(r)$, is then obtained by a sine Fourier transform according to

$$G(r) = \frac{2}{\pi} \int_0^\infty Q[S(Q) - 1] \sin Qr \, dQ. \tag{3.1}$$

Fig. 3.10 shows one example of the raw diffraction data directly coming from the experiments. Examples of $F(Q) = Q(S(Q) - 1)$ and $G(r)$ from both neutron experiments are shown in Fig. 3.11. Q_{max} of 32.0 Å^{-1} was used for $LaMnO_3$(A) NPDF data, while Q_{max} of 26.0 Å^{-1} for $LaMnO_3$(B) SEPD data. The 980 K NPDF data appeared to subject to fluctuating incident beam profiles during collection, and will be ignored in our data interpretations. All other PDFs show high quality. Extensive structural modeling immediately followed.

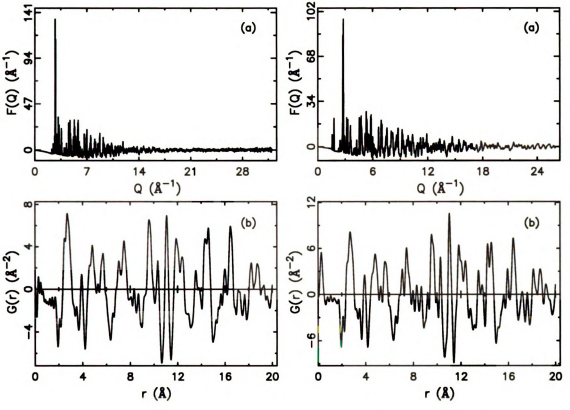

Figure 3.11: Left half shows the NPDF data from sample $LaMnO_3$(A) at 300 K and right half shows the SEPD data from sample $LaMnO_3$(B) at 300 K. The annotations are, (a) The experimental reduced structure function $F(Q) = Q(S(Q) - 1)$. (b) The experimental $G(r)$ obtained by Fourier transforming the data in (a).

3.6.5 Real space PDF refinement

PDFFIT [11], a real space non-linear least square regression refinement program, was used to fit structural models to all experimental PDFs. The real space distance r range of the experimental PDF used is 1.5 to 20.0 Å [3]. The initial structure model for the orthorhombic phase has space group *Pbnm*, with asymmetric cell made up of La (-0.0078, 0.049, 0.25), Mn (0.00, 0.50, 0.00), O1 (0.075, 0.49, 0.25), O2 (0.73, 0.31, 0.04). The high temperature rhombohedral R phase has space group $R\bar{3}c$ with its asymmetric cell comprising of La (0.0, 0.0, 0.25), Mn (0.00, 0.00, 0.00), O (0.44, 0.0, 0.25). Necessary constraints are properly set up manually to maintain the *Pbnm*

[3] The r_{max} of 20.0 Å PDF refinements already obtain the crystallographic structures in excellent agreement with Rietveld analysis

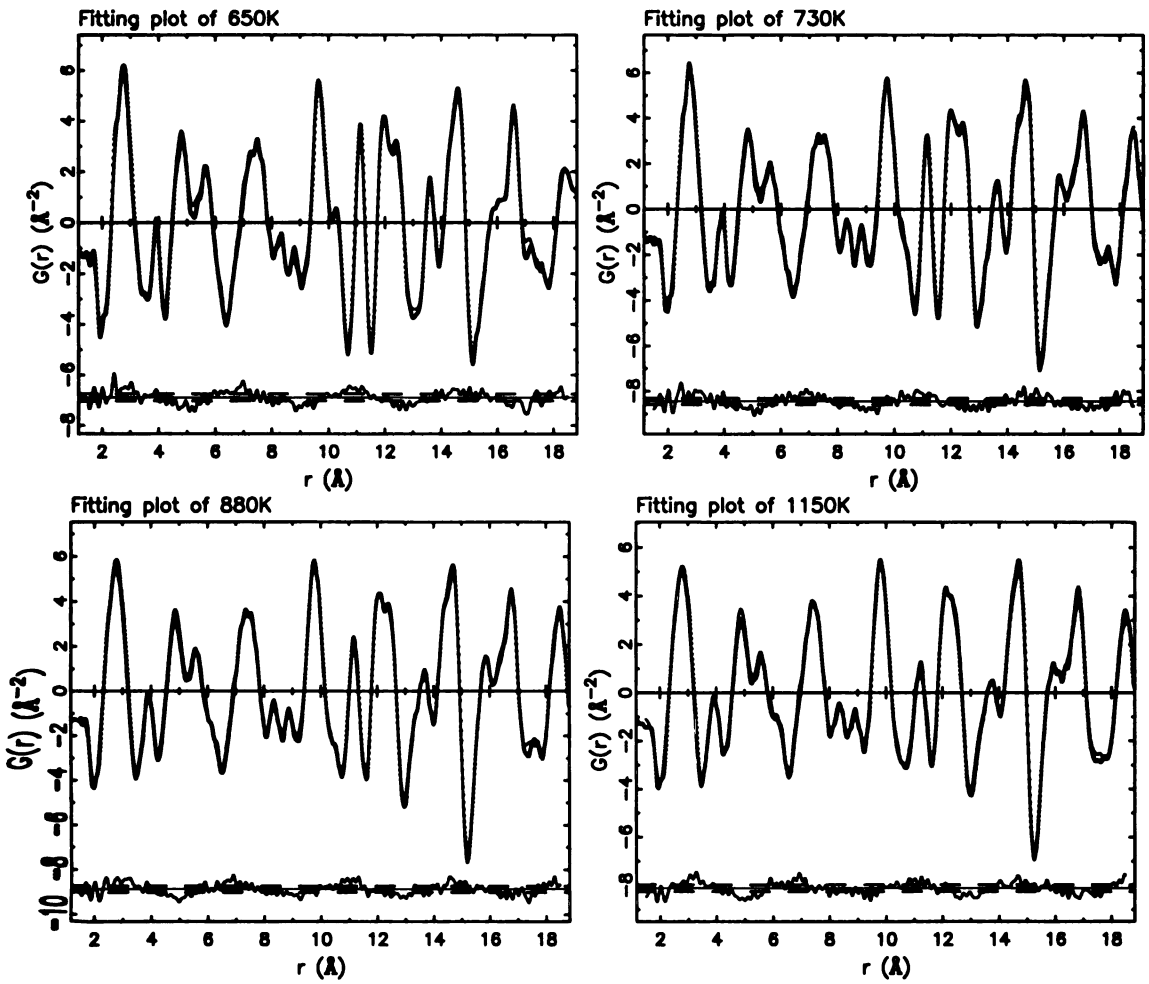

Figure 3.12: (upleft) The PDFFIT refinement results of sample $LaMnO_3$(A) data at 650 K, (upright) 730 K, (downleft) 880 K, (downright) 1150 K. Denotations are the following, the experimental $G(r)$ is shown as solid dots, and the calculated PDF from refined structural model is shown as solid line. The difference curve is shown offset below. The dashed lines show the estimated standard deviations due to finite counting statistics at 2σ level.

or $R\bar{3}c$ space group symmetry. This also means that special atomic positions are not refined. It is noteworthy that constraints can be set based on the atomic environments regardless of the space group, as PDFFIT assumes no inherent symmetry of the refined structure. Refined structure parameters include lattice constants, non-special atomic fractional coordinates, and isotropic thermal displacement parameters. Additionally, finite instrument resolution factor is modeled as the Q_{sig}, the full width at half maximum (FWHM) of the instrumental resolution function; the renormalization factor (scale factor) is also refined to account for small but non-negligible systematic errors during data analysis. All refinement agreements are rather good with R_{wp} values less than 0.10. Examples of the PDF refinement are shown in Fig. 3.12 and 3.13 for sample $LaMnO_3$(A) and (B), respectively.

In the difference curves shown in Fig. 3.12, sine wave like fluctuations are somehow apparent. A clearer plot is shown in Fig. 3.14(a). This is found to originate from the missing low Q Bragg peaks in $F(Q)$, which was directly sine Fourier transformed to obtain the $G(r)$. From Fig. 3.14(b), three peaks (first one is a doublet) are missing from the experimental $F(Q)$ with positions at 1.57, 1.61, and 1.77 $Å^{-1}$. With the known peak positions and the relative peak intensities estimated from the structure factors, the analytical formula of $s * \exp^{\frac{1}{2}(0.018r)^2} \cdot (200\sin(1.57r) \cdot 1.57 + 83\sin(1.61r) \cdot 1.61 + 38\sin(1.77r) \cdot 1.77)$ was fit to the difference curve. r is the real space distance. s is the scale factor as the only fitting parameter. The fit is shown in Fig. 3.14(c). The excellent agreement of the fit strongly indicates the missing Bragg peaks are the origin of the fluctuations in the difference curves. Subtraction of the fitted sine waves resulted in a much improved refinement as expected, which can be seen in Fig. 3.14(d).

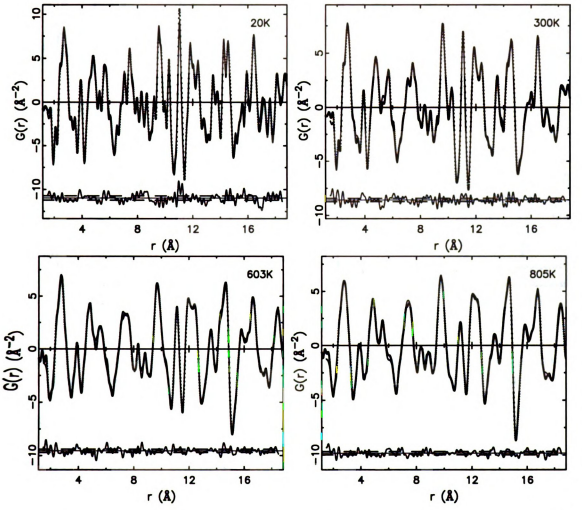

Figure 3.13: Examples of PDF refinement results at 20 K, 300 K, 603 K, 805 K of **sample** $LaMnO_3$(B). Denotations are the following, the experimental $G(r)$ is shown as **solid** dots, and the calculated PDF from refined structural model is shown as solid **line**. The difference curve is shown offset below. The dashed lines show the estimated **standard** deviations due to finite counting statistics at 2σ level.

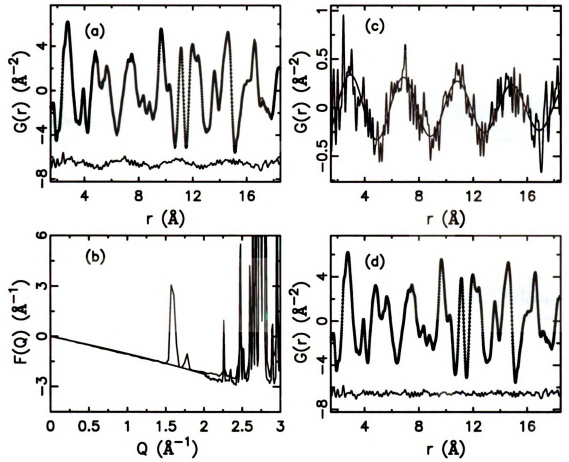

Figure 3.14: Demonstration of the consequence of missing Bragg peaks at low Q region of the experimental $F(Q)$ on later PDF refinement (see text for details).

3.6.6 Reciprocal space Rietveld refinement

Program GSAS [68], the general structure analysis system package, was used to carry out Rietveld analysis of Bragg peaks in reciprocal space. The Q range used is from 1.0 to 12.5 Å^{-1}. Only the two highest angle banks are refined. Initial structure models are the same as the aforementioned PDFFIT refinements, i.e. *Pbnm* and $R\bar{3}c$. For both NPDF and SEPD data sets, the lowest temperature data were first refined. Instrument and sample dependent parameters, such as diffractometer zero constants and peak profiles, are only refined at this initial step. Then, in the order of low to high temperatures, starting from the refined parameters of previous temperature, the following are refined: lattice constants, non special atomic fractional coordinates, and

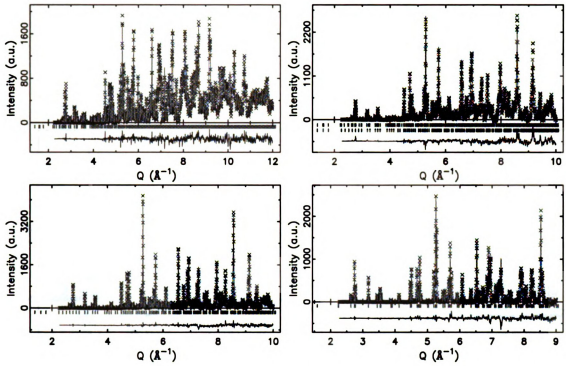

Figure 3.15: (upleft) The Rietveld refinement plot of bank 5 of 650 K $LaMnO_3$(A) data, (upright) 730 K, (downleft) 880 K, (downright) 1150 K. The annotations are: experimental observed intensities are shown as crosses (×); calculated pattern from crystallographic model is shown as solid line; their difference is shown offset below; Bragg peak positions are indicated by the short vertical bars.

isotropic thermal displacement factors. Background for each bank is approximated by a shifted Chebyschev polynomial with 7–12 terms (type 1 in program GSAS). Along the way, addition of the second phase or the change of space group was necessary near phase transition temperatures. Rather satisfactory agreements were achieved at all temperatures with χ^2 ranging from 2.0 to 5.0. Examples of Rietveld analysis are shown in Fig. 3.15 and 3.16 for sample $LaMnO_3$(A) and (B), respectively.

The sample $LaMnO_3$(A) after the high T measurement was also measured at 300 K at a later time in displex, to check whether the sample stoichiometry has changed during the high temperature measurement. Rietveld refinements were carried out on both 300 K data sets, and shown in Fig. 3.17. Between these two measurements, the crystal structures are identical, and the only different parameters are scale factors and scattering background. Both refinements have rather small χ^2 values, 2.46 (be-

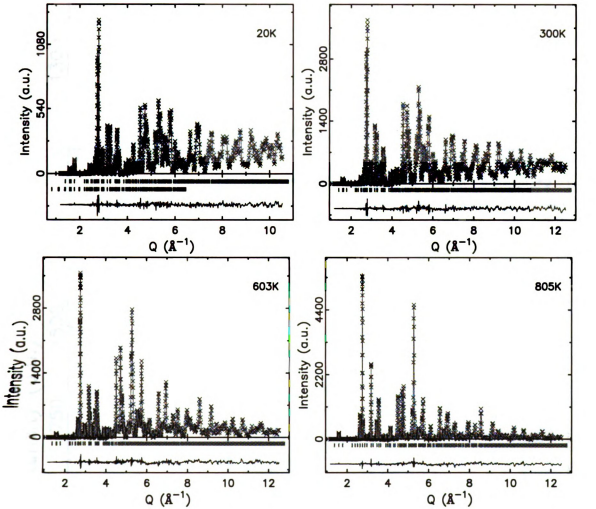

Figure 3.16: (upleft) The Rietveld refinement plot of bank 5 of 20 K $LaMnO_3$(B) **data**, (upright) 300 K, (downleft) 603 K, (downright) 805 K. The annotations are: **experi**mental observed intensities are shown as crosses (×); calculated pattern from **crystal**lographic model is shown as solid line; their difference is shown offset below; **Bragg** peak positions are indicated by the short vertical bars.

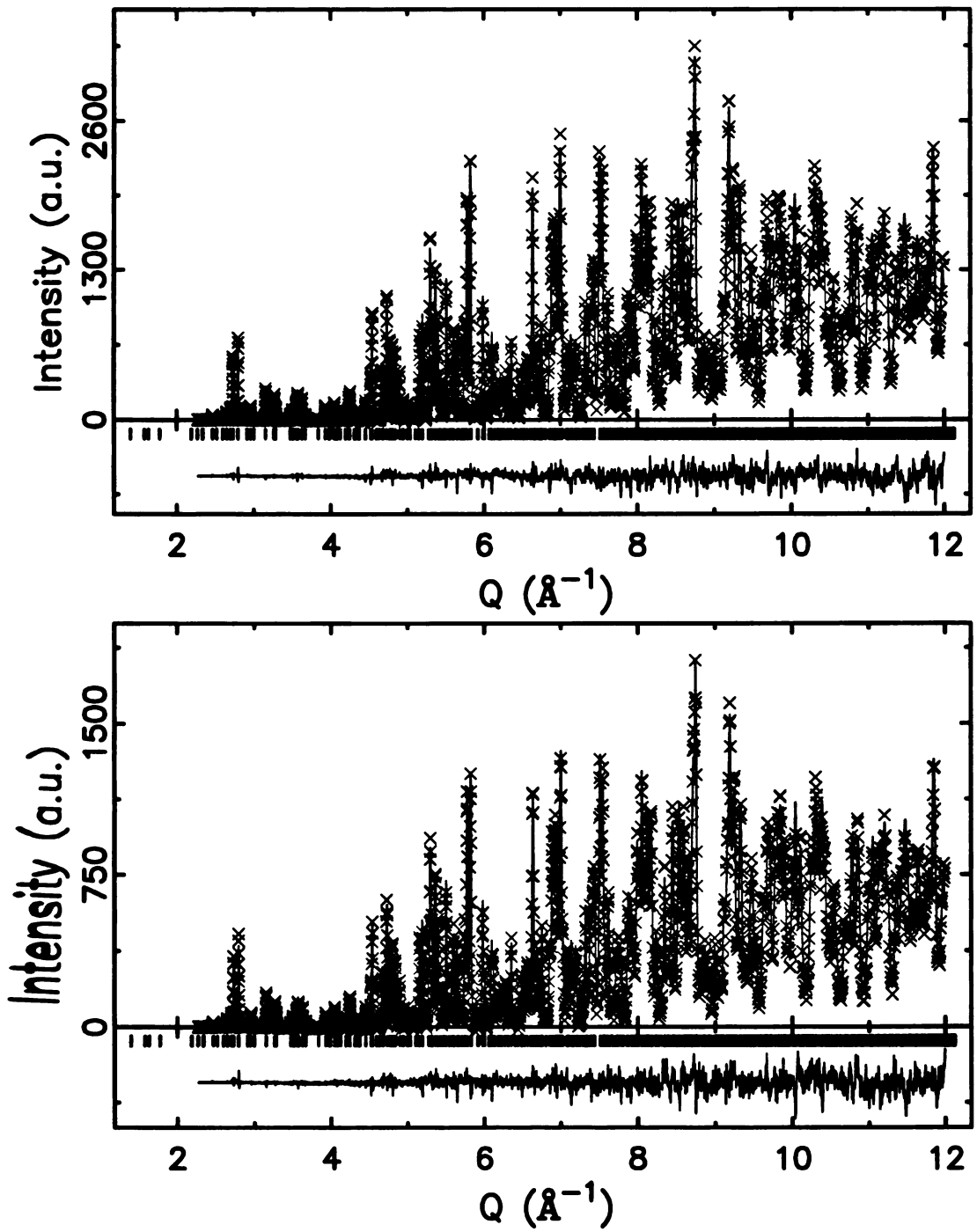

Figure 3.17: Comparison of the neutron powder diffraction pattern of sample $LaMnO_3$(A) between the beginning and end of the experiment. (left) Rietveld refinement of 300 K data before the high T measurement, (right) 300 K data after the high T measurement.

fore), 1.87 (after). Also in consideration that the measurement was all carried out in vacuum, we reached the conclusion that the sample stoichiometry had not changed during our experiment.

3.6.7 Model independent peak analysis

The PDF tells directly the distribution of inter-atomic distances regardless of the inherent lattice symmetry. Thus, even without a structure model, we are able to extract quantitative information about one or more specific bonds, such as the bond length and coordination numbers. To our advantage, usually only a few distinct peaks exist at the low r PDF region, corresponding to the few bonding lengths in the structure. It is generally more difficult to directly analyze the high r PDF peaks, which requires serious effort to decompose the contributions from many inter-atomic distances. With rather good accuracy [137, 138], PDF peaks are of Gaussian curve shape, along with the consideration of termination effects [18]. Therefore, we can simply fit the low r PDF peaks with a few Gaussian peaks, whose number corresponds to the number of distinct (and resolved) bond lengths. The obtained Gaussian peak profiles reveals the local structure details quantitatively. PWID and XYFIT (home written programs) are used for this purpose.

3.7 Local structure from PDF analysis

From now on, our discussion will focus on the experimental results from the sample $LaMnO_3$(A). The corresponding data from sample $LaMnO_3$(B) will be also shown side by side for comparison. Qualitatively, the two samples show behaviors in excellent agreement.

Local structure information is contained in low r PDF regions. Thus we show in Fig. 3.18(a) the low r region of the PDF, which directly reflects the Mn-O bond

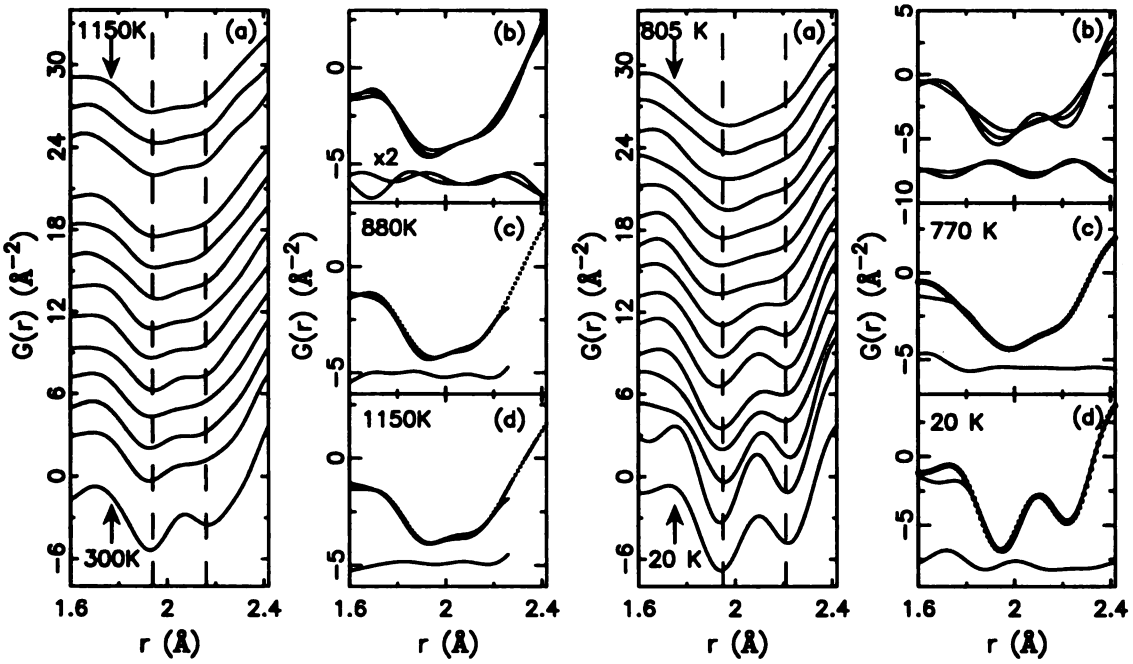

Figure 3.18: Left half (four panels) show the low r experimental PDF data from sample $LaMnO_3$(A). (a) Low r region of experimental PDFs at all temperatures shown with offsets. Positive y axis points to the increase of temperature. Two dashed lines indicate the Mn-O long and short bonds at 1.94 and 2.16 Å, respectively, (b) shown are the PDFs at 650, 720, and 880 K without offset. The differences between 650 and 720 K, 720 and 880 K are shown below offset. (c) fitting result of PDF data at 880 K with two Gaussian curves. Solid dots denote the experimental data. Solid line denotes fitted curve. Plotted below is the difference curve. (d) fitting result of PDF data at 1150 K with annotations as in (c).
Right half (four panels) show the low r experimental PDF data from sample $LaMnO_3$(B). (a) low r region of the PDF at all temperatures shown with offsets. Positive y axis points to the increase of temperature. (b) low r region of the PDFs at 300 K, 517 K, and 770 K are shown. The differences between 300 K and 517 K, 517 K and 770 K are shown below. (c) fitting result of PDF data at 770 K with two Gaussian curves. Solid dots denote the experimental data. Solid line denotes fitted curve. Plotted below is the difference curve. (d) fitting result of PDF data at 20 K with annotations as in (c).

length distributions. It should be first noted that Mn-O peaks are upside-down due to the negative Mn neutron scattering length [5]. In the low temperature O' phase, the JT distorted MnO_6 octahedra are ordered in the staggered pattern as illustrated by Fig. 3.7. This perfect long range ordering results in identical local and average structure. Consequently, we should observe the four shorter and two longer Mn-O bonds in experimental PDFs (the two short and two medium bonds can not be resolved directly). The low temperature PDFs in Fig. 3.18(a) clearly show the Mn-O doublet at 1.94 and 2.16 Å, e.g. the 300 K data at the bottom of Fig. 3.18(a).

Within the low temperature O' phase, increasing the temperature will enhance the atomic thermal motions, which in turn will broaden PDF peaks [5]. This is what we see by comparing the bottom five PDFs in Fig. 3.18(a). Across the JT transition at $T_{JT}\sim$ 735 K, the average crystallographic structure indicates nearly regular MnO_6 octahedra. If this is also true for the local structure, the first Mn-O PDF doublet peak should turn into a single peak around 2.0 Å. However, the experimental PDFs show the opposite: the Mn-O doublet persists above JT transition. The long Mn-O peak does not separate itself from the more pronounced short Mn-O peak, however, is clearly evident as the high r shoulder. The splitting remains larger than the thermal broadening of the peaks. This behavior extends into the highest temperature measured. As our local structure data covered the high temperature R phase for the first time, the local JT distortion is then discovered to exist in R phase as well. The PDFs at low r region show qualitatively and intuitively that the JT distortion survives at all temperatures. The peaks do broaden at higher temperature due to increased thermal motion [5] and the two contributions to the doublet are not resolved at high temperature. However, it is clear that the peak is not a broad, single-valued, Gaussian at high temperature as predicted from the crystallographic models.

We would like to see if there is any change in the peak profile on crossing the T_{JT} beyond normal thermal broadening. To test this we plot the change in this

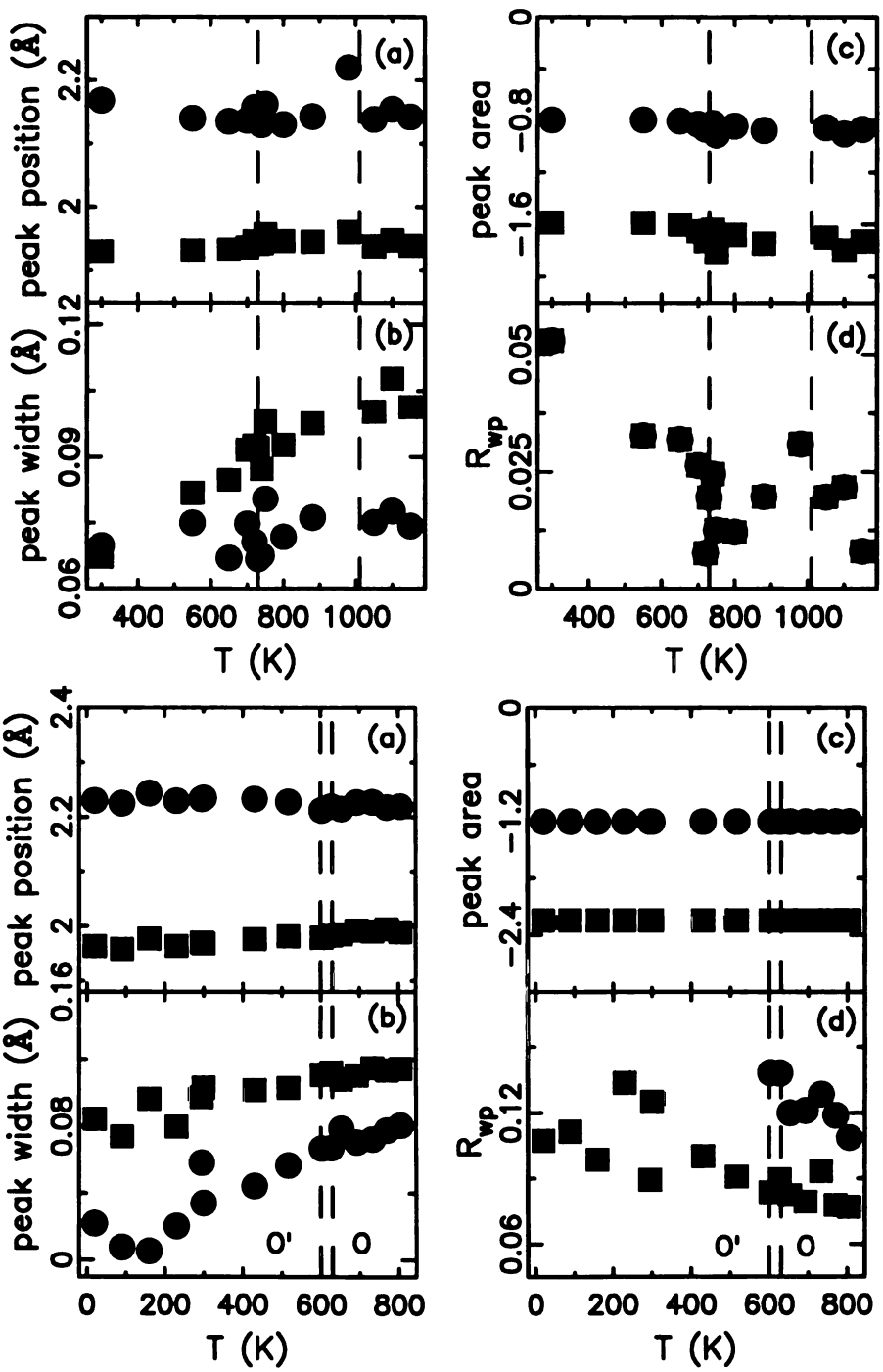

Figure 3.19: Extracted peak profile parameters from the double Gaussian curve fitting. Upper half is from sample $LaMnO_3$(A); lower half is from $LaMnO_3$(B). The low r peak is shown as filled squares, while the high r peak is shown as filled circles: (a) peak positions, (b) peak widths, (c) peak area, (d) R_{wp}.

nn Mn-O peak between T=720 K and T=880 K, as it crosses T_{JT}, and compare this to the change in the peak on going from 650 K to 720 K. The latter case has approximately the same temperature differential (thermal broadening will be the same) but there is no structural transition in that range. The difference curves from these two situations, shown in Fig. 3.18(b), are almost identical. We conclude that there is virtually no change to the MnO_6 octahedra as they go from the O' to the O phase. It is noteworthy that the shape of the difference curves mimics the typical differences between two Gaussian with different widths.

Finally, to quantify the nature of the local JT distortions, we have fit two Gaussian peaks to the nearest-neighbor MnO_6 doublet in the experimental data at all temperatures. The quality of the fits at "low" (880 K) and high (1150 K) temperature are rather good, as can be seen in Fig. 3.18(c) and (d). The position and width of each peak, and the total integrated intensity of the doublet, were allowed to vary (the intensities of the long and short bond distributions were constrained to be 1:2 in the fits). The weighted residual factor R_{wp} varies from 1% at high temperature to 5% at low-temperature indicating excellent agreement over all temperatures. Attempts to fit a single Gaussian in the O phase resulted in significantly worse agreements. The results of the temperature-dependent fits are shown in Fig. 3.19.

No anomaly of any kind can be identified across the T_{JT}=735 K. The integrated intensities and peak positions do not change significantly with temperature from 300 K to 1150 K indicating that the average bond-lengths of the short- and long-bonds in the JT distorted octahedra are rather temperature independent. The peak widths increase slightly with temperature due to increased thermal motion (Fig. 3.19(b)); however, there is no clear discontinuity in the peak broadening associated with the phase transition. The broader low r peak (larger peak width) seems to come from the fact that two Mn-O bonds (two short and two medium) contribute to it, while the high r peak only comes from the two long Mn-O bonds. The results confirm that

the local JT distortions persist, virtually unstrained, into the O and R phases.

To summarize here, we first confirmed the earlier XAFS results [129, 130] and establish that in the O phase the full JT distortion persists in the local structure. Second, we show for the first time that the high temperature R phase (T$\geq$ 1010 K) is also locally fully JT distorted. Both qualitative and quantitative analysis has been carried out.

3.8 Average structure from the PDF and Rietveld analysis

3.8.1 Crystallographic phase determination

Both PDF refinements over a wide r range and Rietveld refinements result in a crystallographic model to represent the average structure. The average structure here means that it is obtained by spatially averaging over all cells, which can be all the same as in perfect crystals, or different in the presence of disorder. As the detailed average structures have been reported in the literature [136, 126, 139], only brief results will be shown. We first show the lattice constants in Fig. 3.20. According to convention, $c/\sqrt{2}$ is shown in the orthorhombic phase for easy comparison with a and b. The "equivalent" $c_{eq} = c/\sqrt{2}$ for the rhombohedral phase is obtained from the relations: $a_H = b_O, b_H = \frac{1}{2}(a_O - b_O - c_O), c_H = 2a_O + c_O$. So that $18c_{eq}^2 = c_H^2 + 12a_H^2$, where the subscripts H and O denote the orthorhombic and rhombohedral phase, respectively. The experiment data clearly show the JT transition temperature T_{JT} around 735 K for $LaMnO_3$(A), and 610 K for $LaMnO_3$(B), indicated by vertical dashed lines in Fig. 3.20, where the sample goes from the O' into the O (pseudo-cubic) phase. It is worth mentioning that the transition temperatures are in good agreement with earlier DTA results. Refined values from PDF refinements are plotted as filled symbols, while

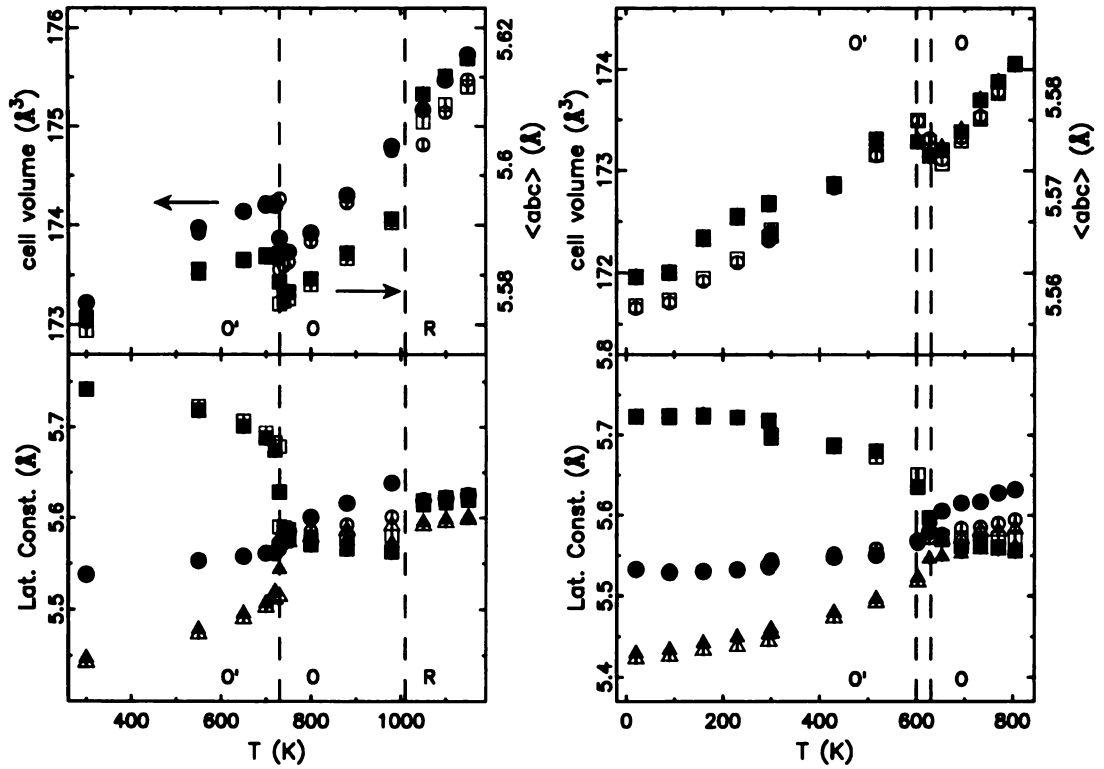

Figure 3.20: Results from $LaMnO_3$(A) are shown in the left panel; while $LaMnO_3$(B) in the right. Both PDF (filled symbols) and Rietveld (open symbols) refined values are shown. (up) The unit cell volume (•) and the average of three lattice constants (■) as a function of temperature. (down) The lattice constants a(■), b(•), and $c/\sqrt{2}$(▲).

the Rietveld refined values are shown as open symbols. They appear to be in excellent agreement. It is interesting that the three lattice constants a, b, and $c/\sqrt{2}$ become a little more separated with increasing T after T_{JT}. The cell volume is shown in the upper panel of Fig. 3.20. One striking feature is the collapse of cell volume across the JT transition, which is believed to be from the orbital disorder above JT transition. The same reason is believed to account for the decrease of the average of the three lattice constants (to be discussed later). For sample $LaMnO_3$(B), the seemingly rather large JT transition temperature difference of 150 K from only 0.006 (nominal value) excess O atoms is in fact somewhat expected. For example, a T_{JT}=600 K was observed by Norby *et al.* in a slightly non-stoichiometric $LaMnO_{3.005}$ [136].

Another signature of this JT transition is the disappearance of the MnO_6 octahedral JT distortion upon warming. Fig. 3.21 shows how the three "orthogonal"

Mn-O bond lengths within one MnO_6 octahedron, their average, and the MnO_6 octahedral volume evolve with temperature. Clearly, in the low T O' phase, the MnO_6 octahedron is fully JT distorted with two long, two medium, and two short bonds. This is not contradicting the local structure results where only *two* Mn-O bonds were observed. The reason is that the short and medium Mn-O bonds are not directly resolved in the experimental PDFs, as the Mn-O peak is shown as a doublet (not a triplet) in Fig. 3.18. It is the same reason why *one* Gaussian curve was used to fit these *two* shorter bonds (in Fig. 3.19). It is also self-consistent that the low r Gaussian curve appears to have an area twice as large as the high r one. In the average structure, upon the JT transition, the difference between those long and short bonds reduces drastically, which is what we expect from this O' to O (pseudo-cubic) phase transition. The JT transition is confirmed to be orbital order-disorder type as the local JT distortion persists at all temperatures. The anomalous change of the Mn-O bond lengths in the average structure comes from the orientational disorder of the distorted MnO_6 octahedra in the O phase, while the MnO_6 octahedra always lay their long Mn-O bonds in the *ab* plane in the O' phase. In both Fig. 3.20 and 3.21, the OR transition of the sample $LaMnO_3$(A) is also identified to occur around 1010 K in agreement with early DTA results. In the R phase, MnO_6 octahedra are strictly normal with six equi-distant Mn-O bonds, and the lattice symmetry becomes hexagonal. No anomaly is observed on the cell volume, however, the volume of the MnO_6 octahedron collapses again. This most probably indicates the structure experiences two relaxation steps: JT and OR transition. The lattice relaxation introduces more disorder, and thus results in "seemingly" reduced volumes across both phase transitions.

Therefore, both the JT and OR phase transitions have been confirmed on our samples, and are consistent with the published literatures. Average structure analysis with combined PDF and Rietveld methods has been shown to have quantitative

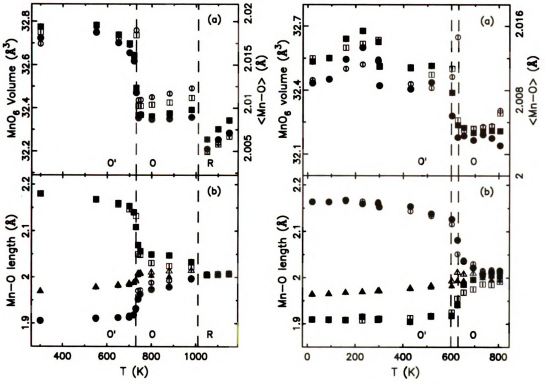

Figure 3.21: Results from $LaMnO_3$(A) are shown in the left panel; and $LaMnO_3$(B) in the right. Both PDF (filled symbols) and Rietveld (open symbols) refined values are shown. (up) The MnO_6 octahedral volume, and the average of three Mn-O bond lengths as a function of temperature. (down) The long, medium, and short Mn-O bonds.

agreement. $LaMnO_3$ in high temperature O and R phases shows no JT distortion on the average structure. In the context of the existence of local JT distortions at all temperatures, the O and R phases are orbital disordered.

3.8.2 Lattice structure parameters

In the following, we will show other extracted structural data coming from the average structural analysis. The isotropic atomic displacement parameters are shown in Fig. 3.22. Basically, La shows rather normal temperature dependence, while Mn experiences a small jump only across the JT transition. Only O atoms show significant increase of U_{iso} across both the JT and OR transitions. Rietveld results indicate this anomaly on both O atoms, while PDF results only suggest the in-plane O atom. In

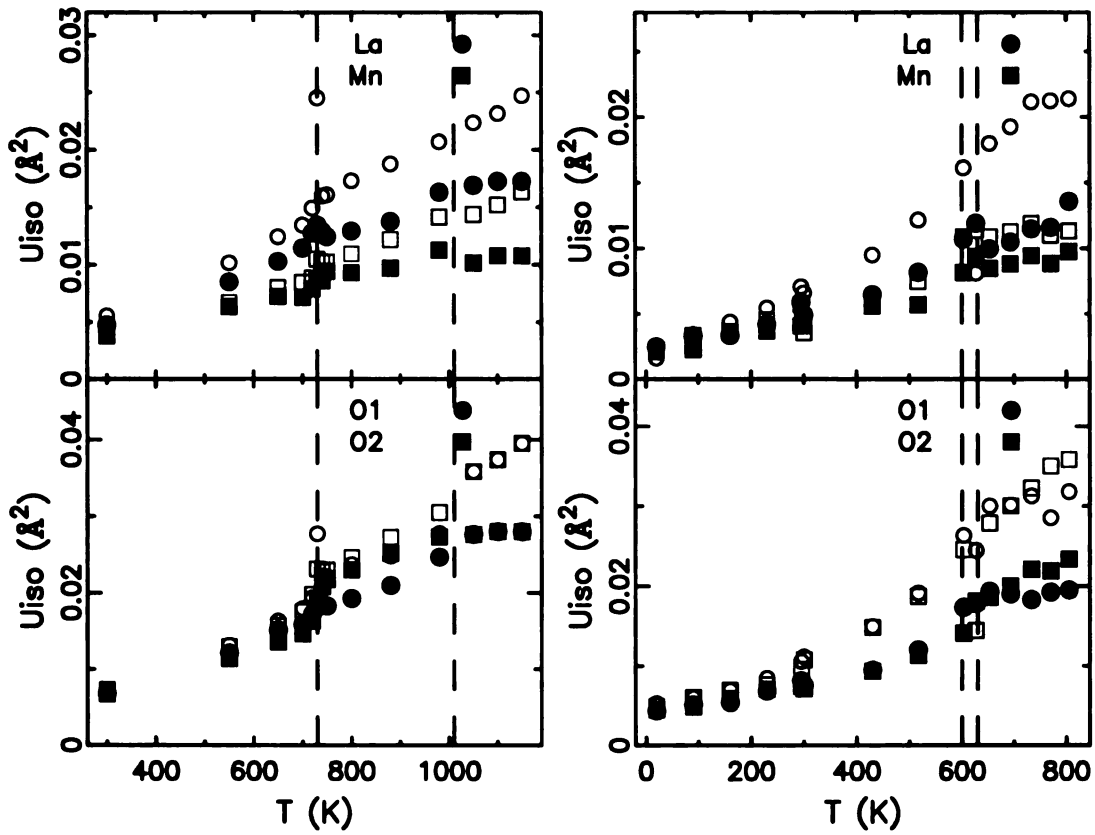

Figure 3.22: Results from $LaMnO_3$(A) NPDF data are shown in the left panel; while $LaMnO_3$(B) SEPD data in right. Both PDF (filled symbols) and Rietveld (open symbols) refined values are shown. Data represent the isotropic atomic displacement parameters for all atoms in the asymmetric cell (La, Mn, O1, O2).

both refinements, the U_{iso} of both O atoms are released/refined at the same time, not one by one. This should rule out the side effect of parameter fitting orders. The discrepancy between the quantitative values between PDF and Rietveld refinements has been discussed in Ref. [41]. The excess increase of O atom thermal displacement parameters is consistent with the scenario of increasing disorders across both transitions.

The lattice and MnO_6 octahedron appear to be more metrically normal upon increasing temperature. We can define some geometric parameters to characterize the distortions in the following. The lattice orthorhombicity factor D is defined as

$$D = \frac{a-b}{a+b}, \tag{3.2}$$

where a and b are the in-plane lattice constants. The distortion parameter Δ of a coordination polyhedron MO_N is

$$\Delta = \frac{1}{N}\sum_{i=1}^{N}\{(b_i - \langle b\rangle)/\langle b\rangle\}^2, \tag{3.3}$$

where b_i is the i^{th} M-O bond length and $\langle b\rangle$ is their average. One important parameter frequently quoted in the literature is the tolerance factor defined as

$$\Gamma = \frac{b_{A-O}}{\sqrt{2}b_{Mn-O}}, \tag{3.4}$$

where b_{A-O} is the distance between the A site and the nearest oxygen, and b_{Mn-0} the average Mn-O bond length. In a perfect cubic system, the tolerance factor Γ is equal to 1.0. We show the above defined parameters in Fig. 3.23. The main result is the reduction of lattice distortions in the O and R phases. Anomalies are evident across the JT transition, while OR transition appears to be a rather smooth crossover. The tolerance factor Γ is approaching the "perfect system" value from below (noting that $\Gamma > 1.0$ is not possible), but does not reach 1.0 even at the R phase.

The smaller than unity tolerance factor Γ also means that the MnO_6 octahedra have to tilt for self accommodating in the lattice matrix. In the orthorhombic phase, there are two Mn-O-Mn angles, while only one in the R phase. Those Mn-O-Mn angles are not 180 degrees due to the tilt of MnO_6 octahedra around the pseudo-cubic [111] direction. The average tilt angle $\langle\varphi\rangle$ can be computed from the two Mn-O-Mn angles θ_1 and θ_2 by

$$\cos\theta_1 = \frac{2 - 5\cos{\varphi_1}^2}{2 + \cos{\varphi_1}^2}, \tag{3.5}$$

$$\cos\theta_2 = \frac{1 - 4\cos{\varphi_2}^2}{3}, \tag{3.6}$$

and $\langle\varphi\rangle = (\varphi_1 + \varphi_2)/2$. Another set of angles of interest is between the O-Mn-

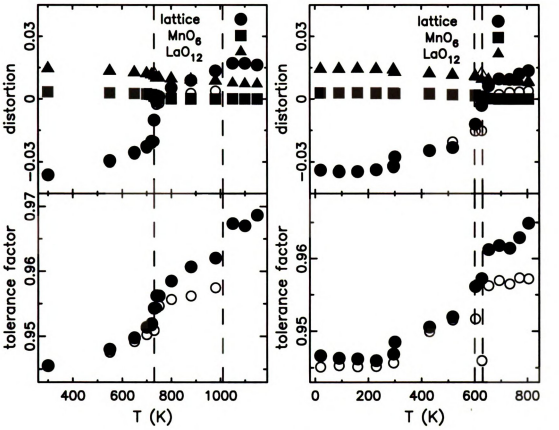

Figure 3.23: Results from $LaMnO_3$(A) NPDF data are shown in the left panel; while $LaMnO_3$(B) SEPD data in the right. Both PDF (filled symbols) and Rietveld (open symbols) refined values are shown. (up) The distortion parameters for lattice, MnO_6 octahedron, and LaO_{12} polyhedron. (down) The tolerance factor Γ.

O triplets within one MnO_6 octahedron. Fig. 3.24 shows the development of these angles with temperature. We need to mention that for these results, the *Pbnm* model was used in PDF refinements of the R phase, which actually has a higher symmetry $R\bar{3}c$. If space group $R\bar{3}c$ is used in PDF refinements, the same results were obtained as from the Rietveld refinements. The use of lower symmetry group *Pbnm* for the R phase aimed to look for local structure motifs, which would otherwise be constraint by the $R\bar{3}c$ symmetry. The trend is that Mn-O-Mn angles are getting more "straight", i.e. approaching 180 degrees. However, change of the average tilt angle φ is not drastic, and does not show anomalous decrease upon either phase transition. We thus can not simply attribute the change of lattice constants and Mn-O bond lengths

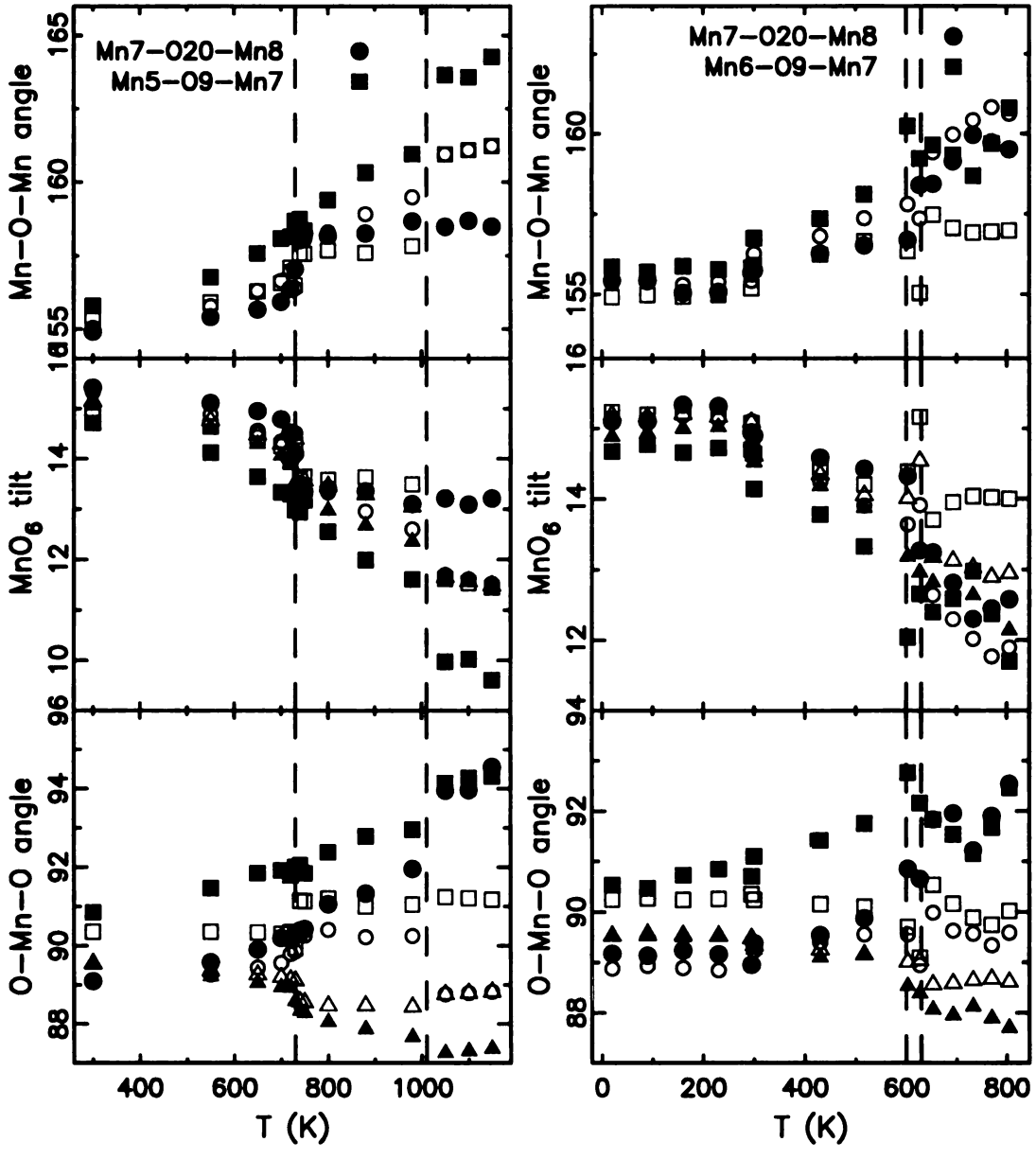

Figure 3.24: Results from $LaMnO_3$(A) NPDF data are shown in the left panel; while $LaMnO_3$(B) SEPD data in right. Both PDF (filled symbols) and Rietveld (open symbols) refined values are shown. (up) the two Mn-O-Mn angles θ_1 and θ_2, (middle) the MnO_6 octahedral tilt angles φ_1, φ_2 (■, •), and their average $\langle\varphi\rangle$ (▲) (down) the O-Mn-O angles within one MnO_6 octahedron.

without careful thoughts. The exact picture can not be obtained without knowing the local structure in disordered systems (discussed later). The O-Mn-O angles are rather intriguing. The Mn-O bonds are not orthogonal even in the O' phase, probably due to the lattice strains. However, this non-orthogonality seems to increase with increasing temperature, and shows a jumping at the JT transition. We think this is an indication of increasing lattice strain in the high temperature phases.

The MnO_6 octahedral JT distortion has been characterized by the normal JT modes such as $Q_2 = 2(l-s)/\sqrt{2}$ and $Q_3 = 2(2m-l-s)/\sqrt{6}$, where the l, s, m are the long, short, and medium Mn-O bond lengths. The ground-state wave functions Ψ_g and Ψ_e in the e_g state are given [140, 141, 82] by

$$\Psi_g = c_1\phi_{x^2-y^2} + c_2\phi_{3z^2-r^2}, \tag{3.7}$$

$$\Psi_e = c_2\phi_{x^2-y^2} - c_1\phi_{3z^2-r^2}, \tag{3.8}$$

where c_1 and c_2 are coefficients obtained from relations: $\tan\varphi = Q_2/Q_3$ and $\tan\varphi/2 = c_1/c_2$. The self-normalization condition $c_1^2 + c_2^2 = 1$ should also be satisfied. In the absence of octahedral distortions, we should obtain $c_1 = c_2 = 0.7071$, i.e. orbitals $\phi_{x^2-y^2}$ and $\phi_{3z^2-r^2}$ are degenerate. Those parameters are shown in Fig. 3.25. Both Q_2 and Q_3 values approach zero as the MnO_6 octahedral JT distortion diminishes, which is as expected. As the Q_2 mode is more pronounced at low T, the $\phi_{3z^2-r^2}$ orbital is more preferably occupied, as is evident from the large c_2 values. Upon increasing T and reducing the average MnO_6 JT distortion, c_1 and c_2 merge to the equal probability value of 0.7071. Above T_{JT}, c_1 and c_2 values are not physically meaningful, as the distortion is essentially gone as from the average structure.

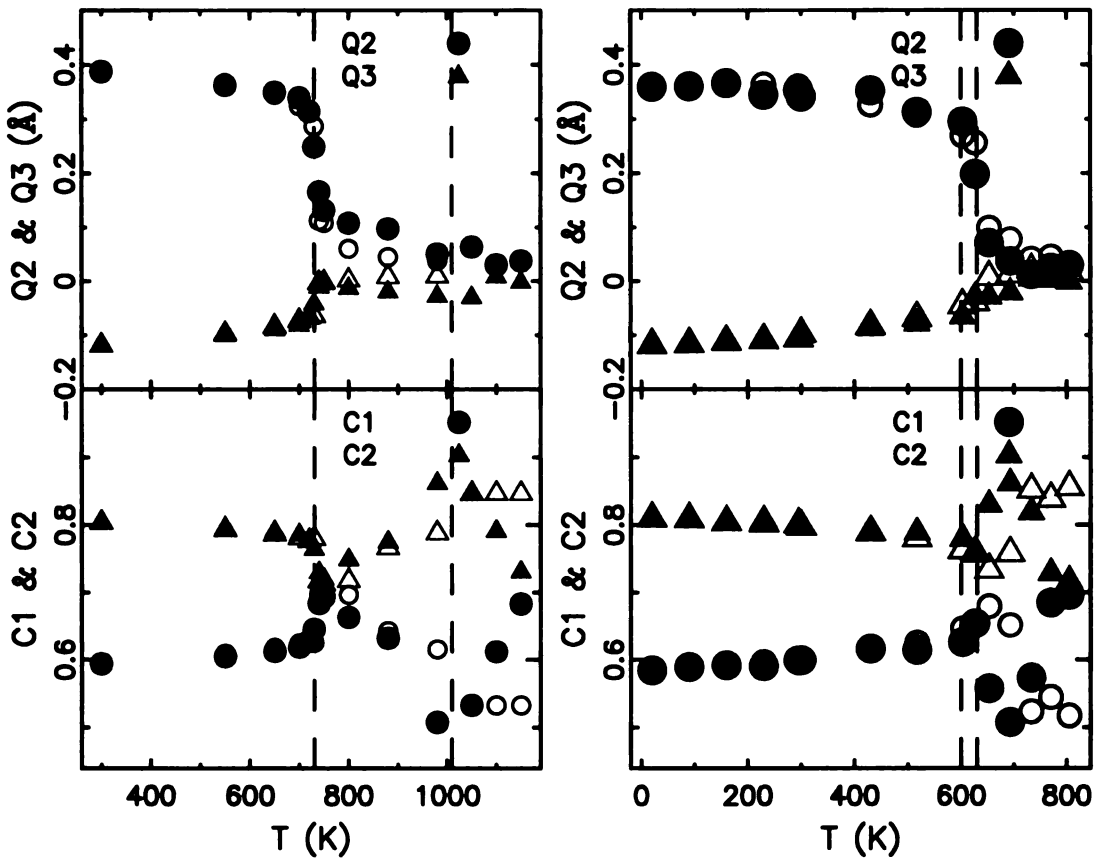

Figure 3.25: Results from $LaMnO_3$(A) NPDF data are shown in the left panel; while $LaMnO_3$(B) SEPD data in right. Both PDF (filled symbols) and Rietveld (open symbols) refined values are shown. (up) The Q_2 and Q_3 values, (down) the c_1 and c_2 values.

3.8.3 Summary

In summary, our average structure analysis has established the crystallographic JT and OR phase transition of our samples. Obtained transition temperatures from our neutron powder diffraction and DTA data are in good agreement. PDF wide r range refinements and Rietveld analysis give quantitatively consistent results. Below T_{JT}, MnO_6 octahedra are fully JT distorted with two long, two short, and two medium Mn-O bonds. The e_g orbitals order in a staggered pattern, giving the significantly orthorhombic O' phase. Across the JT transition, the lattice enters the O (pseudo-cubic) phase where the MnO_6 distortion is drastically reduced, though not completely removed. The OR transition completes the removal of MnO_6 JT distortions, and leads

to the more symmetric hexagonal phase ($R\bar{3}c$).

3.9 Intermediate structure from PDF analysis

Fits to the nearest neighbor Mn-O peaks show a large JT distortion in the O phase, whereas crystallographically the MnO_6 octahedra are almost regular (six equal bonds). This implies that the average structure results from a loss of coherence of the ordering of the JT distorted octahedra and that the JT transition is an orbital order-disorder transition. The locally JT distorted MnO_6 octahedra orient the long bonds randomly along three main axis. Thus, on the average, the lattice appears to be pseudo cubic, and the MnO_6 octahedron appears to be almost regular. However, the placements of the long bonds of neighboring MnO_6 octahedra are not independent, because of the shared oxygen atom. It would cost too much lattice elastic energy (strain) to have two long bonds aligned back to back. An anti-ferrodistorsive first-neighbor interaction has to be considered, maybe a weak second neighbor interaction as well. Thus, we expect locally JT distorted MnO_6 octahedra to form small short-range ordered clusters ("polarons"), and the cluster size ("correlation length") depends on the relative strength of the JT distortion and the lattice stiffness.

In principle we can test the extent of any orbital short-range-order in the PDF by refining models to the data over different ranges of r. Fits confined to the low-r region will yield the local (JT distorted) structure whereas fits over wider ranges of r will gradually cross over to the average crystallographic structure. To extract the size of the short-range ordered clusters, we have fit the PDF from $r_{min} = 1.5$ to r_{max}, where $5 < r_{max} < 20$ Å [4]. This was done for all data-sets. The model used at all temperatures was the low-temperature structure in the *Pbnm* space group. Representative results are shown in Fig. 3.26 as open circles The amplitude of the refined JT distortion is constant as a function of r_{max} at 300 K (Fig. 3.26(a)) reflecting

[4] r_{max} of 20 Å is found to already give the crystallographic results.

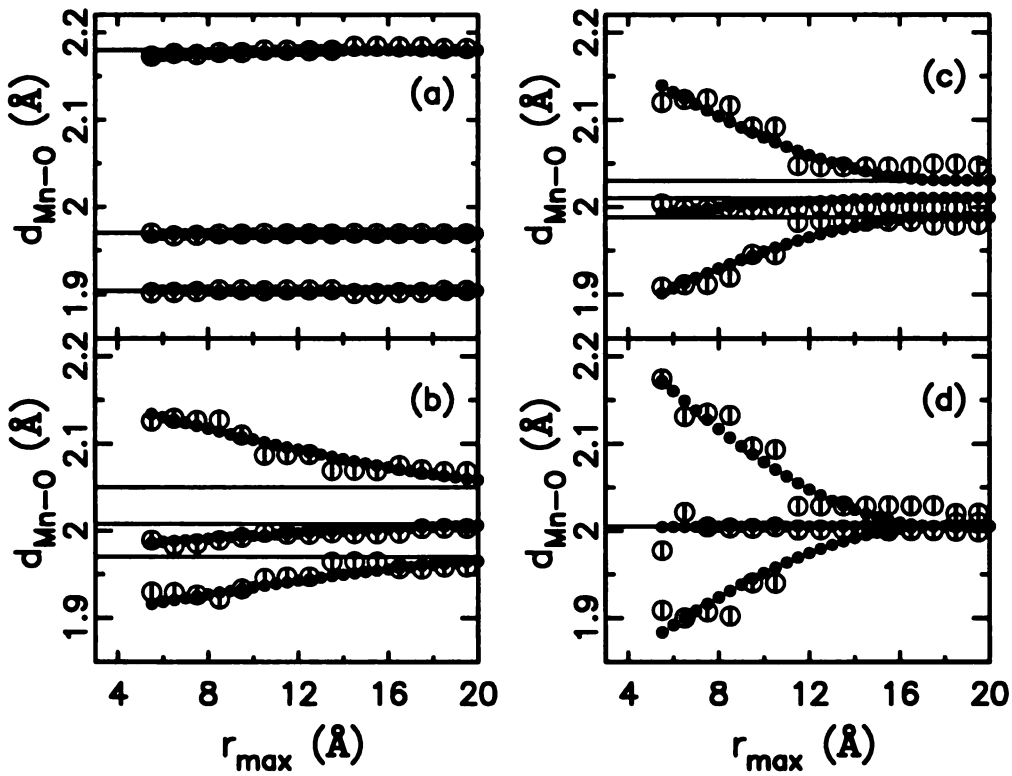

Figure 3.26: Mn-O bond lengths from the refined structure model as a function of r_{max} are shown as open circles, and the corresponding fits with the PDF form factor of a solid sphere is shown as filled circles. The horizontal lines indicate the Mn-O bond lengths from Rietveld refinements. (a) 300 K, (b) 740 K, (c) 800 K, (d) 1100 K (see text for details).

the fact that the orbital order is perfectly long-range. Regardless of the range fit over, the full JT distortion is recovered. At higher temperature, and especially in the O' phase the amplitude of the refined distortion falls off smoothly as the fit range is extended to higher-r, until it asymptotically approaches the much smaller crystallographically refined value (Fig. 3.26(b,c,d)). We understand this behavior in the following way. Domains of local orbital order exist in the O phase. These may resemble the pattern of orbital order at low temperature, and for convenience this is how we have modeled them; however, we cannot rule out the possibility that another type of orbital order exists as we have not done an exhaustive search and compared different models. These domains do not propagate over long range and are

orientationally disordered in such a way that, the observed pseudo-cubic structure is recovered on average. We can estimate the domain size by assuming that the orbitals are ordered inside the domain but uncorrelated from one domain to the neighboring domain. This results in a fall-off in the amplitude of the refined distortion with increasing fit range with a well defined PDF form-factor [142], assuming spherical domains, that depends only on the diameter of the domain. The three curves of refined-bond-length vs. r_{max} from the short, medium and long bonds of the MnO_6 octahedron could be fit at each temperature with the diameter of the domain as the *only one* parameter. Representative fits are shown in Fig. 3.26 as the filled circles, evidencing rather good agreements.

The temperature dependence of this domain size is shown in Fig. 3.27. We find that in the pseudo-cubic O phase these clusters have a diameter of $\sim$ 16 Å independent of temperature except close to T_{JT} where the size grows. Below T_{JT} the correlation length of the order is much greater, although some precursor effects are evident in the data just below T_{JT}. The refined domain size of orbital order is similar in the R-phase though the quality of the fits becomes worse in this region. This may be because the nature of the short-range orbital correlations changes, i.e. different from the O' phase. Domain size of $\sim$ 16 Å spanning over four MnO_6 octahedra suggests the JT distortion has strong first nearest neighbor coupling, and weak second nearest neighbor coupling.

3.10 Discussion and conclusions

We now address the issue of the unit-cell volume collapse observed crystallographically [134]. This is most readily explained if charges are delocalizing resulting in more regular MnO_6 octahedra and a smaller unit cell, as observed at higher doping in the $La_{1-x}Ca_xMnO_3$ system for example [23]. This appears to be borne out by our detailed Rietveld results on the same data which indicate that the volume contraction

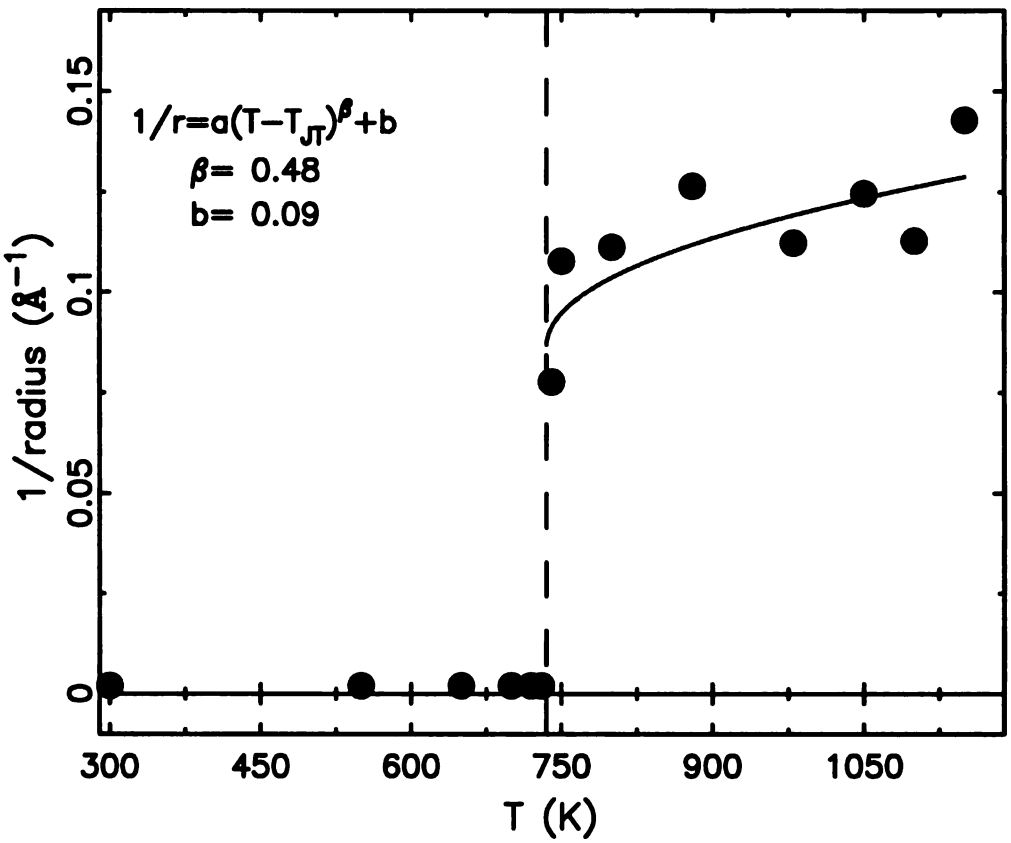

Figure 3.27: The inverse of the domain radius as a function of temperature is shown as the filled circles. The dashed line indicates the JT transition temperature. The solid line is a fit with the formula shown in the upper left corner.

occurs as a result of a shortening of the average Mn-O bond length, $\langle r_{Mn-O} \rangle$. This is shown in Fig. 3.21(a)s where the results of both Rietveld and wide-r-range PDF fits are in excellent agreement and show the rapid shortening of $\langle r_{Mn-O} \rangle$. Detailed calculations show that the volume reduction of MnO_6 octahedra accounts for the full volume reduction of the unit cell, i.e. LaO_{12} polyhedron does not show significant volume reduction at all. However, we have clearly shown that *locally* the MnO_6 octahedra do not change their shape and $\langle r_{Mn-O} \rangle$ is independent of temperature. The volume collapse must therefore have another physical origin. The most likely scenario is an increase in octahedral tilting amplitude, although none is seen in the average octahedral tilt angle. To test this, we made a $\sqrt{2} \times \sqrt{2} \times 1$ supercell so as to decompose the O atom's thermal displacement parameters along directions parallel and

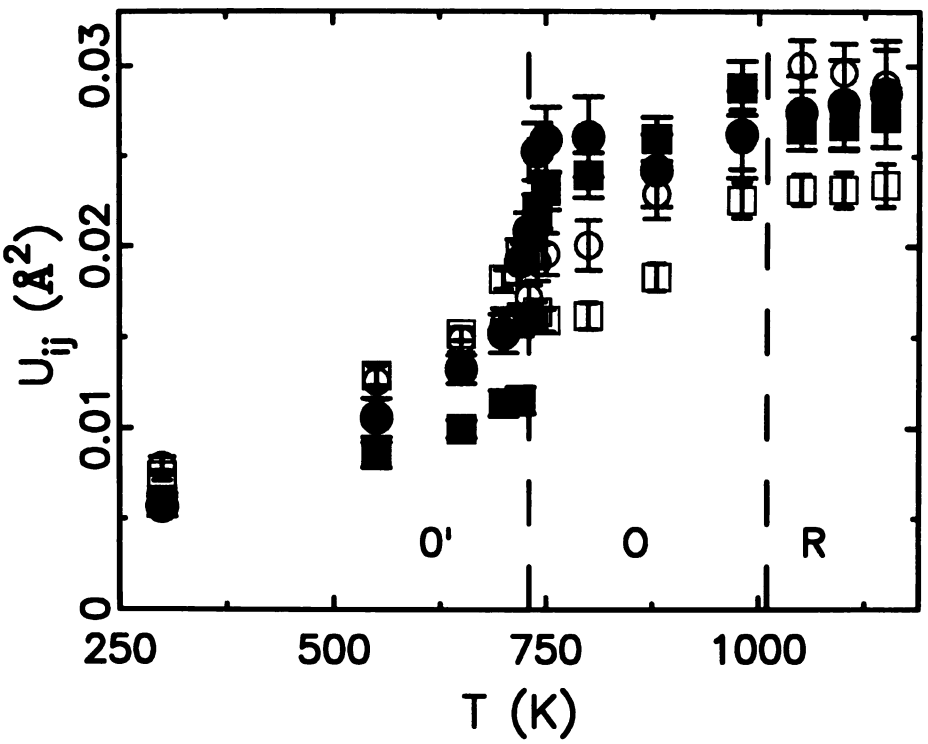

Figure 3.28: The thermal displacement parameters of oxygen atoms parallel and perpendicular to Mn-O bonding directions. Filled symbols (•, ■) are the parallel; open symbols are the perpendicular.

perpendicular to the Mn-O bonds. Fig. 3.28 shows the refinement results. It is clear that a jump in the oxygen displacement parameters, refined over a wide range in the PDF, is seen at T_{JT} consistent with the appearance of increased, but disordered, tilt amplitudes. The change in the average tilt angle that is necessary to accommodate the collapse in unit cell volume is just 0.4 degree (cell volume decreases by 0.38% across T_{JT}). Note that a sharp increase is seen in the components of the oxygen displacement parameter both parallel and perpendicular to the Mn-O bonds. This is expected due to the disordered distribution of the Mn-O long bonds as well as the increased inhomogeneous tilting that is required to accommodate the short-range ordered orbitals.

It may become necessary to discuss the somewhat counter-intuitive decrease of the

$\langle r_{Mn-O} \rangle$ upon warming in the average structure, while the local structure analysis shows it to actually slightly increase as expected from the normal thermal expansion. The local structure PDF analysis gives the physical distance between atomic pairs (i.e., the Mn and O atoms in this case) without any assumption about the long range ordered structure. The average structure analysis first assumes one crystallographic unit cell with some symmetry, then obtains the the average position of each atom in the unit cell. Therefore, the position of each atom is averaged before the atomic pair distance is calculated. The average structure analysis will give the physical atomic pair distances in the perfect crystalline materials. However, these distances may not represent the real physical values in the presence of structural disorder. This is in fact what occurs in the high temperature $LaMnO_3$ phases. Locally JT distorted MnO_6 octahedra lay their long bonds randomly along each crystallographic axis. The three Mn-O bond lengths thus approach their averaged value across the JT transition. Still, this does not explain the decrease of the $\langle r_{Mn-O} \rangle$, as none of the three Mn-O bonds shorten across the JT transition. In the mean time, the average of the lattice constants also decreases. The angle between the Mn-O bonds and the corresponding crystallographic axis has to increase for this to happen, i.e., an increase of the MnO_6 octahedral tilting angle. As mentioned in the previous paragraph, an increase of 0.4° of the tilting angle is sufficient to account for the decrease of the decrease of $\langle r_{Mn-O} \rangle$ as well.

The sudden decrease of resistivity across the JT transition is still somewhat puzzling. As the nature of the JT transition is orbital order to disorder, we would expect the more disordered state has lower conductivity due to the increased scattering by the "defects". Apparently, this is not the case, and there has to be some other physical origin. Zhou and Goodenough [132, 143, 144, 145] have proposed a vibronic model where small fractions of Mn^{3+} disproportionate into Mn^{2+} and Mn^{4+}. While this charge disproportionation improves the conductivity, the JT distortions of those

involved MnO_6 octahedra also disappears. Though our PDF studies strongly suggest the fully JT distorted MnO_6 octahedra at all temperatures, the error bar of a few percent in our analysis may be incapable of resolving such small fractions. This author thinks the dynamic JT nature of the high T phases may offer an explanation to the sudden increase of conductivity. In the scenario of dynamic JT distortions, the MnO_6 octahedron is constantly changing its shape, which means the e_g electron is moving around at least inside one octahedron. This e_g electron jumping is supposed to be a slow process as our neutron powder diffraction study (energy resolution $\sim$ 20 meV) sees the fully distorted state. Nevertheless, due to the non-ionic nature of the Mn-O bonding, we would expect the e_g electron to possibly hop to its neighboring octahedron, thus increasing the conductivity. Particularly in the case of short range JT distortion correlations in the *O* and *R* phases, this gives the "large polaronic transport" picture.

To conclude, we have used a diffraction probe of the local atomic structure, neutron pair distribution function (PDF) analysis, to see if the local and average behaviors can be reconciled and understood. This method allows quantitative structural refinements to be carried out on intermediate length-scales in the nanometer range. We confirm that the JT distortions persist locally at all temperatures, and quantify the amplitude of these *local* JT distortions. No local structural study exists of the high-temperature rhombohedral R-phase that exists above $T_R = 1010$ K. We show for the first time that even in this phase where the octahedra are constrained by symmetry to be undistorted, the local JT splitting is constant. Fits of the PDF over different r-ranges indicate that locally distorted domains have a diameter of $\sim$ 16 Å with four MnO_6 octahedra spanning the locally ordered cluster. The unit cell volume collapse seen crystallographically comes from a reduction in the average Mn-O bond-length; however, this quantity is constant with temperature in the local structure. We show that the observed volume reduction is consistent with increased octahedral rotational

degrees of freedom. We speculate that local clusters of the low-T structure form on cooling at T_R but are disordered and align themselves along the three crystal axes. These domains grow, and the orbital ordering pattern becomes long-range ordered below T_{JT}.

Chapter 4

Local Structure of the Bi-layered Manganite $La_{2-2x}Sr_{1+2x}Mn_2O_7$ in the Mn^{4+} Rich Region

4.1 The bi-layered manganite:$La_{2-2x}Sr_{1+2x}Mn_2O_7$

The bi-layered manganite $La_{2-2x}Sr_{1+2x}Mn_2O_7$ is the $n = 2$ member of the so-called Ruddlesden-Popper series $A_{n+1}Mn_nO_{3n+1}$, while the "cubic" compound $LaMnO_3$ is the $n = \infty$ end member. The crystal structure of the bi-layered manganite is shown in Fig. 4.1. This system appears to be a prospective candidate for future technological application by showing a large colossal magneto-resistance (CMR) effect [146], and has been widely studied [147]. This compound consists of double layers of corner shared MnO_6 octahedra (perovskite structure type) separated by one rock-salt layer of (La,Sr)-O. Common to many transition-metal oxides with perovskite-related structures, the interplay between spin, charge, and lattice degrees of freedom is of critical importance [148]. Their delicate interactions result in a rich and interesting, but somewhat poorly understood, phase diagram [149, 150]. The bi-layered manganite system $La_{2-2x}Sr_{1+2x}Mn_2O_7$ shows behavior qualitatively similar to the cubic

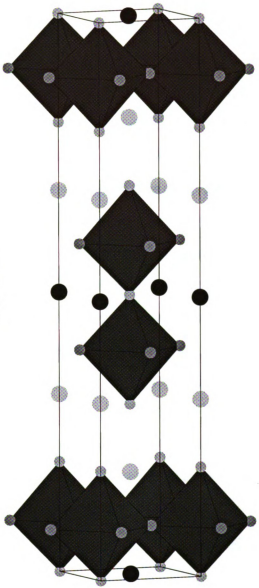

Figure 4.1: Crystal structure of the bi-layered manganite $La_{2-2x}Sr_{1+2x}Mn_2O_7$. It consists of double layers of cornered shared MnO_6 octahedra, which are separated by one rock-salt layer of (La,Sr)-O.

CMR manganites and is particularly interesting to study because of the extra factor of its reduced dimensionality. This material is also thought to be a good candidate for applications because its low dimensionality increases the ferromagnetic critical fluctuations close to the paramagnetic-ferromagnetic transition that are important for the CMR phenomenon. The reduced dimensionality obtained by constraining the lattice degree of freedom in this bi-layered system also facilitates the investigation of strong correlations between electron-lattice coupling and magnetic properties, proving it to

be one of the most interesting CMR manganites [147].

The crystallographic structural and magnetic phase diagram of $La_{2-2x}Sr_{1+2x}Mn_2O_7$ is shown in Fig. 4.2. The tetragonal unit cell with space group $I4/mmm$ is found in all Sr doping levels, except between $x = 0.76$ and $x = 0.94$ where the tetragonal and orthorhombic (space group I/mmm) structural phases coexist. The most heavily studied region is between $x = 0.30$ and 0.42, where the important CMR phenomenon and the temperature driven Insulator-Metal (IM) transition are observed [146]. The pioneering work of Moritomo *et al.* [146] discovered a Curie temperature of 126 K for this bi-layered compound at $x = 0.40$. The observed magneto-resistance (MR) ratio at the Curie temperature reached as high as 200% under 0.3 Telsa magnetic field, significantly higher than in the equivalent 3D Sr-based compound. The large MR effect was also reported for the $x = 0.3$ compound [151]. Ling *et al.* [150] have used temperature dependent neutron powder diffraction to systematically map out the magnetic and structure phase diagram in wide Sr-doping range of $0.3 \leq x \leq 1.0$, which serves as the basis to the more modern version shown in Fig. 4.2. While the paramagnetic state appears at high temperatures at all doping levels, the ground states of this bi-layered compound show very interesting magnetic structures. Fig. 4.3 shows the schematic diagrams of the magnetic phases. The magnetic coupling between the double layers of MnO_6 octahedra (inter-layer) is significantly weaker than intra-layer, giving quasi-2D magnetic interactions. We will get into more details of the different structural and magnetic phases in the regions of interest in the sections followed. Please refer to Ref. [150] for others. Most studies have focused on the Mn^{3+} rich portion ($x < 0.5$) of the $La_{2-2x}Sr_{1+2x}Mn_2O_7$ phase diagram, particularly because of the observed CMR phenomenon. However, the phase diagram of the less studied Mn^{4+} rich region shows many novel and intriguing properties, and is the subject of this chapter.

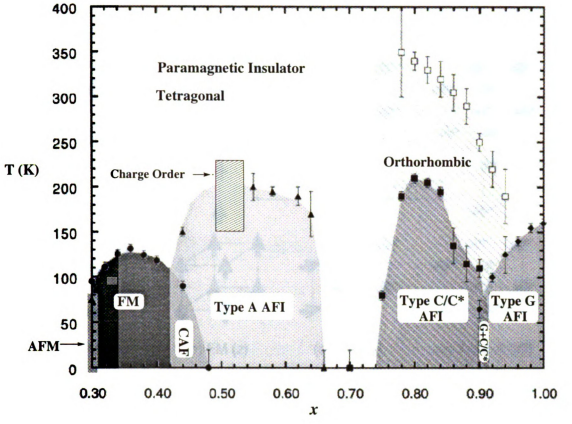

Figure 4.2: Magnetic and crystallographic phase diagram of $La_{2-2x}Sr_{1+2x}Mn_2O_7$. Solid data points represent magnetic transitions determined from neutron powder-diffraction data (antiferromagnetic Neel temperature T_N, ferromagnetic Curie temperature T_C, charge-ordering temperature T_{CO} , and orbital ordering temperature T_O). Open data points represent crystallographic transitions. Lines are guides to the eye.

4.2 Orbital occupancy transition at $x = 0.54$

4.2.1 Introduction to the question

In manganite systems close to 50% doping ($Mn^{3.5+}$) charge and orbital ordering is very common [152, 153, 154, 155]. This is understood as an interplay between coulombic and lattice strain degrees of freedom [99]. Charges disproportionate towards Mn^{3+} and Mn^{4+} and form a lattice on every second site. The occupied orbitals also order so as to lower the energy of the system. In the cubic manganites the occupied orbital results in a longer Mn-O bond as a result of the Jahn-Teller distortion. These elongated $d_{3z^2-r^2}$

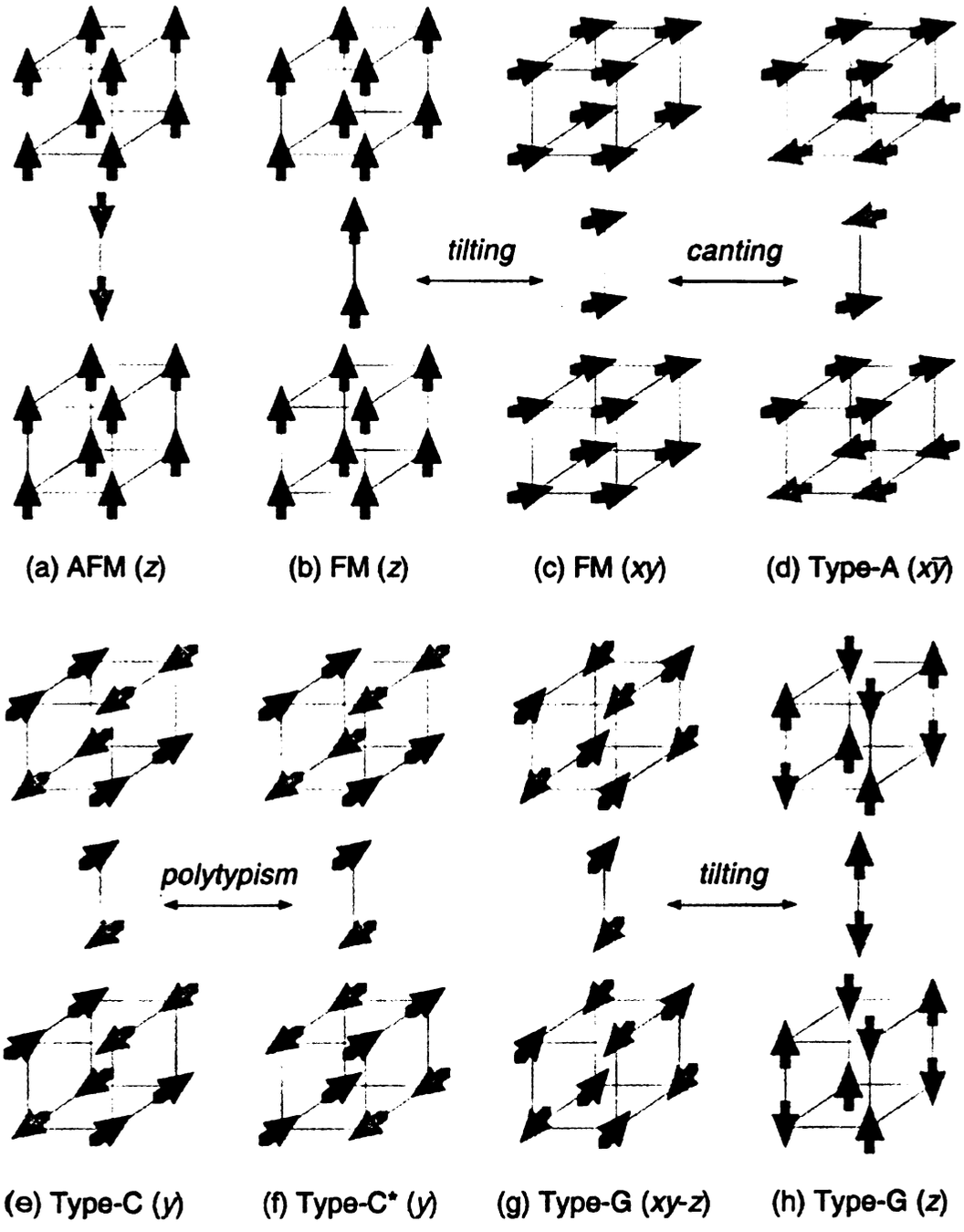

Figure 4.3: Schematic illustrations of magnetic structures of $La_{2-2x}Sr_{1+2x}Mn_2O_7$, arrows representing spin orientations on Mn sites: (a) AFM, (b) FM at $x = 0.32$, (c) FM at $x = 0.40$, (d) type-A AFI, (e) type-C AFI, (f) type-C^* AFI, (g) type-G AFI at $x = 0.92$, and (h) type-G AFI at $x = 1.00$. Taken from Ref. [150].

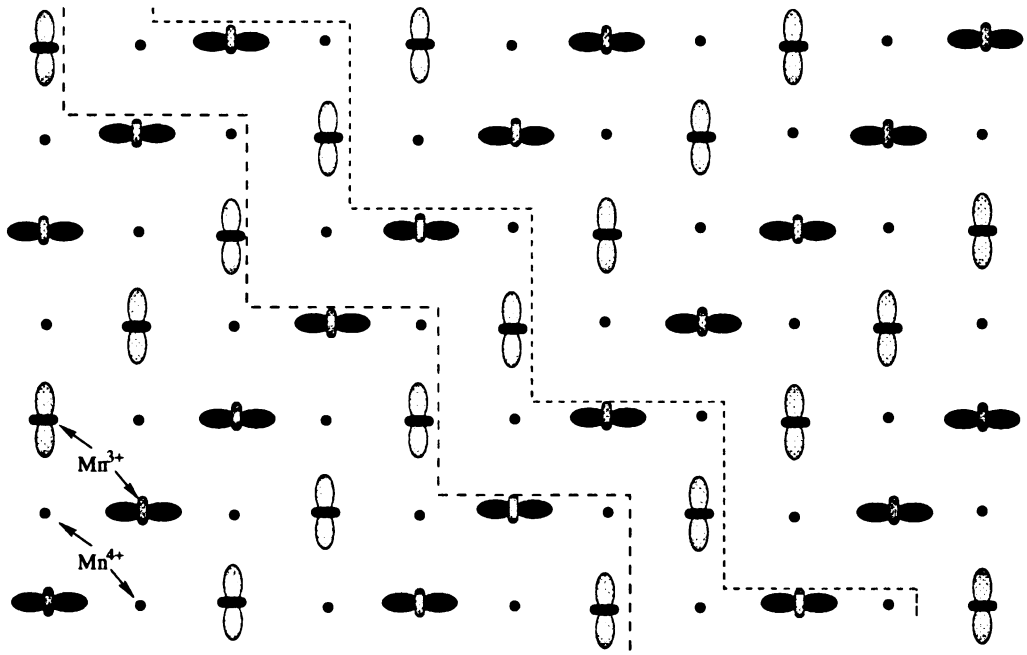

Figure 4.4: Cartoon representation of type CE charge ordering in manganites. The solid dots (•) are the Mn^{4+} ions. Shown orbitals are the occupied $d_{3(x,y)^2-r^2}$ orbitals of Mn^{3+} ions. Dashed lines indicate the ferromagnetic zigzag chains coupled antiferromagnetically.

orbitals, ($\sigma = x,\ y,\ z$), lay down in a crystallographic plane (shown in Fig. 4.4) and form a zig-zag pattern resulting in the CE magnetic ordering arrangement [152, 156, 154]. The simple, semi-empirical, understanding for this behavior comes from the Goodenough-Kanemori rules [81, 82].

In common with the cubic manganites, CE charge and orbital-ordering is observed in this bi-layered compound close to 50% doping (nominal $Mn^{3.5+}$ charge, in this case composition $LaSr_2Mn_2O_7$) [153, 154], appearing at 210 K on cooling. However, in contrast to the cubic manganites the ordering disappears again around 170K and the sample has an A-type antiferromagnetic insulating ground-state. A-type magnetic ordering is observed in undoped and lightly doped cubic manganites and consists of ferromagnetic planes that are antiferromagnetically coupled along the c-axis. In the undoped manganites this state is easily understood in the framework of the Goodenough-Kanemori (G-K) rules [81, 157]. However, at the high doping levels

of this sample it is inconsistent with these rules, as we discuss below.

The G-K rules give a simple road-map for understanding the diverse magnetic ground-states observed with changing doping in the manganite systems. It is assumed that charges reside in particular d-orbitals (and their associated covalent bonds with neighboring oxygen atoms). A particular orbital can then be considered as "filled" or "empty" (though in reality this disproportionation of charge will not be complete). The network of Mn ions is then considered. The Mn e_g d-orbitals point towards neighboring Mn ions through the nearest neighbor oxygen ions. When two filled, or two empty, orbitals point towards each other the coupling is locally antiferromagnetic due to superexchange through a (nearly) 180° Mn-O-Mn bond. When a filled orbital points towards an empty one, double-exchange results in a local ferromagnetic interaction. The orbitals can then order to produce long-range magnetic order of different types according to these local interactions. For nominal Mn charge of 3.5, the G-K rules straightforwardly lead to the CE structure. The elongated, occupied, $d_{3x^2-r^2}$ and $d_{3y^2-r^2}$ orbitals form a zigzag chain with ferromagnetic correlations along the chain. Each zigzag chain is then coupled antiferromagnetically with its neighboring chain, and also with the chain residing in the layer above (refer to the OO cartoon representation shown in Fig. 4.4). In contrast, in the undoped cubic manganites the occupied $d_{3x^2-r^2}$ or $d_{3y^2-r^2}$ exist on every site and form into a checkerboard pattern. In this case, in the plane, a filled orbital always points towards an empty one resulting in 2-D ferromagnetic correlations in the plane (see Fig. 3.7). The orbitals pointing perpendicular to the plane are all empty $d_{(x,y)^2-z^2}$ resulting in antiferromagnetic correlations between neighboring planes and therefore A-type antiferromagnetism.

The problem comes when one tries to explain A-type antiferromagnetism at 50% doping. Here we have to take these orbitals and tile a plane when half of the sites are Mn^{4+} in such a way as to have alternating filled and empty orbitals. In fact, it is possible if the electrons change their usual $d_{(x,y)^2-z^2}$ orbital occupancy to $d_{x^2-y^2}$.

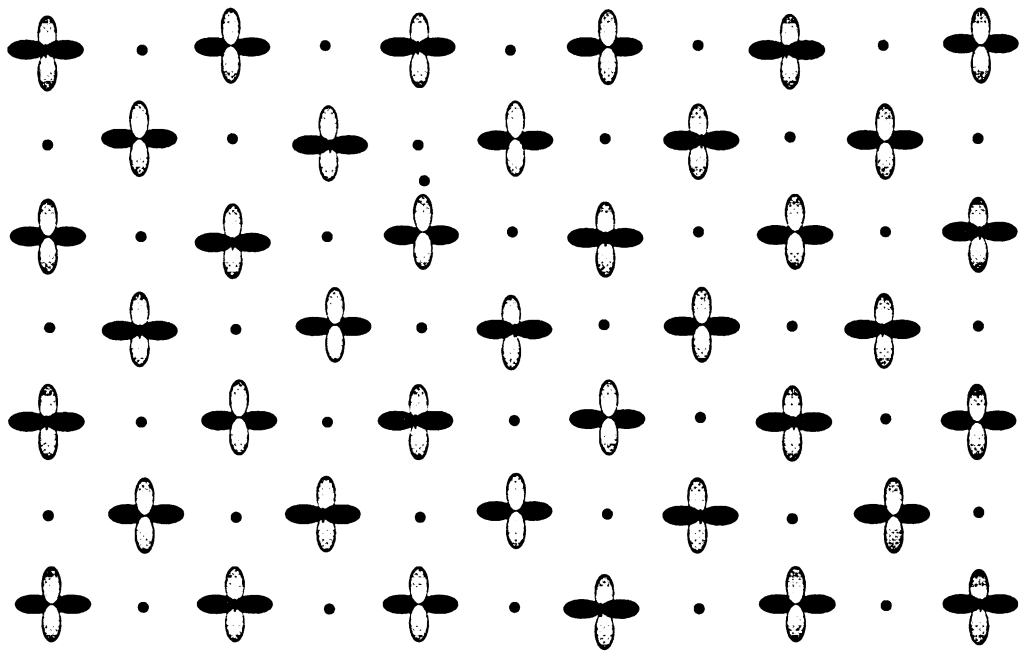

Figure 4.5: Illustration of the in-plane $d_{x^2-y^2}$ orbital occupancy in half doped $La_{2-2x}Sr_{1+2x}Mn_2O_7$. The solid dots (•) are the Mn^{4+} ions. Shown orbitals are the occupied $d_{x^2-y^2}$ orbitals of Mn^{3+} ions.

The MnO_6 octahedron distorts due to the JT effect that breaks the degeneracy of the $d_{3z^2-r^2}$ and the $d_{x^2-y^2}$ e_g orbitals (where x, y and z can be permuted depending on the orientation of the octahedron). In general, in the manganites the $d_{3z^2-r^2}$ orbital is stabilized and becomes occupied and elongated. However, it is possible given different external perturbations, such as crystal field effects, that the $d_{x^2-y^2}$ could become stabilized and the occupied orbital. This orbital forms bonds with four neighboring oxygens instead of two. When this is the occupied orbital we expect that there will be four long bonds and two short bonds and the octahedral distortion will be oblate instead of prolate. It also changes the relative *number* of filled and empty orbital pairs at constant charge. A-type antiferromagnetism at 50% doping is then predicted by the G-K rules if we tile the plane alternately with Mn^{3+} and Mn^{4+} ions and the filled $d_{x^2-y^2}$ orbitals of the Mn^{3+} ions lie in the plane. Every site in the plane is then joined by a filled-to-empty orbital pair and therefore ferromagnetic correlations, as illustrated in Fig. 4.5. All the out-of-plane orbitals are empty resulting in AF cor-

relations between the planes. This would seem a natural explanation for the A-type magnetism at 50% doping in the layered manganites. That it is energetically plausible has also been verified theoretically [158, 159], due to the reduced quasi-2D geometry stabilizing the $d_{x^2-y^2}$ orbitals. Note, it has been shown by resonant X-ray scattering [160] that this orbital occupancy explains the A-type antiferromagnetism [161] in $Nd_{0.45}Sr_{0.55}MnO_3$, a 50% doped cubic manganite. What makes the current case particularly interesting is that CE-type charge ordering is observed over a narrow temperature range on cooling, *before* the sample passes into the A-type ground-state. Since the CE style orbital ordering requires $d_{3z^2-r^2}$ occupancy and the A-type requires $d_{x^2-y^2}$ occupancy, this implies a transition in orbital occupancy happening as a function of temperature in this material.

We have carried out local structural measurements using the atomic pair distribution function (PDF) analysis of neutron powder diffraction data on a sample of $La_{2-2x}Sr_{1+2x}Mn_2O_7$ with $x = 0.54$ as a function of temperature to investigate this orbital occupancy transition. The corresponding local structure response from oblate to prolate MnO_6 octahedra transition is evidenced consistently. The PDF technique has proved to be capable of directly measuring the local JT distortion effects in both cubic and layered manganites [127, 162].

4.2.2 Experimental methods

A powdered sample of $La_{0.98}Sr_{2.08}Mn_2O_7$ was synthesized using the method described in Ref. [163]. The samples were characterized using X-ray diffraction and susceptibility measurements. The oxygen content were verified by measuring the $c-$axis parameter that was found to fall on the expected curve for stoichiometric samples.

Neutron powder diffraction measurements were carried out on the Special Environment Powder Diffractometer (SEPD) at the Intense Pulsed Neutron Source (IPNS) at Argonne National Lab (ANL). The sample of about 7.0 g was sealed in a cylin-

drical vanadium can with helium exchange gas. Temperature dependence data were collected from 4 K to room temperature using a closed cycle helium refrigerator.

Experimental PDFs were obtained the program PDFgetN [42]. The resulting total-scattering structure function, $S(Q)$, and the PDF, $G(r)$, from $La_{0.98}Sr_{2.08}Mn_2O_7$ ($x = 0.54$) at 4 K is shown in Fig. 4.6. Superimposed on the PDF is a fit to the data of the average structure model using the profile fitting least-squares regression program, PDFFIT [11]. The $S(Q)$ data were terminated at $Q_{max} = 30$ Å^{-1} before the Fourier transform. This is a reasonable value for Q_{max} in typical PDF measurements on SEPD. Rietveld refinements of the same diffraction data were also carried out using program GSAS [68] with the conventional tetragonal crystallographic cell: space group I4/mmm, $a = b = 3.8666$ Å, $c = 19.8713$ Å, La(Sr)1 (0.00, 0.00, 0.50), La(Sr)2 (0.00, 0.00, 0.32), Mn (0.00, 0.00, 0.10), O1 (0.00, 0.00, 0.00), O2 (0.00, 0.00, 0.19), O3 (0.00, 0.50, 0.09). The type A magnetic phase was added as the second phase to account for the magnetic diffraction peaks. Excellent fits were obtained for data at all temperatures. Fig. 4.7 shows the exemplary Rietveld fit plot of diffraction data at 4 and 300 K.

4.2.3 Results

The PDF, $G(r)$, tells the probability of finding pairs of atoms separated by the real space distance r. Thus every existing inter-atomic distance results in a Gaussian shaped peak, the width of which is determined by the atomic thermal motions [5]. In the case of one e_g electron complete $d_{3z^2-r^2}$ occupancy, a long Mn-O bond around 2.15 Å becomes possible [127] in CE ordering phase. However, there is no direct evidence for a $r = 2.15$ Å peak at any temperature (see Fig. 4.8). Note that Mn-O peak is upside down due to the negative Mn neutron scattering length [5]. The existence of such long bonds has been claimed in earlier PDF measurements at a much lower doping ($x = 0.32$) [162], but are not apparent in our data. In addition, the integrated

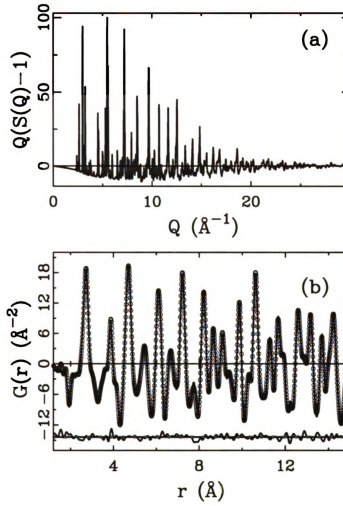

Figure 4.6: (a) Reduced total scattering structure function, $F(Q) = Q(S(Q)-1)$ from $La_{0.98}Sr_{2.08}Mn_2O_7$ at 4 K. (b) The obtained experimental PDF, $G(r)$ (open circles). The solid line is a fit to the data of the crystallographic model with the difference curve shown below offset.

area between 1.6 and 2.1 Å (i.e. the number of short Mn-O bonds) shows no sign of changes over the whole measured temperature range. We attribute the absence of 2.15 Å Mn-O bond to mixed $d_{x^2-y^2}$ (minority) and $d_{3z^2-r^2}$ (majority) orbital occupancies in CE phase. The long Mn-O bonds in both the type A AFM and CE CO phases appear to be shorter than 2.1 Å. This scenario has also been suggested by theoretical calculations [164], as a result of the reduced quasi-2D geometry.

The proposed $d_{x^2-y^2}$ to $d_{3z^2-r^2}$ orbital occupancy transition also changes the shape of MnO_6 octahedra from oblate to prolate. The Mn-O bonds change from four long

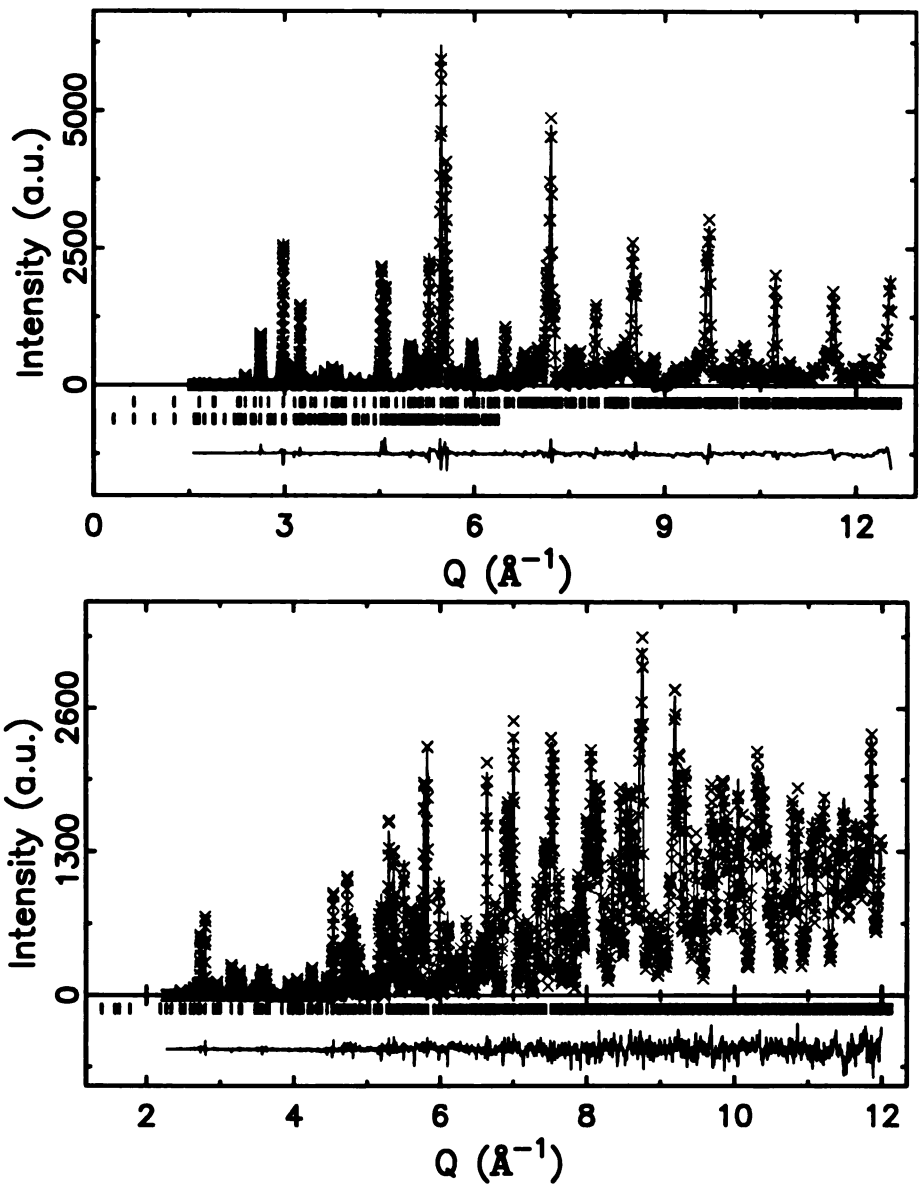

Figure 4.7: Rietveld refinement results of $La_{2-2x}Sr_{1+2x}Mn_2O_7$ at $x = 0.54$ neutron **powder** diffraction data at 4 (upper panel) and 300 K (lower panel). Crosses (×) are **experimental** data, solid lines are the calculated values from refined structure model, **the** difference curve is shown offset below. The short bars indicate the Bragg reflection **positions** from nuclear (upper) and magnetic structures, respectively.

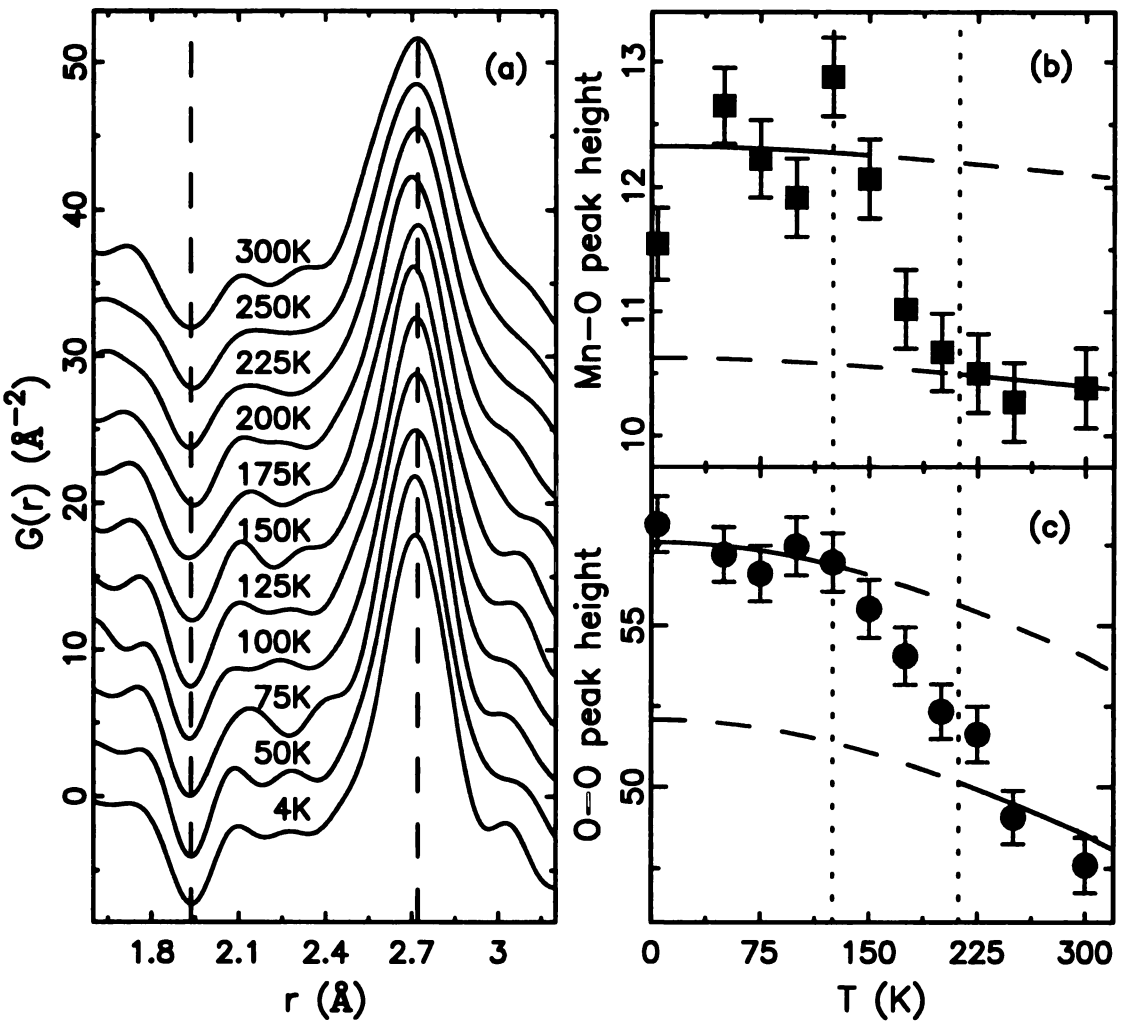

Figure 4.8: (a) The low r region of all experimental $G(r)$s from 4 K to 300 K of $La_{2-2x}Sr_{1+2x}Mn_2O_7$ at $x = 0.54$, with offsets along y axis for clarity. The two dashed lines indicate the Mn-O and O-O peaks at 1.94 and 2.72 Å, respectively. (b) Temperature dependence of the Mn-O absolute peak height around 1.94 Å. Vertical dashed lines indicate the transition temperatures around 110 and 210 K. Debye behaviors of the PDF peak height are indicated by solid lines, with extrapolated dashed lines. (c) The O-O peak height around 2.72 Å. Annotations as in (b).

and two short to two long and four short. Though with the same four and two combinations, the prolate octahedron actually has a broader Mn-O bond length distribution than the oblate, because of the larger separation between the long and short bonds. The underlying reasoning is that one e_g electron will lengthen two Mn-O bonds more than the case of four bonds. A broader distribution directly leads to a broader PDF peak with the area conserved. Therefore, the height of the PDF Mn-O peak, as a directly obtainable experimental quantity, is expected to drop excessively across the oblate to prolate octahedra transition. Fig. 4.8(b) shows the temperature dependence of the Mn-O ($\approx$ 1.94 Å) peak height, with dashed vertical lines indicating the transition temperatures. The PDF peak height normally decreases with temperature due to thermal broadening, following the Debye behavior. One guiding-to-the-eye PDF peak height Debye curve was then calculated and plotted on top of the data in Fig. 4.8(b) with different offsets to match the high and low T data. The required offset between the low and high T behaviors evidences the excess reduction of peak height, as expected from the above reasonings. This trend from the somehow noisy Mn-O peak height data is further substantiated by the peak height temperature dependence of the O-O pairs ($\approx$ 2.72 Å) edging the MnO_6 octahedron. The O-O peak height data shown in Fig. 4.8(c) indicate similar excess peak height falloff, though less sensitive to MnO_6 octahedral distortions. These observations directly support the scenario of the oblate to prolate MnO_6 octahedra transition.

The long Mn-O bonds in the oblate and prolate $Mn^{3+}O_6$ octahedra all lay down in the MnO_2 plane implied by the $d_{x^2-y^2}$ to $d_{3z^2-r^2}$ orbital occupancy transition. However, the orientations of the JT distorted octahedra are in-extractable from the PDF peak height data, which only tell the overall octahedral shape. We then fit the conventional crystallographic model (space group I4/mmm, $a = b = 3.8742$ Å, $c = 19.9844$ Å)) where all MnO_6 octahedra have the same shape with four equal in-plane Mn-O bonds. Though with the presence of local structure disorders, excellent

fits to all experimental PDFs were obtained, suggesting the JT distortions in this bi-layered system are indeed rather small. The the refined thermal displacement parameters (TDP) of the oxygen atoms are examined for signs of disorders. As no symmetry is assumed in PDFFIT, the TDPs are conveniently decomposed into two components, parallel and perpendicular to the Mn-O bond directions. One direct consequence of the oblate to prolate octahedra transition is the increased Mn-O bond length mismatch in the MnO_2 plane (as the long bonds in the prolate octahedra are significantly longer). This effect should show up on the parallel TDP components in Fig. 4.9(a)), where only the in-plane oxygen atom shows anomalous increase across the transition (deviating from the low T Debye behavior at high T). This is a strong indication that the long Mn-O bonds always stay in the MnO_2 plane. Note that the TDP of Mn atoms show no sign of anomaly. To accommodate the long bonds in the prolate octahedra, we also expect the MnO_6 octahedra to increase tilting amplitude. As no octahedral tilting is present in the structure model, sudden increase of the perpendicular TDP components is expected. Fig. 4.9(b) evidences the anomalous increases on both the in-plane and out-of-plane oxygen atoms. These results suggest the oblate to prolate octahedra transition to be the $d_{x^2-y^2}$ to $d_{3z^2-r^2}$ orbital occupancy transition type.

Consistent behaviors are also observed on the lattice constants from the Rietveld analysis of the same data (shown in Fig. 4.9(c,d)). Clearly, the intermediate range between the two transition temperatures appears to be a cross-over region between the low and high T regions, which can be well described with the same Debye model (solid lines) offset-ed differently. The in-plane ($a = b$) and apical (c) constants show similar trends, though with opposite signs. We argue that both behaviors can be qualitatively explained by the $d_{x^2-y^2}$ to $d_{3z^2-r^2}$ orbital occupancy transition as follows. At low T, e_g electrons occupy the $d_{x^2-y^2}$ orbitals. Around 115 K, the orbital occupancy transition to $d_{3z^2-r^2}$ sets in. This process in fact distributes more electron densities along the

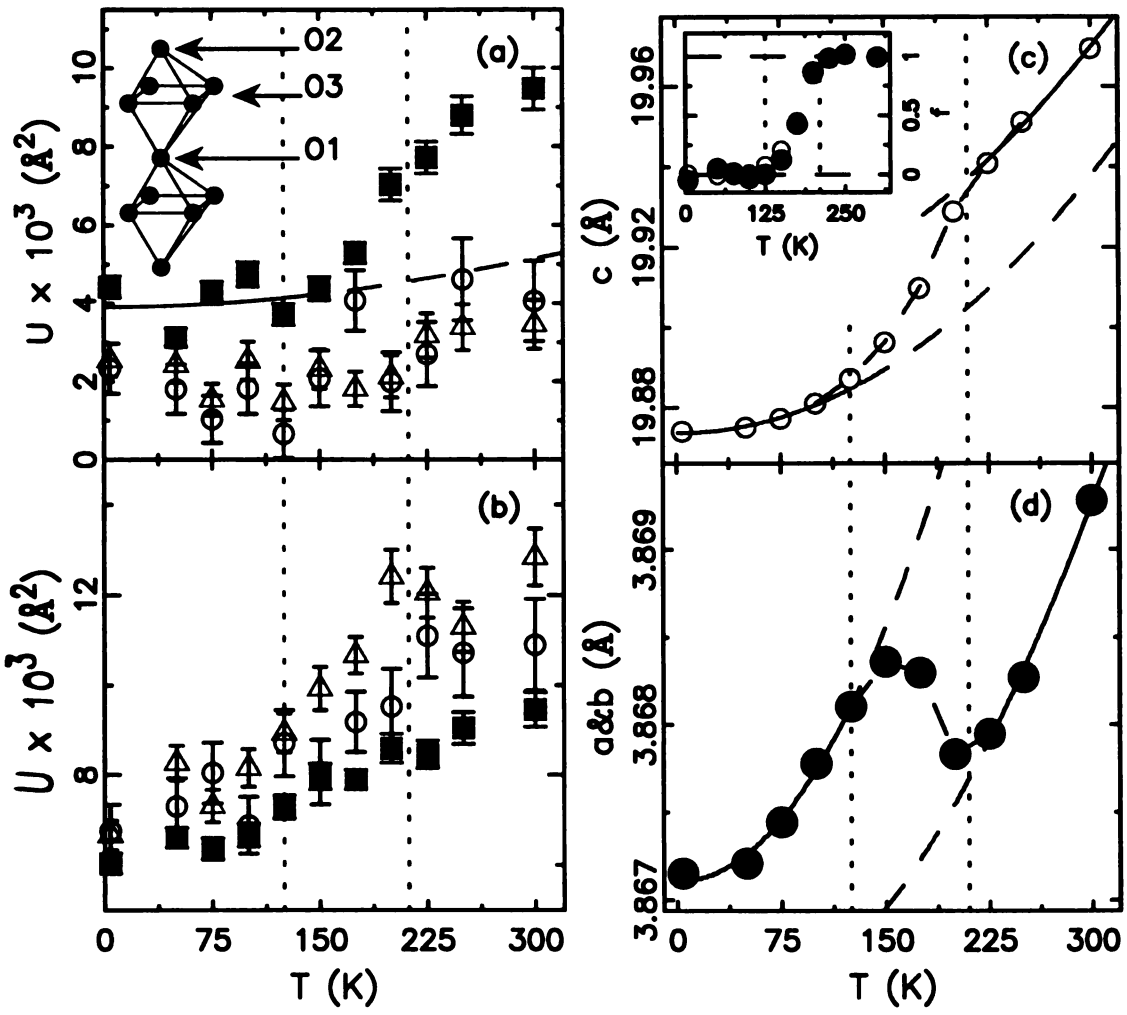

Figure 4.9: Dotted lines in all panels indicate the transition temperature. (a) and (b) **show** the thermal displacement parameters of the O1 (○), O2(△), and O3 (■) oxygen **atoms** along the direction parallel and perpendicular to Mn-O bonds, respectively. (c) **and** (d) show the in-plane *a&b* and apical *c* lattice constant, respectively. The solid **and** dashed lines are the fitted and extrapolated Debye curves, noting that each pair **in** each panel are the *same* curve with different offsets. The inset in (c) shows the "**phase**" fraction of the prolate MnO_6 octahedron as a function of the temperature.

c axis, due to the donut shaped ring in the $d_{3z^2-r^2}$ type orbitals. This will lengthen the c axis. To the opposite, a & b axis would decrease correspondingly, e.g. bond valence and/or volume considerations. The coexistence of $d_{x^2-y^2}$ and $d_{3z^2-r^2}$ orbital occupancy is expected in the cross-over region. Using the extrapolated values (dashed lines) from both the low and high T Debye curves, we then extract the fraction of occupied $d_{3z^2-r^2}$ orbitals by assuming linear combinations. The inset in Fig. 4.9(c) shows thus obtained fraction of the $d_{3z^2-r^2}$ orbital occupancy (type CE phase), noting the good agreements between values calculated from the in-plane and apical lattice constants.

Finally, we show the three crystallographically distinct Mn-O bond lengths from Rietveld refinements within one MnO_6 octahedron in Fig. 4.10(a). The in-plane Mn-O3 distance behaves in the same way as the $a = b$ lattice constants, though not apparent under the shown scale. The significant observation is that the three Mn-O bonds are rather close in length, i.e., the difference is less than 0.04 Å at any temperature. The absence of long Mn-O bonds around 2.15 Å is consistent with our PDF results, supporting the mixed $d_{x^2-y^2}$ and $d_{3z^2-r^2}$ type orbital occupancy picture. As the e_g electron stays always inside the MnO_6 octahedra, the octahedral volume is not expected to show significant anomalies. Fig. 4.10(a) shows both the octahedral and unit cell (scaled) volume increases normally with temperature as expected. Note that drastic octahedral and unit cell volume changes are found near the insulator-metal transitions where the e_g electron mobility changes [165]. The absence of volume anomalies suggest the residence of the e_g electron within the octahedron at all temperatures, and only its orbital occupancy changes.

4.2.4 Discussion and conclusions

Our results are consistent with the widely believed scenario of nano-scale phase separation and competition, by showing the oblate to prolate octahedra transition to be a

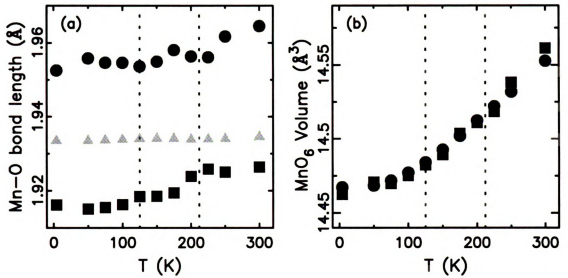

Figure 4.10: (a) Temperature dependence of the three crystallographically distinct Mn-O bond lengths within one MnO_6 octahedron: Mn-O1 (■), Mn-O2 (•), Mn-O3 (△). (b) The MnO_6 octahedral volume (■) and scaled unit cell volume (•). Note that both volumes increase smoothly with temperature, showing no anomalies.

smooth cross-over spanning the phase coexisting temperature range between 115 and 210 K. The structural and magnetic states of the ~50% doped layered manganites have been well characterized by diffraction [155, 149, 153, 154]. There is some disagreement about the details of the transitions (e.g., compare Refs. [153] and [154]); however, qualitatively the progression is as follows. On cooling, charge-order (CO) sets in around 210 K. Below this temperature both A-type antiferromagnetism and CE-type antiferromagnetism appear and coexist in nano-scales over some range of temperature. At low temperature the A-type ferromagnetism prevails and the CE is strongly suppressed or destroyed. High resolution x-ray diffraction [154] suggest that in the coexistence region the sample is phase separated into distinct regions containing the A and CE phases. A hysteresis to the destruction of the CE phase [153] also suggests that this transition is first order. Conductivity goes down at the CO transition. It recovers as the CE phase is destroyed around 115 K bearing a remarkable similarity to the MI transition in the CMR manganites. However, at low temperature the resistivity again rises indicating that the A-type magnetic state is insulating,

albeit with better conductivity than the CE-phase. This behavior reflects a competition between the CE and A phases, and this delicate balance of power between the phases presumably explains the variability in quantitative results between different investigations [153, 154]. We also note that CE-type magnetism is observed in the higher-doped region of the phase diagram [166]. By the same arguments we expect that this requires $d_{3z^2-r^2}$ occupancy. Therefore, if this argument is correct the region of stability of the $d_{x^2-y^2}$ orbital occupancy is rather narrow and bounded on the low- and high- doped side, and at high-temperature, by $d_{3z^2-r^2}$ orbital occupancy.

To conclude, our PDF analysis of high resolution neutron powder diffraction data consistently evidence the oblate to prolate JT distorted MnO_6 octahedra transition when the material goes from type A AFI phase into type CE CO phase. This can also be understood as an unusual charge occupancy transition from $d_{x^2-y^2}$ to $d_{3(x,y)^2-r^2}$ orbitals. Our experimental results provide consistent evidences for theoretical calculations.

4.3 Evidence for nano-scale inhomogeneities in the Mn^{4+} rich region: $0.54 \leq x \leq 0.80$

4.3.1 Introduction to the question

In a wide range $0.46 \leq x \leq 0.66$, the type-A anti-ferromagnetic insulator (AFI) phase is the ground state while it is more commonly found in cubic manganites at the lowest Sr^{2+} dopings, though with some exceptions [167, 161]. Also, a spin disordered "gap" region takes over for doping x from 0.66 to 0.74; then a tetragonal to orthorhombic crystallographic phase transition occurs sharply at x=0.74, followed by the type C/C* AFI phase up to 0.90 doping. There is also a wide charge ordered (CO) region ($0.48 \leq x \leq 0.66$). These observations challenge the simple Goodenough-Kanemori

(GK) rules [81] that successfully correlate the magnetic and structural properties of cubic perovskite manganites and are not well understood.

An A-type AFI phase, of ferromagnetic sheets antiferromagnetically coupled, at 50% doping can be explained within the framework of the GK rules if the Mn $3d_{x^2-y^2}$ orbitals are occupied by the e_g electrons rather than the more commonly observed $3d_{3y^2-r^2}$ occupancy. However, to explain the C/C* AFI phase (linear FM coupled chains that are antiferromagnetically coupled to their neighbors) at high doping requires $3d_{3y^2-r^2}$ occupancy. Because of the symmetry of these different orbitals the former, $3d_{x^2-y^2}$ occupancy, will result in oblate (two short and four long bonds) and the latter, $3d_{3y^2-r^2}$ occupancy, in prolate (two long, four short bonds) JT-distorted octahedra. Alignment of the long-bonds in the plane along the *b*-axis naturally explains the observed orthorhombic symmetry [150]. In addition, a theoretical model based on the two e_g orbitals by Okamoto *et al.* [168] also suggests the stabilization of $3d_{x^2-y^2}$ and $3d_{3y^2-r^2}$ orbitals in type A and type C/C* magnetic phases respectively.

One outstanding question is the origin of the wide spin disordered region ($0.66 \leq x \leq 0.74$). Because of the change in symmetry of the occupied orbitals a transition from A- to C/C*-type order must be first order. Presumably in the spin disordered region a competition exists between these two magnetic orders that frustrates the system preventing magnetic long-range order from forming. It would be interesting to study the local spin correlations to verify this, but lack of single crystals has, thus far, prevented such studies. However, the local structure can be studied straightforwardly using the atomic pair distribution function (PDF) analysis of neutron powder diffraction data [5] and the local magnetism can be inferred from this through application of the GK rules.

In the spin-disordered region the crystallographic structure is metrically tetragonal. This would be observed both if the *local* structure is tetragonal and also if it is locally orthorhombic but the locally orthorhombic domains are disordered along the

a and b directions. For example, this would occur if the long bonds of JT-distorted octahedra are randomly arranged along a and b. The PDF method could distinguish these two cases. Similarly, if Mn^{3+} and Mn^{4+} ions are spatially disordered their presence will be more apparent from a local structural study [23].

We applied Atomic Pair Distribution Function (PDF) analysis of neutron powder diffraction data to search for the presence of JT distorted MnO_6 octahedra in the doping range $0.54 \leq x \leq 0.80$ at low temperature. Being a high resolution local structure probe, PDF technique has proved to be capable of resolving different levels of MnO_6 octahedral JT distortions in cubic perovskite manganites [23]. The advantage of this technique is that both Bragg and diffuse scattering intensities are used, reflecting both long and short range structural correlations. This enables us to study local structures contained in diffuse scattering found underneath and between the Bragg peaks [5].

The results indicate a gradual change of the local structure with doping rather than an abrupt phase transition as seen in the average structure. Local orthorhombicity is evident as early as $x = 0.60$ where the average structure is clearly tetragonal. This supports the idea that the sample is inhomogeneous on the nano-scale with $3d_{x^2/y^2-r^2}$ symmetry JT distorted Mn^{3+} octahedra coexisting with undistorted Mn^{3+} and Mn^{4+} octahedra. The number of JT distorted octahedra varies smoothly with doping.

4.3.2 Experimental methods

Finely powdered samples of $La_{2-2x}Sr_{1+2x}Mn_2O_7$ (x = 0.54, 0.60, 0.64, 0.66, 0.68, 0.70, 0.72, 0.76, 0.78, 0.80) were synthesized at Argonne National Laboratory (ANL). The synthesis method is described elsewhere [163]. All samples were characterized using X-ray diffraction and susceptibility measurements. The oxygen content was verified by measuring the $c-$axis parameter and was found to fall on the expected curve for stoichiometric samples.

Neutron powder diffraction measurements were carried out on the Special Environment Powder Diffractometer (SEPD) at the Intense Pulsed Neutron Source (IPNS) at ANL. The samples of about 7.0 g were sealed in cylindrical vanadium cans with helium exchange gas. Data were collected at 4 K for all the compounds using a closed cycle helium refrigerator. The $x = 0.64$ and $x = 0.68$ samples were measured four months after the others. Standard corrections were made to the raw data to account for experimental effects such as detector dead time and efficiency, background, sample absorption, multiple scattering to obtain the normalized total scattering structure function, $S(Q)$, where Q is the magnitude of the scattering vector. These procedures are described in detail elsewhere [5]. All corrections were carried out using the program PDFgetN [42]. The PDF, $G(r)$, is obtained by a Fourier transformation according to $G(r)$. The PDF gives the probability of finding an atom at a distance r away from another atom. An example of the PDF from $La_{2-2x}Sr_{1+2x}Mn_2O_7$ ($x = 0.80$) at 4 K is shown in Fig. 4.11(b) with the diffraction data in the form of $F(Q) = Q[S(Q) - 1]$ in Fig. 4.11(a). Superimposed on the PDF is a fit to the data of the average structure model using the profile fitting least-squares regression program, PDFFIT [11]. The $S(Q)$ data were terminated at $Q_{max} = 33.0$ Å^{-1}. This is a reasonable value for Q_{max} in typical PDF measurements on SEPD. Uncertainties at the level of σ are drawn as dashed lines on the difference curves.

Peaks in $G(r)$ represent the probability of finding pairs of atoms separated by the distance-r, weighted by the product of the corresponding atom pair's scattering lengths. In a perfect crystalline $La_{2-2x}Sr_{1+2x}Mn_2O_7$ structure, the nearest neighbor distance comes from the 6 equidistant Mn-O bond lengths in one MnO_6 octahedron, corresponding to the first peak in PDF at about 1.94 Å. This is negative due to Mn atom's negative neutron scattering length. Peaks at higher-r generally contain contributions from more than one unresolved pair. The peak at 2.72 Å is dominated by high multiplicity O-O correlations, though it also contains a contribution from

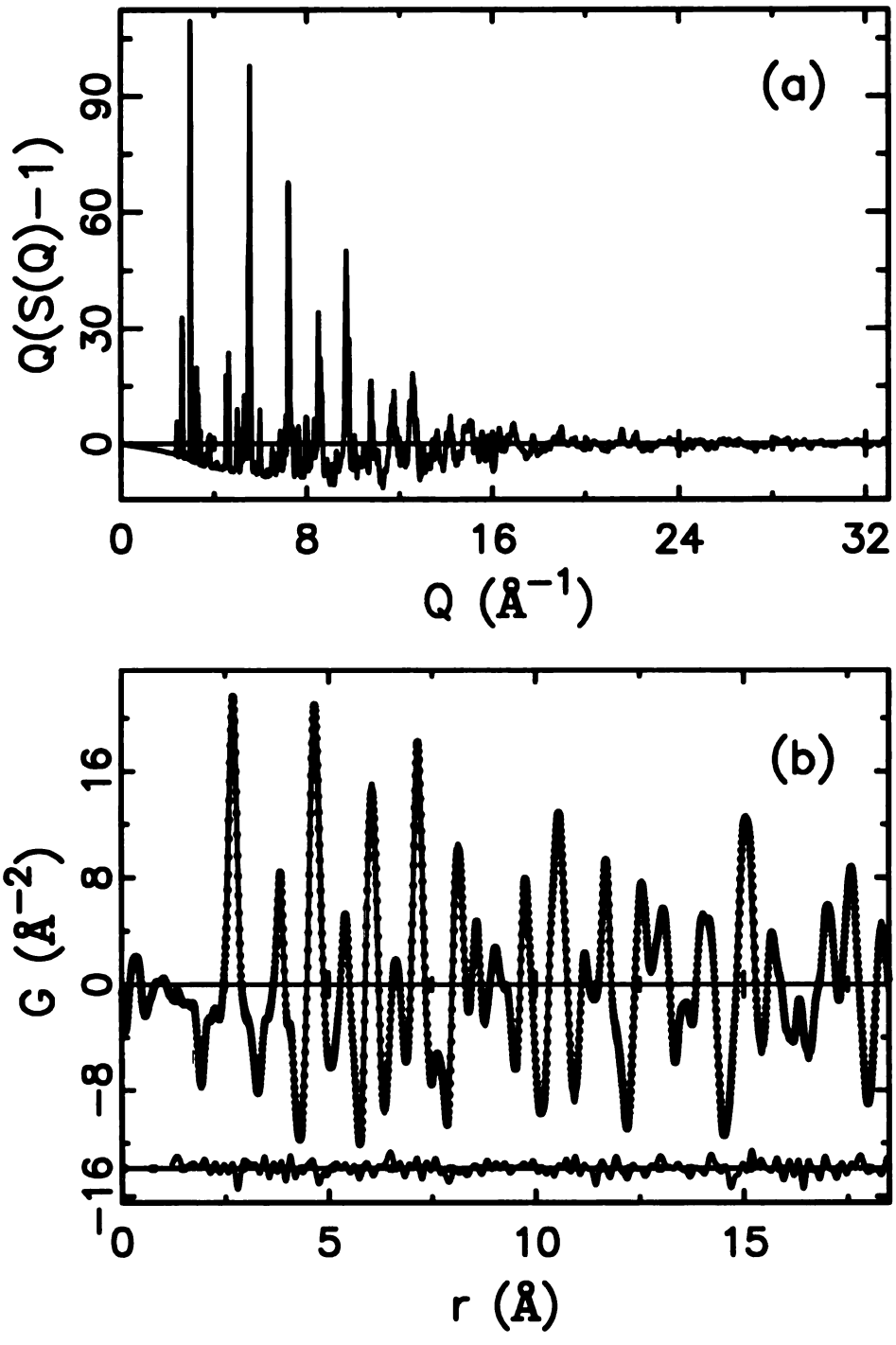

Figure 4.11: (a) The experimental reduced structure function $F(Q) = Q*(S(Q)-1)$ of $La_{2-2x}Sr_{1+2x}Mn_2O_7$ at x =0.80. (b) The experimental $G(r)$ obtained by Fourier transforming the data in (a) (solid dots) and the calculated PDF from refined structural model (solid line). The difference curve is shown offset below.

La/Sr-O correlations. The decomposition of multiple contributions is handled by a real space Rietveld refinement program: PDFFIT [11] with which a structural model can be obtained without the constraints posed by space group symmetries. Therefore, both local structural and average structure analysis can be performed on the same data set.

4.3.3 Model independent analysis

Low-r PDF peaks directly reflect the local structural details, and disorder in the local structure can cause excess peak broadening [23], extra shoulders [162] and even split peaks [127]. The prolate JT distorted octahedra of Mn^{3+} ions result in four short Mn-O bonds in the range 1.92–1.97 Å and two long bonds at 2.16 Å [169, 126, 127]. In the cubic manganites, in the absence of disorder, these are easily resolved in the PDF [127]. With doping the loss of orientational order of the orbitals quickly suppresses the coherent JT distortion and the average structure changes from orthorhombic to rhombohedral. However, the presence of fully JT distorted octahedra is evident in the local structure, though the peak in the PDF from the long-bonds is not resolved and is evident only as a broad shoulder [23, 170, 171].

We first investigated the PDFs from these layered, doped, manganites to search for qualitative evidence for the existence of long $r = 2.16$ Å bonds. This is shown in Figures 4.12 and 4.13. Fig. 4.12 shows the experimental PDFs at x =0.54 and 0.60 with a calculated PDF from a model assuming all $Mn^{3+}O_6$ octahedra are prolate. In this case the number of Mn^{3+} octahedra is determined from the doping and of these, two out of six Mn-O bonds are set to 2.16 Å. The clear discrepancies between experiments and model rule out the existence of fully JT distorted prolate MnO_6 octahedra in the type A AFI phase. As we discuss elsewhere, this is probably due to the fact that electrons are largely delocalized in the planes (though not perpendicular to them) in this region of the phase diagram at low-T [172], in analogy with the

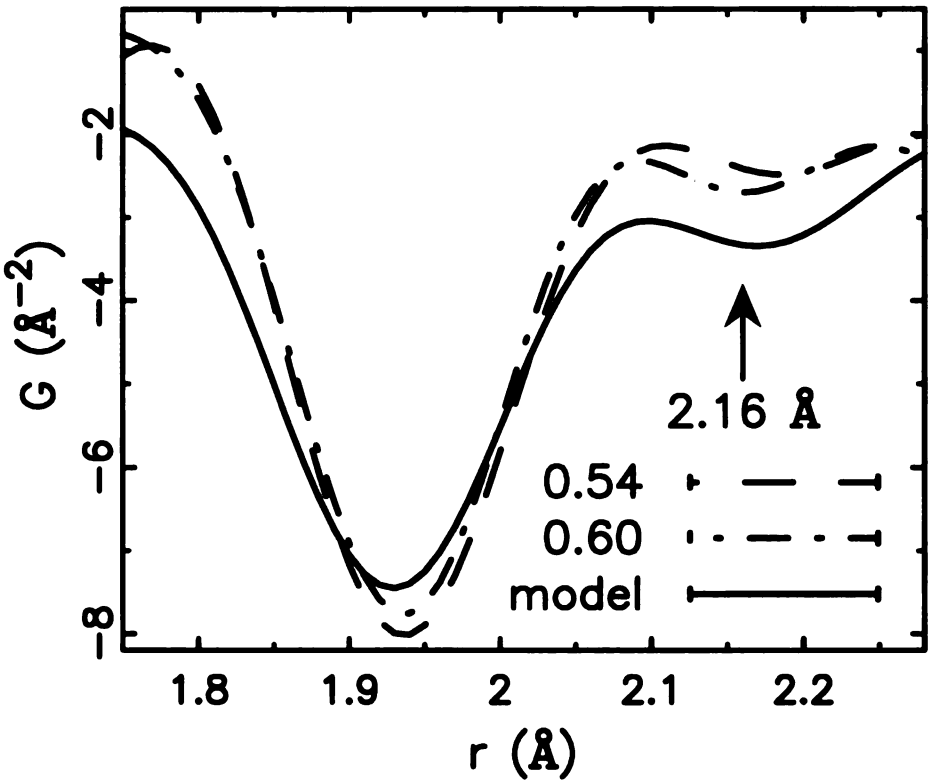

Figure 4.12: Two dashed lines show the experimental PDFs of doping x at 0.54 and 0.60. While the model PDF shown as the solid line is calculated assuming 46% prolate octahedra (two long Mn-O bonds at 2.16 Å, four short ones at 1.935 Å) mixed with 54% normal octahedra (6 Mn-O bonds at 1.935 Å).

situation in the CMR region of the cubic manganites [23, 170, 171].

In the type C/C* orthorhombic phase, we expect e_g electrons to stay in $3d_{3y^2-r^2}$ orbitals, and therefore the 2.16 Å long bonds are expect to be present. In this case the number of Mn^{3+} sites, and therefore the number of long-bonds, is rather small. Nonetheless, there is rather good agreement between the prediction of the simple model and the data in the region around $r = 2.16$ Å. Figure 4.13 shows the experimental PDFs at $x = 0.78$ and 0.80 with the model-PDF. Because of the small number of long bonds (6.7% at $x = 0.8$) this result is not conclusive evidence supporting the existence of these long bonds, though the data are consistent with their presence.

The PDF peaks represent the bond length *distributions* in the material. The

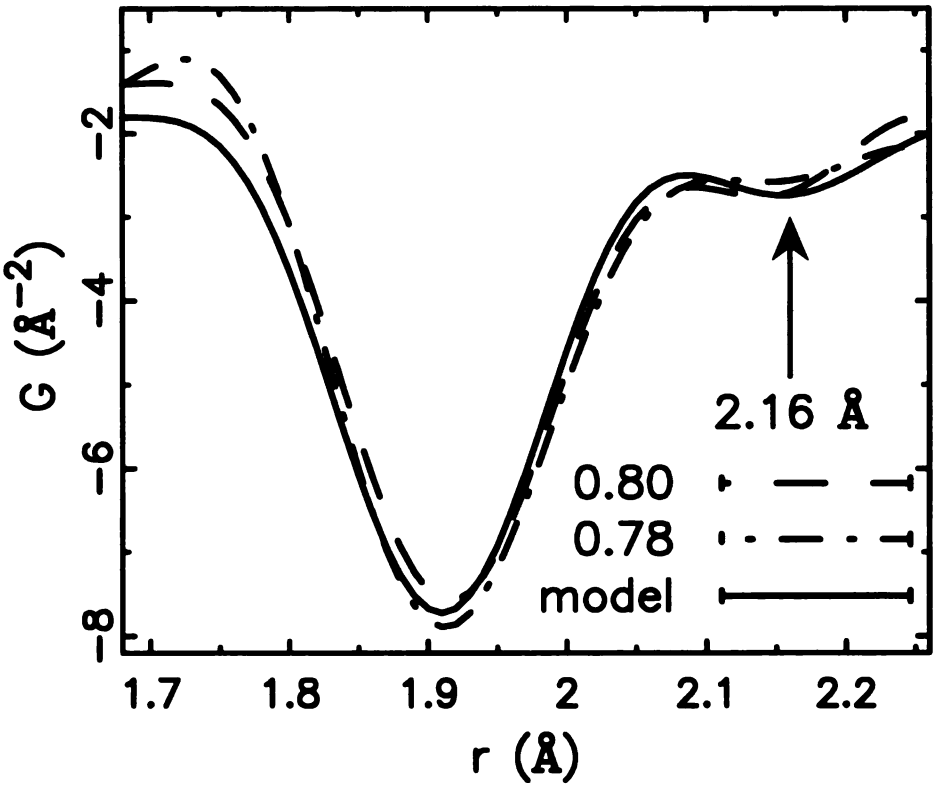

Figure 4.13: Two dashed lines show the experimental PDFs of doping x at 0.78 and 0.80. While the model PDF shown as solid line is calculated assuming 20% prolate octahedra (2 long Mn-O bonds at 2.16 Å, 4 short ones at 1.935 Å) mixed with 80% normal octahedra (6 Mn-O bonds at 1.935 Å).

proposed MnO_6 octahedral shape change of the Mn^{3+} octahedra, from normal to prolate JT distorted with increasing doping, induces more local structural distortion and thus would cause the low-r PDF peak to broaden. An increase in disorder in the local structure will result in this peak broadening, and therefore lowering, with doping as observed. In Fig. 4.14 we show the change of the peak height, inversely related to the peak width, of the first PDF peak around 1.935 Å with doping. The $x = 0.64$ and 0.68 samples lie above the others. These samples were measured at a later date and evidently the systematic errors have not been perfectly reproduced. Note that the data were all collected at 4 K so no temperature broadening effects are expected. Also, increasing the doping in this highly doped region moves the composition towards the pure stoichiometric end-member and so dopant ion induced disorder coming from

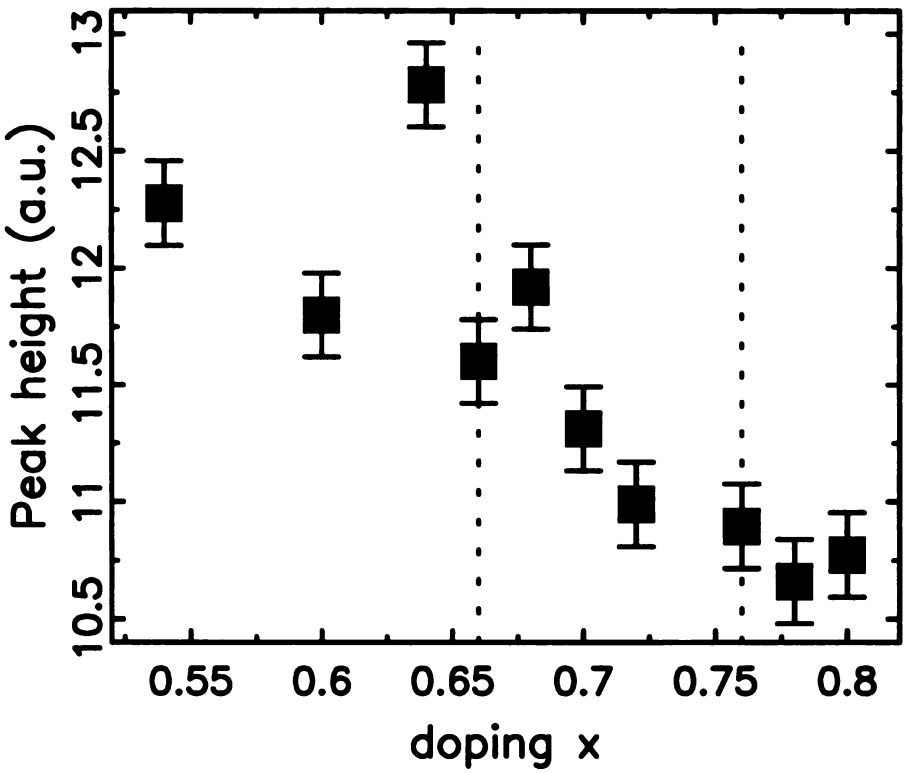

Figure 4.14: Solid squares show the magnitudes of the heights of the first Mn-O peak around 1.94 Å. The vertical dotted lines indicate positions of magnetic phase transitions from type-A to spin disordered to type C/C*.

the alloying is decreasing with increasing doping. The observation of an increase in disorder with increasing doping, in this peak that is highly sensitive to the Mn-O bonds, is therefore strong evidence that an electronically driven change is occurring in the Mn-O octahedral shape.

The smooth evolution of the peak heights (Fig. 4.14) suggests that the local structural changes occur continuously with changes of doping concentration x, in contrast to what is observed in the average structure. The change in global symmetry from tetragonal to orthorhombic at $x = 0.76$ is presumably related to a transition of the JT long-bonds from being randomly oriented to having a net orientation along b.

4.3.4 Structural modeling

Structural modeling gives a more quantitative picture of the local structure than the qualitative analysis described above. Two structural models were fit based on the tetragonal and orthorhombic crystallographic models [150]. It is worth noting here that any constraint by the space group and symmetry during average structure analysis can be relaxed in our real space full profile modeling. Additionally, we can add any kind of constraints based on physical reasons. It was found that the best agreement was found for doping $x \geq 0.60$ when the tetragonal symmetry is relaxed to orthorhombic. In the case of $x = 0.60$ the improvement in fit of the orthorhombic model is barely significant and in this case we cannot unambiguously assign the local symmetry as orthorhombic. In the following, only results from the relaxed orthorhombic symmetry are reported.

The two in-plane lattice constants a and b are shown in Fig. 4.15 together with the lattice constants obtained from Rietveld refinement using GSAS [68]. The two dashed vertical lines show the phase transition from type-A AFI to spin disordered and tetragonal to orthorhombic (which is almost coincident with the magnetic transition from spin disordered to type C/C* AFI), respectively. The PDF refinements suggest the structure is already locally orthorhombic as early as $x = 0.60$, while the sharp crystallographic phase transition occurs around $x = 0.76$. This could be explained if JT distorted MnO_6 octahedra are beginning to appear on Mn^{3+} sites around $x = 0.60$, but the long bonds lie along the a and b axes randomly.

It is important to determine whether the JT long-bonds that appear at $x \geq 0.60$ lie in the plane, perpendicular to the plane, or are distributed between these possibilities. This can be studied by looking at the refined values of the Mn-O bond lengths. The four different Mn-O bond lengths within one MnO_6 octahedron, determined by PDFFIT, are shown in Fig. 4.16. What is clear from this Figure is that over this doping range there is no clear trend in the apical (perpendicular) bonds. This

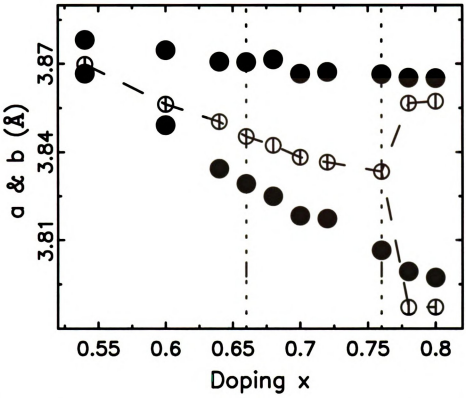

Figure 4.15: Solid circles are the in-plane lattice constants a and b from PDF refinements with orthorhombic models, while open circles are from Rietveld refinements on the same data with tetragonal and orthorhombic models in $0.54 \leq x \leq 0.76$ and $0.78 \leq x \leq 0.80$, respectively. Vertical dotted lines indicate positions of magnetic phase transitions from type-A to spin disordered to type C/C*.

implies that the observed increase in the Mn-O bond-length distribution with doping is coming primarily from the in-plane bonds. The JT distorted Mn^{3+} ions that appear with doping are predominantly locating their long-bonds in the plane. The electronic states along c remain largely unchanged with doping, and little or no charge transfer occurs between in-plane and out of plane.

We have observed evidence for JT long bonds lying in the plane from the PDF refinements. If this picture is correct we would expect to see a response in the refined in-plane Mn and O displacement factors. These should be small for $x < 0.60$ because there is little disorder in the structure and the models that we are using, based on the average structure, should work well also for the local structure. We might expect them also to be small and largely thermal in origin for $x > 0.76$ where the JT distorted

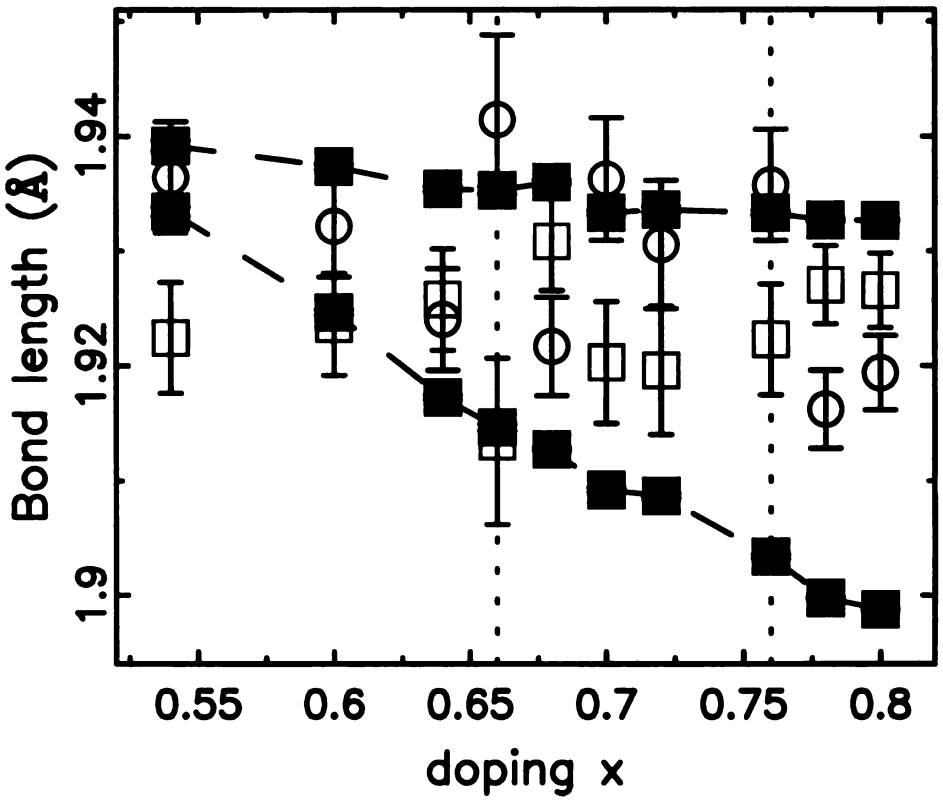

Figure 4.16: Solid squares are the two in-plane (ab) Mn-O bond lengths. The bond length between Mn and the out of plane O atom is shown as open squares, while the bond length between Mn and the intra plane O atoms is shown as open circle. Vertical dotted lines indicate positions of magnetic phase transitions from type-A to spin disordered to type C/C*.

orbitals are ordered along the b axis. In the spin disordered region we see evidence in the local structure for significant numbers of JT distorted Mn^{3+} ions that are not fully ordered. By allowing the local structure to be orthorhombic much of this disorder will not show up in PDF derived displacement factors. However, it is interesting to note that there is a peak in the value of the planar Mn-O displacement parameters in this region, as shown in Fig. 4.17.

4.3.5 Discussion

In the earlier section, we present the evidence supporting the fact that, at low temperature at $x = 0.54$, the e_g electrons associated with Mn^{3+} ions may be delocalized

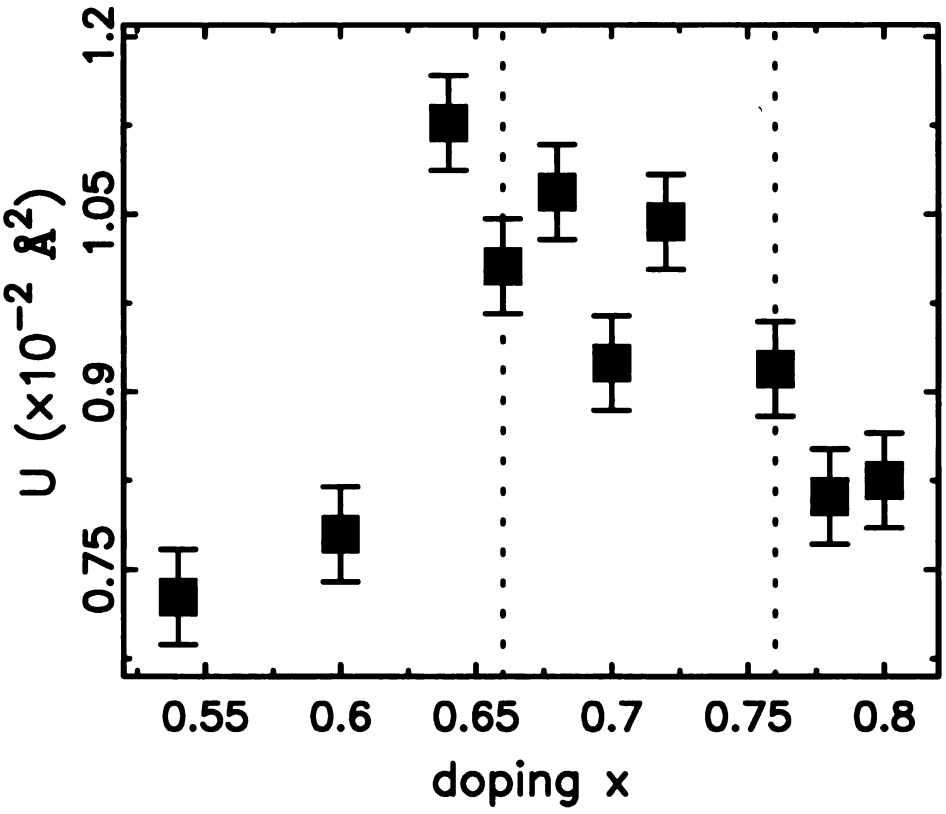

Figure 4.17: Thermal displacement factor of the in-plane O atoms along the direction of Mn-O bonds. Vertical dotted lines indicate positions of magnetic phase transitions from type-A to spin disordered to type C/C*.

in the plane. At this point there are no JT distorted MnO_6 octahedra and the local structure agrees with the average structure. When the C/C*-type antiferromagnetism appears around $x = 0.76$, coincident with a global orthorhombic distortion, it seems clear that JT distorted MnO_6 octahedra have appeared with the $3d_{3y^2-r^2}$ orbitals occupied. The main result from the current work is the observation that, in the local structure, the crossover between these two behaviors happens continuously with doping and is not abrupt as it is in the average structure. The structure is locally orthorhombic as early as $x = 0.60$ suggesting the presence of JT distorted MnO_6 octahedra that are orientationally disordered within the plane. From this work we cannot tell if this disorder is static or dynamic.

This picture could qualitatively explain the spin-disordered region since, from the GK rules, local magnetic correlations will randomly fluctuate between ferromagnetic

and antiferromagnetic from site to site.

More detailed consideration of this model suggests that the sample is likely to be nano-phase segregated in this region since we believe the low-doping end-member (the $x = 0.54$ sample) has its e_g electrons delocalized in the plane [173]. For this to make sense, delocalized clusters with locally A-type magnetic correlations must persist in this spin disordered region. Since there is no evidence of macroscopic phase-separation these clusters are likely to be nano-scale. Presumably they coexist with nanoscale regions of the sample where the e_g electrons are localized as Mn^{3+} ions with a local JT distortion. With increasing doping the number of these localized Mn^{3+} sites first increases as the proportion of the sample in the localized state increases at the expense of the delocalized state. Once the entire sample has transformed to the localized state, with increasing doping the number of Mn^{3+} sites will decrease as $(1-x)$ in the normal way. This is apparent from the decreasing orthorhombicity that is evident for $x > 0.80$ [150].

4.3.6 Conclusions

Based on PDF results, we suggest that the local structure of $La_{2-2x}Sr_{1+2x}Mn_2O_7$ evolves smoothly as a function of doping at low temperature in the region of the phase diagram $0.54 \leq x \leq 0.80$. The material evolves smoothly from being locally tetragonal at $x = 0.54$ to having a well established orthorhombicity at $x = 0.80$. The local and global structures agree well at these end-points. However, in between, and associated with the spin disordered region of the phase diagram, the local structure appears orthorhombic even though the material is metrically tetragonal. These results can be reconciled if JT distorted MnO_6 octahedra exist with their long-bonds lying in the plane but disordered along the a and b axes. We have discussed that these results are consistent with the presence of inhomogeneities resulting in a coexistence of delocalized and localized electronic states, possibly due to nano-scale phase

separation, in this intermediate region of the phase diagram, into regions that have the characteristics of the two end-members at $x = 0.54$ and $x = 0.80$ respectively. We have argued that such a nano phase separation into disordered and possibly fluctuating A-type and C/C*-type magnetic domains may explain the frustrated magnetism in this region. Making certain assumptions we have quantified the evolution of the phase separation with doping.

Chapter 5

Applications of the RA-PDF Method

5.1 Prelude

In chapter 2, we described in great detail the recent development of the RA-PDF method. Some exemplary data were also shown to justify the high reliability and quality of RA-PDF data analysis. As the underlying drive is to apply it to answer significant scientific questions, several recent applications will be shown in this chapter.

5.2 Locally distorted Ti square nets in Ti_2Sb

5.2.1 Introduction to the question

The new binary antimonide Ti_2Sb was discovered in Prof. Kleinke group [174] during attempts to further verify the usefulness of the recently published Kleinke-Harbrecht structure map of the M_2Q pnictides and chalcogenides [175]. This structure map was previously utilized to correctly predict the hitherto uncovered arsenides ZrTiAs and ZrVAs that exhibit undistorted Ti and V square nets, respectively [176, 177]. The

Ti_2Sb sample synthesis procedures is described elsewhere [174].

The crystal structure has been solved through conventional crystallographic analysis with both X-ray powder diffraction and single crystal diffraction refinements. Starting with a tetragonal unit cell (space group $I4/mm$, $a = b = 3.95$ Å, $c = 14.61$ Å, asymmetric unit: Ti1 (0.0, 0.0, 0.33), Ti2 (0.0, 0.5, 0.0), and Sb (0.0, 0.0, 0.14)), both diffraction data were fitted reasonably well. Fig. 5.1 shows the ball and stick model of Ti_2Sb crystal structure. However, the thermal displacement factor U_{11} (0.125) for the Ti2 atom is anomalously large compared to U_{22} (0.006) and U_{33} (0.003) (all U values given in Å^2). All other atoms show neither strong anisotropy nor abnormal U values. Fig. 5.2 shows the thermal ellipsoid of the Ti2 square nets. As such U_{11} anomaly is usually a good indication of static disorder along the anomalous direction, a distorted model with split Ti2 sites was then introduced. In this model, Ti2 atoms are shifted along the U_{11} direction in the asymmetric cell to have none zero x values, but with 50% occupancy to maintain the sample stoichiometry. Refinement with this distorted model improved the agreement significantly, resulting the Ti2 x value of 0.0701(6). Due to the absence of super-lattice peaks, increase of the unit cell was not considered at the first place. Two samples with different synthesis conditions were studied and gave the same distortion of the Ti2 atoms.

This simple distorted model with split Ti2 sites needs to be carefully examined. First, the introduced split Ti2 sites resulted in a unphysical Ti2-Ti2 bond length of 0.56 Å. This can be resolved if the two split sites originating from the same Ti2 site can not be occupied at the same time, though both with 50% occupancy. One hypothetical superstructure of the Ti2 net (shown in Fig. 5.3) was proposed, but can not be fully justified without the observation of super-lattice reflections. While the Ti2 square net distortion is nevertheless strongly suggested, the Ti_2Sb structure appears to be a case of local distortions without long range ordering. If the Ti2 splitted sites scenario correctly describes the local structure, some specific set of local inter-atomic

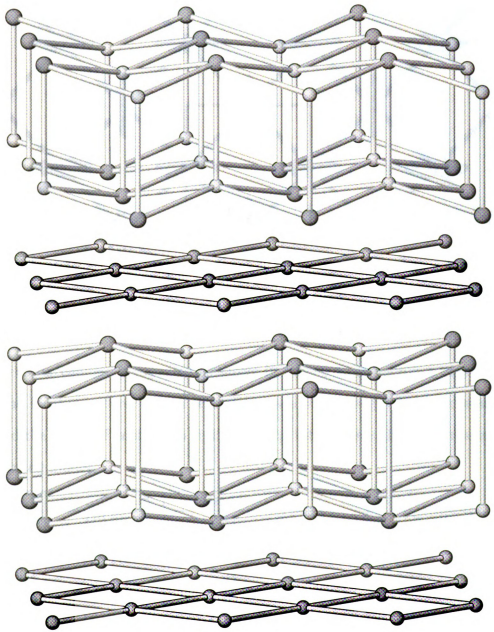

Figure 5.1: Crystal structure of Ti_2Sb in ball and stick model. The connected Ti2 square nets lie at the bottom and in the middle.

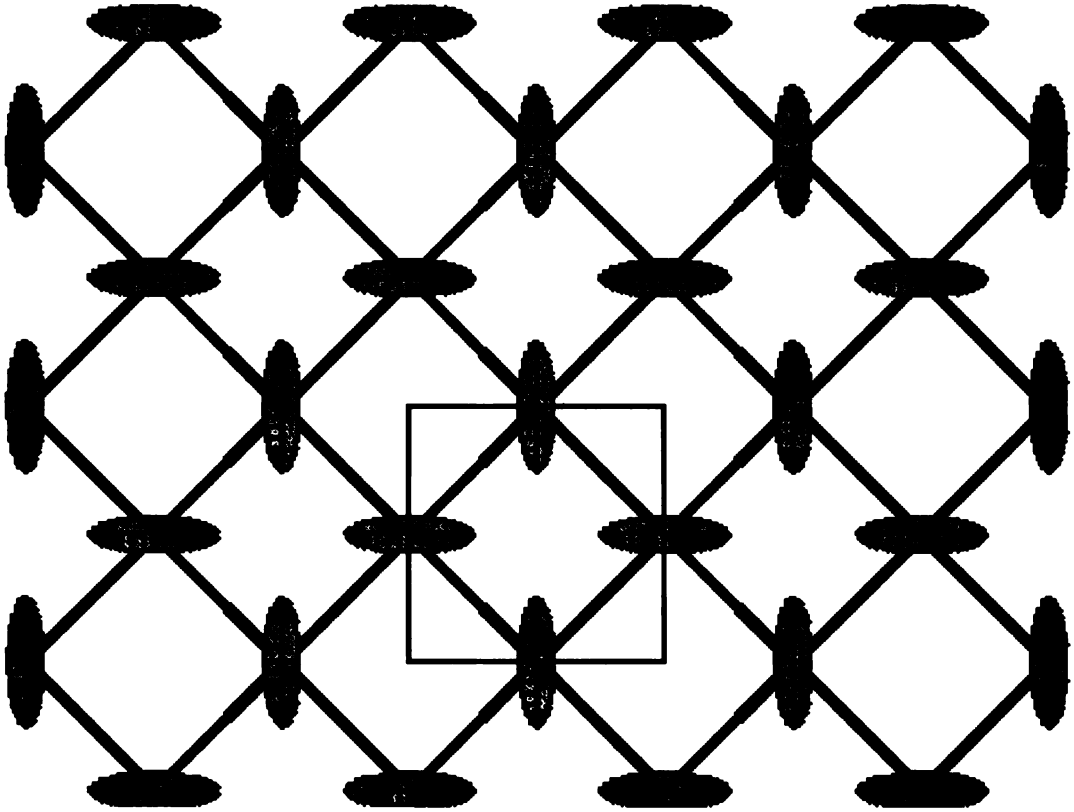

Figure 5.2: Planar net of Ti2 atoms in Ti_2Sb, with thermal ellipsoids shown.

distance splits/changes is expected as shown in table 5.1. To establish beyond doubt about the local structure, a high resolution local structure probe is necessary. We employed the RA-PDF method to verify the local inter-atomic distances coming from the distorted model.

	atomic pair	**undistorted**	**distorted**
1	Ti2-Sb	2.84	2.86
2	Ti2-Sb	4.87	4.65 and 5.10
3	Ti2-Ti2	2.80	2.82
4	Ti2-Ti2	3.95	3.40 and 4.51
5	Ti2-Ti2	5.59	3.99, 5.22, 5.59, and 6.09
6	Ti2-Ti1	3.17	3.00 and 3.35
7	Ti2-Ti1	5.07	4.97 and 5.18

Table 5.1: List of expected inter-atomic distance splits/changes from the undistorted to distorted model. All lengths are given in unit of Å.

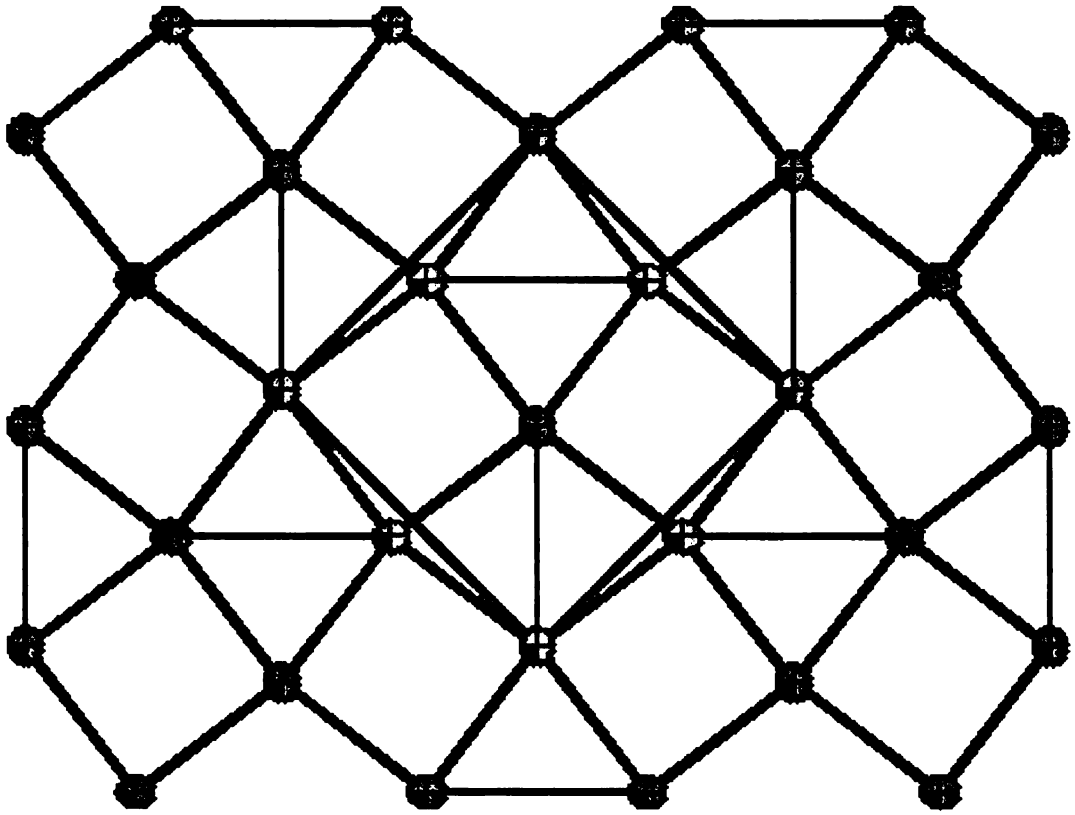

Figure 5.3: The hypothetical $\sqrt{2} \times \sqrt{2} \times 1$ superstructure of the Ti2 square nets.

5.2.2 RA-PDF analysis of local Ti2 distortions

The distorted model with split Ti2 sites ultimately yields different inter-atomic distances, in particular involving Ti-Ti bonds (Table 5.1), but also Ti-Sb distances in the second coordination sphere. Experimental proof for the presence of the bonds/distances stemming from the split of Ti2 sites was directly obtained utilizing the real-space pair distribution function (PDF) technique [5]. The PDF, $G(r)$, gives the probability of finding pairs of atoms separated by distance r, and thereby comprises peaks corresponding to all discrete inter-atomic distances. The experimental PDF is a direct Fourier transform of the total scattering structure function $S(Q)$, the corrected, normalized intensity, from powder scattering data given by $G(r) = \frac{2}{\pi} \int_0^\infty Q[S(Q) - 1] \sin Qr \, dQ$, where Q is the magnitude of the scattering vector. Unlike crystallographic techniques, the PDF incorporates both Bragg and diffuse scattering intensities resulting in local structural information [5]. Its high real-space resolution is

ensured by measurement of scattering intensities over an extended Q range (35.0 Å^{-1}) using short wavelength X-rays or neutrons.

Both X-ray and neutron powder diffraction experiments were carried out. These give complementary data-sets due to the different relative scattering lengths of Ti and Sb to X-rays and neutrons: $f_{Ti}(0)/f_{Sb}(0) = 0.43$ for X-rays whereas for neutrons $b_{Ti}(0)/b_{Sb}(0) = -0.61$. Thus, the scattering from Ti, and therefore the PDF peaks originating from Ti correlations, are somewhat more apparent in the neutron data. The X-ray experiment was performed at the 6-ID beam line at the Advanced Photon Source (APS) at Argonne National Laboratory. A powdered Ti_2Sb sample of disk shape (thickness of 1.0 mm, diameter of 1.0 cm) was loaded into a hollow flat metal plate, and then sealed between thin kapton films. Data acquisition at 300 K employed the recently developed rapid acquisition PDF (RA-PDF) technique [61] with the X-ray energy of 98.0 keV. A single exposure of the image plate detector was limited to 2 seconds to avoid detector saturation, and was repeated 20 times to achieve better counting statistics in the high-Q region.

The neutron experiment was performed at the newly upgraded neutron powder diffractometer (NPDF) at the Lujan center at Los Alamos National Laboratory [21]. A powdered Ti_2Sb sample of 5.92 g was loaded into a standard 3/8" vanadium can under helium exchange gas. The sample height was measured to be 2.92 cm. Low temperature is preferred to sharpen the peaks in the PDF and so data acquisition was carried out at 15 K in a displex closed cycle refrigerator. Data were collected for 10.0 hours. The long collection time was necessitated because the large amount of incoherent scattering from this sample. Calibration measurements of the background, empty containers, etc, were also performed. Standard corrections were applied to obtain the total scattering structure functions, $S(Q)$, using the programs PDFgetX2 [41] and PDFgetN [42] for X-ray and neutron data, respectively. The experimental reduced structure function, $F(Q) = Q(S(Q) - 1)$, is shown in Fig. 5.4 (a) (X-ray) and (b)

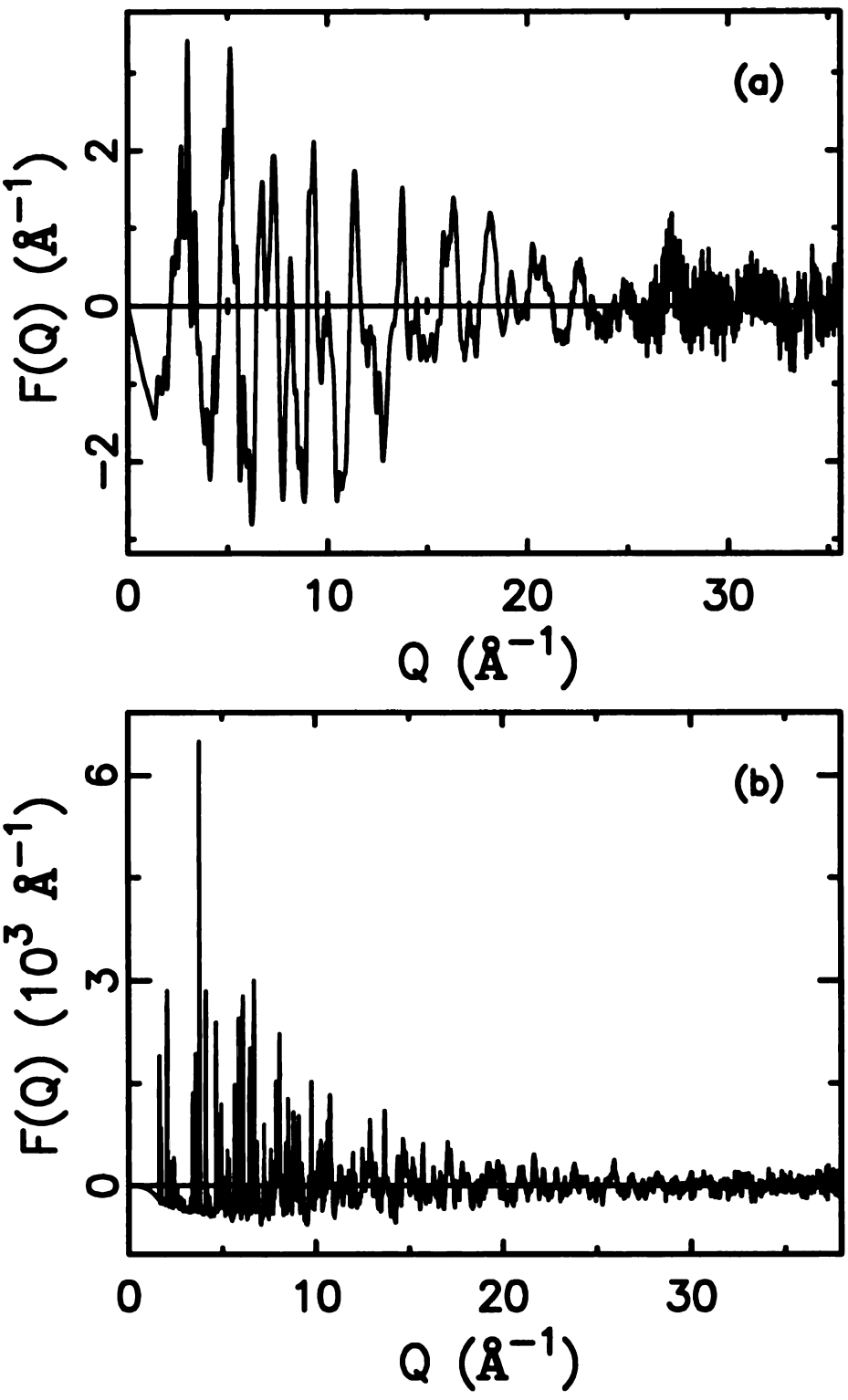

Figure 5.4: The experimental reduced structure function $F(Q) = Q(S(Q) - 1)$ of Ti_2Sb (a) at room temperature from the X-ray measurement and (b) at 15 K from the neutron data.

(neutron). The resulting PDFs, $G(r)$, are shown in Fig. 5.6 as the solid dots. Panels (a) and (b) show the X-ray data and (c) and (d) have the neutron data.

The data-PDFs were examined to search for direct evidence of the short and long Ti2-Ti2 distances implicit in the distorted model. A large thermal factor with no underlying splitting results in broad peaks in the PDF centered on the average position whereas a split position results in peaks in the PDF splitting into two components that retain their sharpness. Thus, the distorted and undistorted models should be directly distinguishable in the PDF. The low-r region of the PDF is shown in Fig. 5.5 for X-rays (upper curve) and neutrons (lower curve). Features in the PDF can be compared to expected bond distances from Table 5.1. The strength of the PDF peak depends on the scattering power of the two atoms contributing to the peak, and the multiplicity of the pair. For both X-rays and neutrons Ti is a weaker scatterer than Sb and so the low multiplicity Ti-Ti bonds that would show the distortion directly are hard to see. In particular, the Ti1-Ti2 peak centered at 3.17 Å and the Ti2-Ti2 distance at 3.95 Å are barely evident. There is some suggestion from the neutron data that the 3.17 Å is split (apparent as a highlighted "M"-shaped feature in both the x-ray and neutron difference curves), but by itself this is hardly convincing. However, the relatively strong Ti2-Sb peak centered at 4.87 Å gives a clear and unequivocal indication of this splitting. The peak from the undistorted model centered at this distance is absent in the data which, instead, has relatively sharp features at 4.65 Å and 5.10 Å. This results in a clear feature in the difference curves below the data in Fig. 5.5. In the X-ray data it is M-shaped and in the neutron data W-shaped; the difference due to the change in sign of the Ti-Sb peak in the PDF due to the negative neutron scattering length of Ti. These M/W features clearly show that the peak centered at 4.87 Å has split into a shorter and a longer peak.

The data were then modeled quantitatively using a real-space profile fitting program, PDFFIT [11]. This program can refine the crystallographic model to the data,

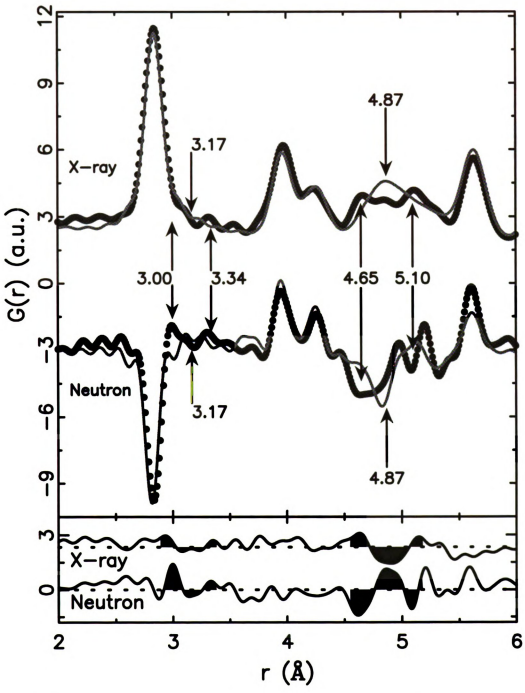

Figure 5.5: Experimental PDF (solid dots) and the calculated PDF from the distorted model (solid line). Upper curves: X-ray data; lower curves: neutron data. The difference curves based on the undistorted model are shown below.

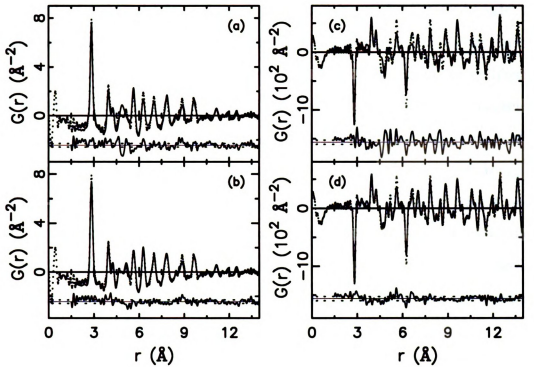

Figure 5.6: PDFs, G(r), from the data shown in Figure 5.4 (a), (b): X-ray data; (c), (d): neutron data (shown as the blue dots in both cases). Solid lines are the fits to the model data, with (a) and (c) from the undistorted model and (b) and (d) from the split site model. Difference curves are shown below the data. The dotted lines around the difference curves indicate the standard uncertainties due to random counting statistics on the data at the 1 σ level.

in analogy with Rietveld refinement. However, local structural distortions can be introduced into the models even when they are not long-range ordered and no crystallographic super-lattice reflections are observed as in the current case. We first fitted the data with the undistorted model, and show the results in Fig. 5.6 (a) (X-ray) and (b) (neutron). Clearly, the undistorted model proves to be insufficient, as evident from the difference curves below the data. Fluctuations significantly larger than the experimental uncertainties (the estimated errors at the 1 σ level are shown as dotted lines associated with the difference curves) are observed over the whole fitting range. One of the strengths of the PDF technique is that it yields quantitatively reliable intermediate range information on nanometer length-scales. The persistence of the fluctuations in the difference curve of Fig. 5.6 (c) is significant and a clear indication

that the undistorted model fit to the data is lacking. Next, the distorted model with split Ti2 sites was tried, with the fitting results shown in Fig. 5.6 (c) (X-ray) and (d) (neutron). The agreements to both X-ray and neutron PDFs improved significantly over the entire range, with the addition of only one additional refinement parameter, and gave rather satisfactory fits given that the distorted model is an average of the unknown superstructure. The superstructure model, in the Cmca space group, was also tried and gave comparable fits. The structure data from the PDF refined models are in excellent agreement with those refined from the single crystal study as shown in Table 5.2. The full profile PDF refinements confirm that the distorted model describes both the local and average structure to great accuracy and is far superior to the undistorted model. The superstructure model in the Cmca space-group gives comparable agreement to the split site model which shows that this model is also consistent with the data as well as making better physical sense.

	Crystal data	**X-ray 300K**	**Neutron 15K**	**Neutron 300K**
a (Å)	3.9546(8)	3.9611(10)	3.9472(2)	3.9575(3)
c (Å)	14.611(3)	14.655(6)	14.565(1)	14.576(2)
Ti1 z	0.3305(1)	0.3307(3)	0.33069(8)	0.3310(1)
Ti2 x	0.0701(6)	0.0708(20)	0.0711(9)	0.067(1)
Sb z	0.1398(1)	0.1398(1)	0.13977(6)	0.1400(1)
Ti1 U_{iso}	0.0074(4)	0.0073(2)	0.00273(5)	0.0062(1)
Ti2 U_{iso}	0.0067(2)	0.0069(2)	0.00359(6)	0.0079(1)
Sb U_{iso}	0.0063(2)	0.0035(1)	0.00242(3)	0.00573(7)
R_{wp}	0.057	0.213	0.201	0.227

Table 5.2: Comparison of refined parameters of the distorted Ti_2Sb model between the (RA-)PDF and single crystal diffraction methods.

5.2.3 Discussion and conclusions

Structure characterization of the new metallic binary antimonide Ti_2Sb was carried out with single crystal diffraction, powder diffraction, and the RA-PDF method. Both the average structure and local structure were successfully obtained with those complementary studies. More importantly, this study proves again the Kleinke-Harbrecht

structure map capable of predicting the previously unknown Ti_2Sb structure. One very interesting structural feature for this compound is a new type of distortion of one metal atom layer that is a perfect square planar net in its aristotype La_2Sb. The corresponding distorted Ti2 net of Ti_2Sb comprises squares and rhombs in a 1:1 ratio, as shown in Fig. 5.3. It is worth noting that combined X-ray and neutron PDF refinement with the same model was also performed.

High real space resolution RA-PDF analysis of Ti_2Sb powder diffraction data is exemplified in this study. In the mean time, high resolution PDF analysis of neutron powder diffraction was carried out and gave structure details in excellent consistency with the RA-PDF method. It is noteworthy that their reciprocal space resolutions are rather different from the $F(Q)$ peak widths in Fig. 5.4. However, the local structure in the low r PDF region is not affected at all, while the high r PDF data from the RA-PDF method quickly loses intensity compared to the neutron PDF (Fig. 5.6). This stands as a limitation of the RA-PDF method where high real space resolution compromises the reciprocal space resolution due to the finite IP size [10]. Nevertheless, the RA-PDF method shows to be a very powerful and fast way to probe the local structure. The author also would like to note that the X-ray sample was received on the last morning of the experiment. The successful data collection of a complete data set would not have been possible without the fast RA-PDF method.

5.3 *In-situ* chemical reduction of CuO to Cu

This is an example of *in-situ* time resolved powder diffraction studies in heterogeneous catalysis by coupling the study of long range and local structural changes. Most of the work described here was done by our collaborators (see reference [178]). The application of *in-situ* time resolved powder diffraction to study structural changes that occur during chemical reactions has become a standard method at synchrotron sources. With respect to heterogeneous catalysis, the understanding of the structural

changes, both on the local and long range length scales, that are the consequence of reaction conditions is paramount to fully understanding the functioning of many catalysts. Time resolved diffraction experiments which combine high-energy X-rays (>80 keV) with area detectors open the possibility of coupling both reciprocal and real space methods to probe both long range and local structural changes simultaneously [61]. This is particularly advantageous in the study of chemically induced structural changes, commonly encountered in heterogeneous catalysis. Here we illustrate the application of the approach to monitor the reduction of CuO, a material that is ubiquitous in compositions of methanol synthesis and water-gas shift catalysts [179]. Activation of the catalysts requires reduction of the CuO, producing small metallic Cu particles which are the active centers for catalysis. We have therefore been studying the reduction of CuO under controlled conditions using H_2 to examine the formation of centers active for catalysis [180].

5.3.1 Experiment

All diffraction experiments were performed at the 1-ID beamline at the Advanced Photon Source (APS) located at Argonne National Laboratory, Argonne, IL (USA). High energy X-rays were selected using a double bent Laue monochromator capable of providing a flux of 10^{12} photons/second and operating with X-rays in the energy range of 50-200 keV.

In-situ diffraction experiments were performed with a specially designed flow cell (Fig. 5.7), which allows for flow of reactant gas over the sample during acquisition of powder diffraction data. The temperature was controlled in steps as follows; 2 hour ramp from room temperature to 350°C C. During the experiment 4% H_2 in He was passed over the sample at a rate of 8 cc/min. A MAR345 image plate camera was mounted orthogonal to the beam path, with the beam centered on the IP. When using the 99 keV X-rays, a LaB_6 standard was used to calibrate the sample to detector

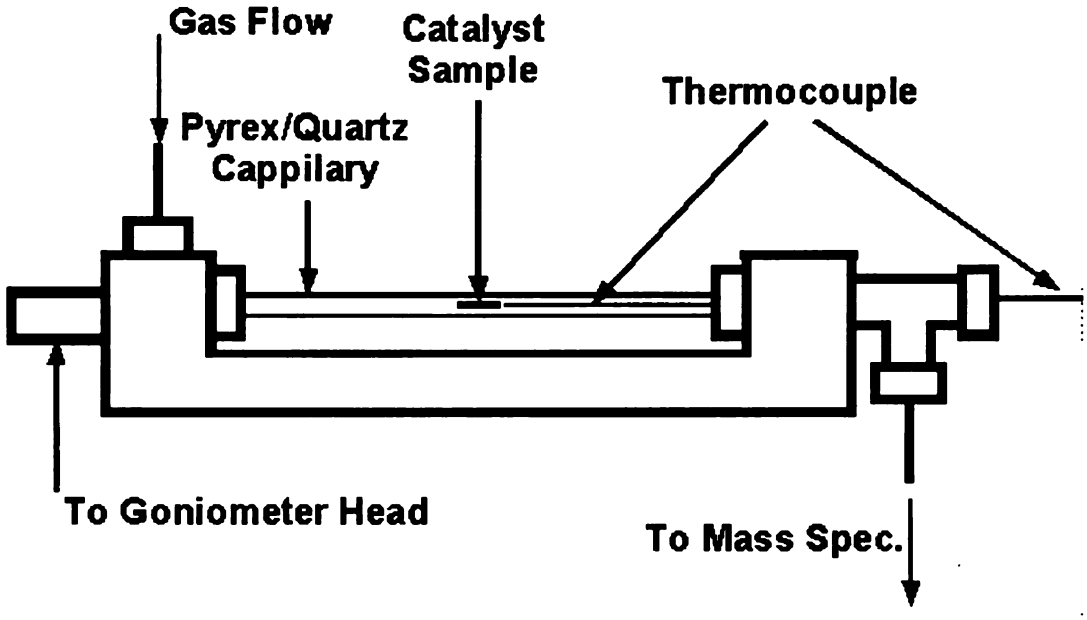

Figure 5.7: Schematic diagram of the flow cell used in the RA-PDF experiment.

distance and tilt of the IP relative to the beam path, using the software Fit2D [64]. All raw two-dimensional image data were integrated using the software Fit2D and files output as intensity versus 2θ. Ten second exposures yielded data that provided very good statistics for the refinement techniques described below.

5.3.2 Results

The in-situ reduction of CuO was followed using high energy X-rays coupled with a two dimensional image plate (IP) detector. The results are shown in Fig. 5.8. The reduction of CuO to Cu metal takes place at approximately 280°C C. The reduction to Cu is quite fast and occurs on the order of minutes. During this period both CuO and Cu are evident, and we are currently investigating the structural changes that occur.

High energy X-rays provide several experimental advantages in the structural analysis of time resolved data. Utilization of high-energy X-rays allow for larger values of momentum transfer to be probed (> 18 Å^{-1}), opening up the possibility for the application of real space methods (pair distribution function, PDF, analysis) to

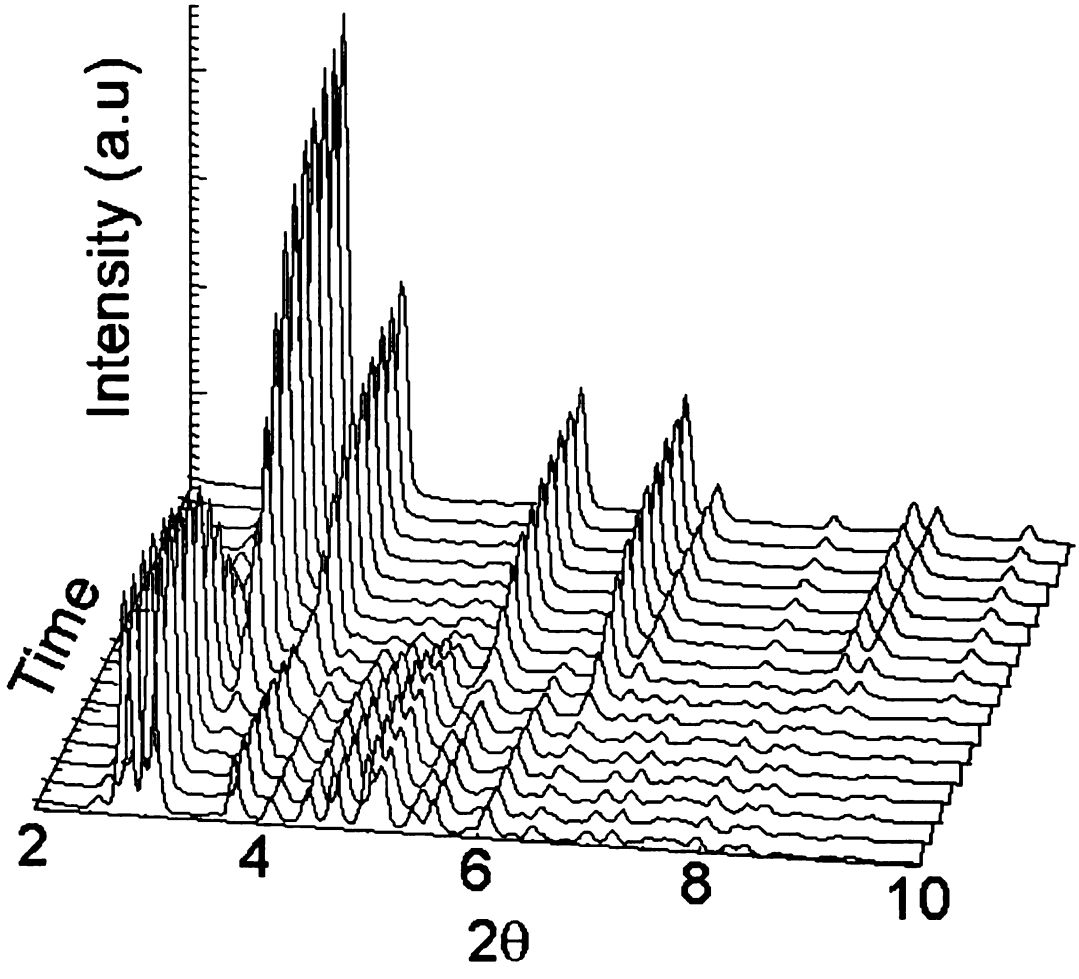

Figure 5.8: Powder diffraction pattern during the chemical reduction of CuO to Cu.

probe changes to local structure during reaction conditions. The $G(r)$s obtained from the diffraction patterns (IP data) at the beginning of the *in-situ* experiment and at the end of the *in-situ* experiment are shown in Fig. 5.9. For example, the first Cu-O peak drops dramatically and a new peak at 2.6 Å (Cu-Cu) is observed. Traditional Bragg refinement of the same diffraction data used for PDF analysis provides for an improved parameter to data ratio. Exceptional Bragg profile refinements of beginning and final phases can be obtained, but disorder in mixed phase results in poorer fits and significant features in the difference electron density maps, which we are attempting to interpret. Following the reduction using real space methods may open up the further understanding of the reduction process, as the changes to the Cu-O coordination during the final stages of reduction may not be evident in the Bragg

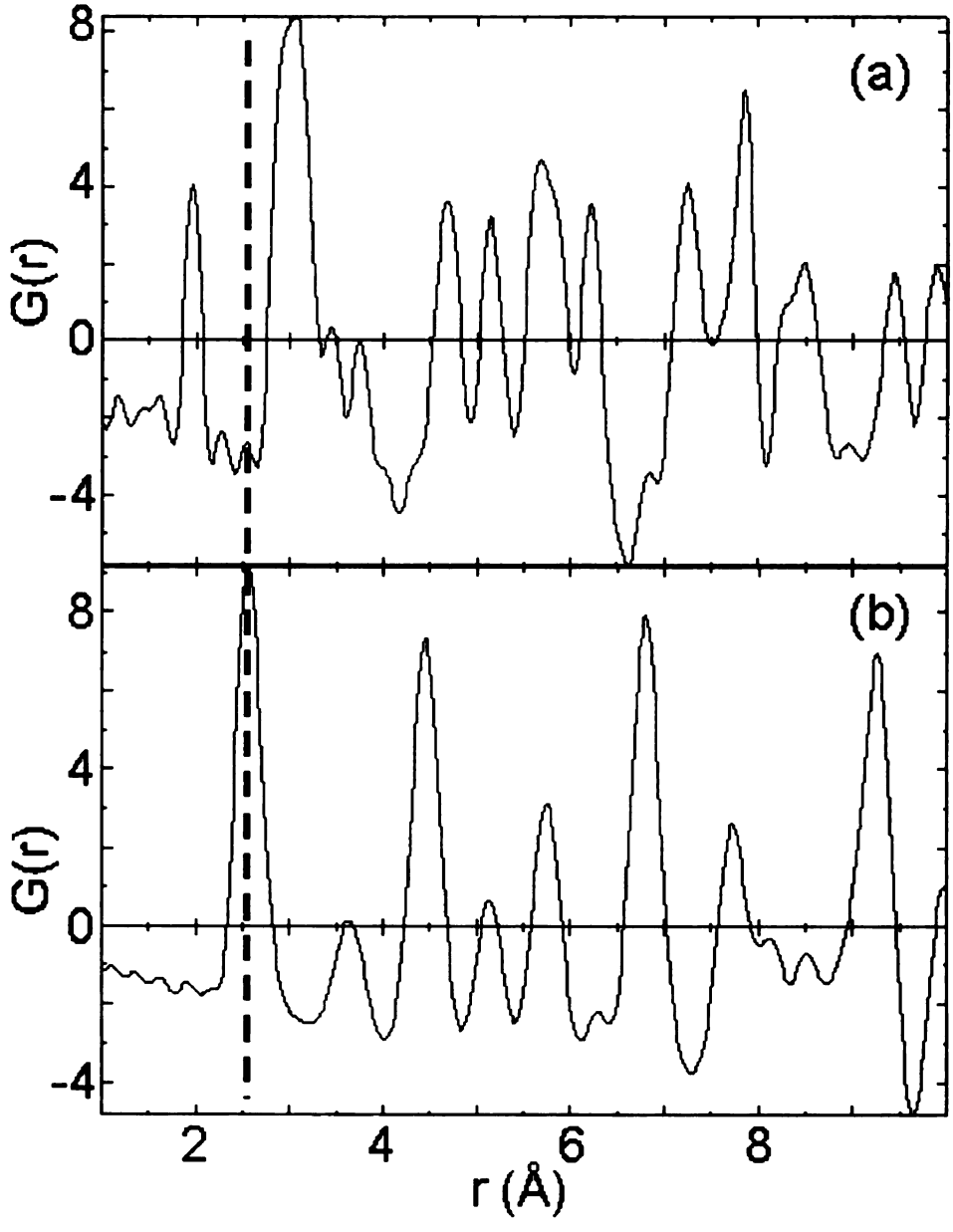

Figure 5.9: $G(r)$ for (a) CuO at the beginning of the time resolved experiment and $G(r)$ for (b) Cu formed at the end of the time resolved experiment. The guideline shows the Cu-Cu first shell distance.

profile refinements.

5.3.3 Conclusion

High energy X-rays open up the possibility for qualitatively new time-resolved experiments which couple both reciprocal and real space approaches to structural analysis.

The application of X-rays with energies between 80-120 keV allows for collection of powder diffraction data to high momentum transfer (>18 $Å^{-1}$) using commercial image plate cameras at sampling rates which will allow monitoring relevant structure changes under process conditions. This allows for both Rietveld and PDF analysis to be carried out on the *same* data sets probing both long range and local structural changes simultaneously.

Chapter 6

Concluding Remarks

6.1 Summary of the thesis

We set out to determine the local structure of disordered crystalline materials, employing the atomic pair distribution function (PDF) method [5]. As the demand of atomic local structure characterizations is growing (see Chapter 2), the PDF technique is emerging as a promising tool for this purpose. Neutron and X-ray powder diffraction experiments have been exclusively used to obtain the experimental PDFs. The novelty of the PDF technique is to take into account both the Bragg peaks and diffuse scattering intensities, as a total scattering probe. Obtained via the Fourier transform from the reciprocal space, the PDF method is a unique local structural probe that presents information in the more intuitive real space [22], and contains structural information at all length scales. The ultimate goal is to understand the fundamental structure-property relationship driven by our sheer scientific curiosity, and then be able to manipulate the structures and/or properties according to our technological needs.

The recently developed rapid acquisition PDF (RA-PDF) method [61] made a leap forward by reducing the data collection time by three to four orders magnitude. The key components of the RA-PDF method are high flux high energy X-rays and an

automated image plate area detector. A new program PDFgetX2 [41] implemented necessary additional corrections to the RA-PDF data, and significantly simplifies the intensive data analysis with the built-in user-friendly graphic user interface (GUI). The proof-of-principle and systematic quality studies established that high quality experimental PDFs can be routinely obtained from materials with wide ranges of atomic Z numbers. The measurable extended reciprocal space range provides the high real space resolution essential to local structure approaches [10]. RA-PDF data have low Q-resolution and this method is not suitable for measurements requiring high reciprocal space resolution. The RA-PDF method has resulted in numerous publications [61, 178, 174, 181], and opens up future possibilities for wide-spread PDF applications.

Relevant to this thesis work, the RA-PDF method has been applied to study the distorted Ti2 square nets in the new binary antimonide Ti_2Sb, in combination with neutron PDF data analysis. The Ti2 square net is confirmed convincingly to distort locally. This example shows one strength of the PDF technique, probing the local distortions inaccessible (or inconclusive) to conventional crystallographic analysis. The other example was the combined PDF and Rietveld study of the *in-situ* chemical reduction of CuO to Cu. The fast RA-PDF measurement makes it possible for following the *in-situ* chemical reactions in real time, while still giving high quality PDFs. In fact, the PDF analysis appeared to be more advantageous than the Rietveld analysis due to the presence of significant diffuse scattering and non-crystalline forms during the reduction. The PDF directly probes the local interatomic distance distributions regardless of the long range structural coherence. The resulting coordination numbers (Cu-O, Cu-Cu) reveal important information such as the "phase" fractions. Within its current capabilities, the time development of chemical reactions and biological systems over time scales of minutes can be studied, as well as, in the future, the pump-probe experiments.

The colossal magneto-resistive (CMR) manganites are fascinating strongly correlated electrons systems challenging our current understanding of condensed matter physics. The atomic local structure plays important roles via the strong interplay between electron, spin, and lattice degrees of freedom. The MnO_6 octahedral Jahn-Teller (JT) distortion is a direct result of the strong coupling between the electrons and the lattice. The undoped parent compound $LaMnO_3$ shows a very interesting, but not fully understood, phase diagram, even without the additional complications such as the admixture of Mn^{3+} and Mn^{4+} ions and pinning effects induced by doped cations in the doped compounds. Our PDF analysis of the JT transition around 750 K continued and extended the same local structural results as earlier XAFS studies [129, 130]. The nature of the JT transition is found to be orbital order to disorder. Our high temperature data in the rhombohedral phase ($T > 1010$ K) discovered the locally JT distorted MnO_6 octahedra while strictly regular MnO_6 octahedra are indicated by an average structure analysis. We have also shown that the PDF analysis can obtain the average structure in quantitative agreement with the Rietveld refinements. More significantly, the intermediate range structure information could be extracted from our PDF analysis by following how the refined structure evolves with the change of the PDF r range that is fit over. In the orbital disordered states at high temperatures, we found the existence of short range ordered domains. The domain size was estimated by the crossover from local to average structure, both of which are obtained from the PDF analysis. This domain size is found to be around 16 Å spanning over four MnO_6 octahedra, suggesting strong nearest neighbor anti-ferrodistortive JT coupling and weak second nearest neighbor coupling. The importance and delicacy of the interplay between electron and lattice degrees of freedom is again borne out of our study, which also illustrates that the PDF gives structural information at all length scales.

The bi-layered manganite $La_{2-2x}Sr_{1+2x}Mn_2O_7$ shows great similarities to the equivalent "cubic" manganite, as well as intriguing differences. In particular, we studied

the Mn^{4+} rich region ($x > 0.5$). One example is to detect the local MnO_6 octahedral shape change across the temperature driven orbital occupancy transition from $d_{x^2-y^2}$ to $d_{3z^2-r^2}$ at $x = 0.54$. This orbital occupancy transition brings the MnO_6 octahedron from oblate (two short, four long Mn-O bonds) to prolate (four short, two long Mn-O bonds) upon warming. This Mn-O bond length distribution transition is evidenced by the excess decreases of the Mn-O and O-O PDF peak heights across the transition. Behaviors consistent with this proposed oblate to prolate octahedral transition are also observed in the thermal displacement parameters of the in-plane oxygen atoms, and the lattice constants. Coexistence of the two orbital occupancies is invoked to explain the observed smooth crossover. The other example concerns the Sr-doping x driven phase separation at nano-scales within the range $0.54 \leq x \leq 0.80$ [182]. We can also understand this as the increasing stability of the $d_{3z^2-r^2}$ orbitals with increased Sr-doping. The $d_{3z^2-r^2}$ orbital occupancy at low Mn^{3+} concentrations (large x) results in the orthorhombic phase. We show evidence supporting the smooth growth of the local orthorhombic phase with Sr-doping, instead of the sharp abrupt tetragonal to orthorhombic crystallographic phase transition at $x = 0.74$ observed on the average structure [150]. It can also be understood that the sample $La_{2-2x}Sr_{1+2x}Mn_2O_7$ in the Mn^{4+} rich region $0.54 \leq x \leq 0.80$ shows intrinsic inhomogeneities ("phase" separation) at nano-scales.

6.2 Future work

In this section, some future possibilities are discussed. The discussion will be taking the view of the PDF technique, instead of each individual research project.

6.2.1 Measuring more PDFs

The RA-PDF method considerably simplifies X-ray PDF measurements, while being three orders or more faster than the conventional X-ray PDF data collection [61]. With high energy X-rays, thicker samples can be measured due to the weak sample self-absorption effect. The third generation synchrotron source provides X-ray beams with significantly boosted brilliance [62]. As a consequence, the necessary total sample exposure time is usually in the order of tens of seconds, which already provides high counting statistics. The limiting factor to data collection time becomes the image plate read-out and erase-off time, which is about three minutes for a single exposure. Thus, we can further improve our data rate by another factor of three if the data operation time of the area detector can be significantly reduced. One solid state area detector (detection media is amorphous silicon) has been tested in our collaborations, which gives 18 frames per second data throughput. The other alternative is the charge coupled device (CCD). The active area of commercially available CCD is close to the image plate size we are currently using (345×345 mm^2), e.g., 315 mm of Quantum 315 model. It will be great to test those two types of area detectors for quantitative PDF analysis in the near future. Various technical issues/difficulties are expected, however, these detectors present a very interesting prospect. For time resolved measurements, a few seconds of exposure time usually suffices to obtain PDFs with acceptable quality for time dependent comparisons. Even in this case, the time resolution of the RA-PDF can be improved by at least two order of magnitude, i.e. from around three minutes to one second level. This would make another leap forward in the PDF applications especially on time-resolved studies. Just to mention about neutron PDF measurements, we currently are using large sample size (6–10 gram), large beam size (5×1 cm^2), and multiple banks of detectors. Thus, neutron data collection is to a large extent beam flux limited. Though slow, the neutron measurements are indispensable, being complementary to X-ray experiments.

A significant amount of additional work would be very much welcome on the bi-layered manganite compounds. One very interesting experimental observation is the re-entrant charge ordering behavior of the $La_{2-2x}Sr_{1+2x}Mn_2O_7$ near $x = 0.50$ around 50 K [183, 155, 184, 185]. We would expect the PDF peaks heights to be lower in the charge ordering temperature region. As the deviations from normal Debye behaviors is better characterized with denser data points, the RA-PDF method should be useful. Anomalies in electric transport data have also been reported in the higher Sr-doped regions [185], temperature dependent measurements at high doping levels would be very promising. In addition, I am particularly interested in the local structure of $La_{2-2x}Sr_{1+2x}Mn_2O_7$ at $x = 0.4$. Though the local structure of the Sr-doping level at $x = 0.3$ has been studied with the PDF method [162], the $x = 0.4$ compound is still very interesting due to their rather different magneto-resistive transport behaviors [151].

6.2.2 Obtaining high quality PDFs

The accessible reciprocal space range has been significantly extended with the available high energy X-rays and faster epi-thermal neutrons [5]. The real space resolution of the PDF has been shown to reach the order of one tenth of an Angstrom [16, 186], which becomes comparable to the intrinsic PDF peak width broadening set by the atomic thermal motions. Though with high real space resolution, the obtainable quality of the PDF is sample dependent. As high quality PDFs can be straightforwardly obtained from the "good" materials, improved data analysis methodologies are necessary to handle the "bad" compounds. For neutron PDF data analysis, samples with high absorption cross section or significant incoherent scattering cross section belong to the "bad" category, e.g. highly absorbing samples necessitate very accurate absorption and multiple scattering corrections. For X-ray PDF data analysis, very low Z ($\leq$ 10) materials are troublesome because of the dominating Compton scattering

at high Q region. It is worth noting that the low Z materials represent an extremely interesting and important group such as organic and biological samples.

The origins are the imperfections in the data corrections. In some cases, the assumptions made in the theoretical/empirical corrections simply fail, e.g., multiple scattering is usually calculated up to secondary scattering only [187, 188, 189, 190], and absorption of elastic and inelastic scattering intensities are taken as the same [44, 41]. Other cases are that some compiled theoretical profiles used in the data corrections have large uncertainties [191, 192, 193] in the high Q region in real material systems. For example, the tabulated atomic form factors are for neutral atoms and some common ions. While this is a reasonable approximation for high Z elements, the change of outer-shell electron densities of low Z elements in the material modifies the scattering form factors rather considerably. The Compton theoretical profiles only have high accuracy up to Q_{max} of 16 $Å^{-1}$ [192, 194], while the experimental data commonly reach as high as 35.0 $Å^{-1}$. Therefore, quantitative analysis of the scattering intensities at high Q calls for more accurate theoretical calculations. On the other hand, to extend the capability of the PDF method, careful experimental studies of those various effects can be carried out and corresponding solutions can be implemented. More specifically, neutron samples with wide ranges of absorption or incoherent cross section can be studied to investigate which corrections are limiting our data analysis. For RA-PDF experiments, the energy dependence of the image plate phosphor layer transmission coefficients are best measured over a wide X-ray energy range, e.g. 20 to 120 keV; the calibration data on the energy dependence of the image plate response needs to be extended to higher X-ray energies ($\sim$ 120 keV) as well; the angular dependence of the fluorescence intensities due to self-absorption can also be verified with a multiple channel analyzer (MCA).

6.2.3 Combining complementary probes

The strength of the PDF technique lies in the local and intermediate range structure information. Thus the conventional crystallographic methods probing the long range ordered structure can be naturally combined with the PDF analysis. This has been routinely exercised, providing complementary and unique insights into the real structure of materials. The PDF measurement takes the average over all powder grains, all atoms, and the solid angle. This makes it less sensitive to longer range structure motifs, such as phase separation in the range of tens of nano-meters. In this case, the joint probes with microscopy measurements are very appealing such as scanning tunneling microscopy (STM), high resolution transmission electron microscopy (HR-TEM), and atomic force microscopy (AFM).

The neighboring environment of atoms influences quite diverse material properties, such as the electronic structure, magnetic exchange coupling, phonon dispersions. Knowledge of the atomic structure will be greatly complemented by the knowledge of the lattice thermal dynamics, macroscopic electronic and thermal transport properties. In view of this, it will be very beneficial to collect first-hand data on the same sample with complementary techniques such as thermal analysis measurement, electric conductivity measurement, neutron and X-ray inelastic scattering measurement. Detailed atomic structure also often serves as the basis for many theoretical calculations such as the band structure computations.

6.2.4 Applying the PDF technique in new areas

The purpose of the PDF technique is to answer significant scientific and/or technological questions suitable to this method. One very effective way is to bring the PDF technique to a wider user community. Widespread use of the PDF method could bring in a large number of new users and have significant impact in various scientific disciplines. On the other hand, the capability and application scope of the PDF

technique needs also to be expanded. Here we will discuss a few possibilities.

Single crystal diffuse scattering (SCDS) measurements also look at the same diffuse scattering intensities as the PDF powder diffraction measurements. Though more time consuming, the SCDS method gives more information due to the absence of powder averaging. Borrowing from the PDF method the idea of a real space probe via Fourier transform, we can obtain the three dimensional PDF from SCDS data. It will be also interesting to obtain the two dimensional PDF from two dimensional structures such as films, surfaces, and interfaces. Another fermenting idea is the magnetic PDFs with polarized neutron scattering experiments, which can separate the magnetic and nuclear scattering components through polarization analysis.

Conventional time resolved diffraction experiments should benefit from the PDF analysis by adapting the RA-PDF setup, i.e., using high energy X-rays and shortening the sample to detector distance. In particular, the potential PDF applications on the time development of biological systems are very appealing. While the shape and conformational changes are probed by the global structure approaches such as optical microscopy and small angle scattering, the change of local environments, e.g., breaking or forming of some specific bonds, can be studied with the PDF method, which is rather sensitive to small local structural changes. Much improved RA-PDF time resolution is also expected with either the solid state area detector or CCD. I am looking forward to the future exciting developments. As the amount of data coming from those experiments will be huge, the efficiency of current data analysis methods needs to be improved correspondingly.

6.3 Acknowledging funding agencies

The work at MSU benefited from support from the following agencies, National Science Foundation through grants, DMR-0075149, DMR-0211353, CHE-9903706 and CHE-0211029, Center for Fundamental Materials Research at Michigan State Uni-

versity, U.S. Department of Energy through grant DE-FG02-97ER45651.

This work has benefited from the use of NPDF at the Lujan Center at Los Alamos Neutron Science Center, funded by DOE Office of Basic Energy Sciences and Los Alamos National Laboratory funded by Department of Energy under contract W-7405-ENG-36. The upgrade of NPDF has been funded by NSF through grant DMR 00-76488.

The work at ANL and beam time at IPNS and APS is supported by the US Department of Energy through grant No. W-31-109-ENG-38.

Appendix A

The rapid acquisition pair distribution function method experiment

The rapid acquisition pair distribution function (RA-PDF) experiment will be described in detail as follows.

A.1 Requirements of the experiment

To collect powder diffraction data suitable for PDF analysis, a few requirements have to be met.

Extended Q range The finite Q space measurement range directly determines the experimental real space resolution of the PDFs [10]. As the physical size of the IP is fixed, the desired Q range defines the relation between X-ray energy and the sample to detector distance. In practice, the probed Q_{max} is determined by the particular question to be answered by the experiment. However, to reduce the effect of the termination ripples due to the cutoff in Q space, $Q_{max} \geq$ 18.0 Å^{-1} is generally necessary. Much higher Q_{max}, e.g. $\geq$ 30.0 Å^{-1}, is required for

highly crystalline materials.

Good counting statistics To obtain quantitatively reliable structural information, a certain level of counting statistics is necessary. As the scattering is a random event, the measured counts follow the Poisson distribution. When the number of measured scattered photons is large, its uncertainty is simply the square root of the measured counts. An empirical rule of thumb is to collect around one million counts per inverse Angstrom.

Good signal to background ratio This can be part of the second requirement. However, this requirement is of special importance, and tricky as well, mostly because more than one scattering process contributes to the measured total counts and only elastic coherent scattering is used in the PDF analysis. To achieve a good signal to background ratio, it is necessary to have a good estimate of what fraction of the total counts is the elastic signal sought after. For example, at Q just as high as 25.0 Å^{-1} for Si atoms, the Compton scattering intensity is 8 times the elastic intensity. If 1% is the desired relative uncertainty, you will need as many as 640,000 counts. Still chances are you are looking for even smaller changes in the elastic scattering intensities, which calls for more counts. In principle, it is difficult to know the expected signal *a priori*. The best approach is to analyze the data during the experiment, then decide whether more collection time is necessary.

A.2 Setup of the RA-PDF experiment

For practical reasons, the procedure to set up the experiment will follow the flight path of the X-rays, which means from upstream to downstream. The first thing is to choose the right beam line with proper X-ray characteristics for your specific experiment. Experimental setup in the early stages is similar to our conventional

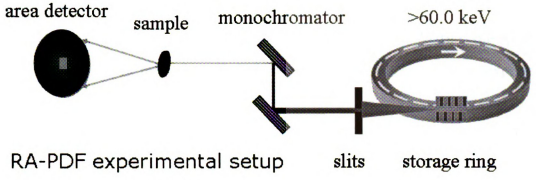

Figure A.1: Schematic diagram of the rapid acquisition PDF (RA-PDF) experiment layout.

PDF X-ray experiments. The schematic diagram of the RA-PDF experimental setup is shown in Fig. A.1.

1. Set the energy. This step doesn't need to be the first, and commonly it's necessary to change the X-ray energy during the experiment. Nonetheless, a few ways to calibrate the energy are briefly explained here. In principle, we can compute the X-ray energy given the monochromator tilting angle and the reflection plane used. However, those calculated values are usually only good approximations due to the various uncertainties in the tilting angle, etc.. One commonly used approach is to scan across the absorption edge of a standard material, such as Pb, or Au K edges, and use their well known absorption edge energy values as references. The other way is to use multiple channel analyzer (MCA) to locate the incident beam energy. One complication of this method is the MCA needs to be calibrated first, usually with a set of standard radiative materials which have characteristic emission lines. A common step after this is to align the center of the slits so that the incident beam passes through the centers. This can be done automatically by monitoring the downstream beam intensities when moving the slits.

2. Set the slit openings to give you the proper beam size. We have used 0.5×0.5

mm at both 1ID-D and 6ID-D at APS. The primary considerations for beam size are usually the Q space resolution and incident X-ray flux. With some approximations, starting from $Q = \frac{4\pi}{\lambda}\sin\theta$, the resolution function can be expressed as,

$$\frac{\Delta Q}{Q} \approx \frac{\Delta\lambda}{\lambda} + \frac{\cos^2(\theta)\cos(2\theta)}{1+\sin^2(2\theta)} \times (\frac{\Delta d}{d} + \frac{\Delta r}{r}) \tag{A.1}$$

where d is the sample to detector distance, r is the distance of the pixel from the center of the image plate. In our typical RA-PDF experiments, the maximum 2θ angle is about 30.0 degrees. We can show that the first term $\frac{\Delta\lambda}{\lambda}$ is the smallest, usually in the order of 10^{-4} determined by the characteristics of the monochromator(s). The prefactor of the Q dependent second term varies from 1.0 to 0.65 as 2θ goes from 0.0 to 30.0 degrees. The typical value of $\frac{\Delta d}{d}$ is $\frac{1.0}{200.0} = 0.005$ with 1 mm thick sample and 200 mm sample to detector distance. Δr can be estimated as the sum of beam dimension and image plate pixel size (0.1×0.1 mm), while r value ranges from 0.0 to 172.5 mm. If we simply take 100.0 mm as the mean value of r, the $\frac{\Delta r}{r}$ becomes comparable to $\frac{\Delta d}{d}$ with beam dimension of 0.5×0.5 mm. A much larger beam size than this would make it the limiting factor to the instrument resolution. There are also some other considerations as well, such as the intrinsic beam size, the incident beam intensity, scattering powder of the sample and so on. Around 0.5×0.5 mm beam size is used in our RA-PDF experiments.

3. Align the center of the diffractometer with the beam center. This involves two steps. We first locate the center of rotation of the diffractometer usually with help from a telescope. A sharp metal pin is mounted on the goniometer, and the goal is to get the tip of the pin in the same place when any circle of the diffractometer is rotated. Once you have done this, use the motor to adjust position of the diffractometer to set the tip of the pin on the beam center. You

can use a monitor or burn paper or fluorescent screen to do it. The easiest way is to place a Silicon diode detector after the pin and do x-y scanning of the diffractometer. Once this is done, remember the current position of the pin tip in the telescope, or move the telescope so that the pin tip sits in an easy to remember position, e.g. the center cross. This is the beam center and the center of the diffractometer after the alignment.

4. Put the image plate detector to its approximate position. You will need to adjust it later. In most cases, the only variable here is the sample to detector distance. As the dimension of the image plate (e.g. 345 mm in diameter for Mar345 detector) is fixed, given the energy you will be working at, you can compute the necessary maximum 2θ, and then the sample to detector distance $d(mm) = 172.5/\tan(2\theta)$. For example, if you want to achieve Q_{max} of 35.0 Å^{-1} at 100 keV with the Mar345 detector, the sample to detector distance needs to be 202.5 mm.

5. Install the beam stop and align it. Before you open the beam shutter, make sure to have Pb shielding right in the front of the image plate detector. Direct beam WILL damage the IP permanently! The best way is to put a Silicon diode monitor after the beam stop installed on a translation stage. Through scanning the beam stop positions, you can quickly position the beam stop to fully intercept the incident beam.

6. Align the image plate detector within a reasonable amount of time. One goal is to set the beam center close to the detector center. The other is to achieve a good orthogonality of the plate plane to the beam direction. This requires the use of a calibrant, for example, fine Si powder. Program FIT2D [64] provides an easy-to-use interface to do this job. One important consideration for this purpose is to minimize the uncertainties in later corrections. For example, the

oblique incident angle dependence correction assumes that the same Q values around the ring have the same incident angle to the IP.

7. Take efforts to reduce the background. The RA-PDF experiment subjects to rather high background levels. Most background intensities come from air scattering. Thus the first step here is to shield out the air scattering before the sample by placing a thick Pb plate with a hole at the center for the incident beam. If there is a considerable gap between the Pb shield and the sample, a collimator right in front of the sample is preferred. During experiments, usually more than 50% incident beam is allowed to pass through the sample. The rather long sample to beam stop distance ($\geq$ 150 mm) creates a significant amount of air scattering. The collimation after the sample is in principle hard to implement. One way is to shorten the sample to beam stop distance, however, this would increase the blocked scattering angle by the beam stop. A very effective way would be to use an evacuated second flight path, however, more difficult in practice. The background scattering in practice only becomes an issue for weakly scattering samples.

8. Install additional equipment required for your experiment. For example, the displex with cryostat needs to be set up for low temperature measurements. In the case of high temperature measurements, the furnace should be installed.

Once you are satisfied with the position and tilt of the image plate, write down the values you get, such as the sample to detector distance, beam center, tilt angle, etc. We are ready now to do some real measurements on samples.

A.3 Collecting RA-PDF data

This briefly describes some common actions during RA-PDF measurements. The RA-PDF data collection mostly involves changing samples and controlling the data

acquisition system. Operation of data acquisition system works varies at different beamlines. However, changing samples is essentially the same. As the sample to detector distance is obtained from the calibration runs (with Si or LaB_6), we need to put the sample at the same position as the calibrant. This is usually done with the help of the telescope indicating both the center of the beam and center of the diffractometer. However, the RA-PDF setup requires a very close sample-to-detector distance, e.g. 202 mm. It might happen that the telescope view of the sample is blocked by the image plate detector. If this is the case, alternative ways of ensuring the same sample positions should be implemented, such as a monitor screen, identical sample holders etc.. If possible, a small telescope can be mounted on the diffractometer for sample alignment. When changing the sample, be sure not to bump the beam stop. A significant shift of the beam stop requires realignment of the beam stop, and another set of measurements of the background scattering.

If the X-ray energy needs to be changed and a new sample to detector distance becomes necessary, extra attention needs to be paid in order not to lose the calibration. This is because the sample to detector distance and the X-ray energy are strongly correlated in the calibration. ONLY one of them can be unknown to get any sensible calibration. You can either change the X-ray energy or move the detector first, then you do the calibration, and then you change the other one. If only room temperature measurements are performed, moving the sample is much simpler than moving the detector because the later almost always requires some aligning adjustments of the detector.

Beam exposure time depends on the scattering power of the sample and the incident beam intensity. The rule of thumb is to keep all the counts in the linear response regime of the image plate. In our case, the maximum count of in each pixel is 64,000 set by the electronic readout device. A reasonable maximum intensity for our data is advised not to exceed 60,000 (though a maximum of 131,000 of 17 bits is possible

with two sets of PMTs). Grainy samples may cause sparse pixel saturations even with very short exposure times because of those crystals with considerable sizes. Certainly the best solution is to have fine powdered samples. As grinding samples may be not possible during the experiments, we may try to do more sample rocking, or try another section of the sample. However, we should not worry about the small number of saturated pixels in our data. First, they can be removed during the data processing. Second, the relative error would be rather small compared to the total number of pixels, e.g. $\sim$ 10,000,000 pixels in the Mar345 detector.

To properly analyze the RA-PDF data, we need to also measure the background and other calibration data if necessary. Here the background refers to the sum of the container scattering and the empty instrument scattering (mostly air scattering). The background intensities will be subtracted from the sample total intensities during data analysis. When the background level is rather high, the absorption correction due to the existence of the sample in the beam (when collecting sample data) becomes necessary. This correction is usually rather tricky since it depends on the detailed experimental setup. Strictly speaking, different absorption corrections also become necessary when the container itself scatters (absorbs) considerably. For the most commonly used kapton tape in our lab, the scattering from the container itself is small compared to the air scattering, and there is no need to distinguish between the container and empty instrument scattering. If a glass capillary is used, the scattering from it may be very strong. We may need to measure the empty instrument separately. As the background scattering is usually slowly varying intensities, they can be smoothed during analysis without compromising the analysis. Thus, the issue of counting statistics is less critical for background measurements.

In the end, you should have the data for the sample, data for the background, and data for the calibration.

A.4 Processing the data

Here the data processing refers to the procedure to obtain PDFs from the RA-PDF data (for more detail see Chapter 5 of [5]. The conventional way to obtain PDFs starts from the SPEC file format data collected with a solid solid detector (SSD), and is described in detail in the tutorial of program PDFgetX2 [41, 195]. A simplified version is described in the following. The raw data from our SSD detector are in SPEC data file format. The program PDFgetX2 [41] was used to preprocess the raw data to obtain the intensity versus 2θ two column data. In the preprocessing, the measured scattering intensities were first corrected for detector dead time (e.g., 0.84 μs), then normalized by the corresponding incident beam intensities (monitor counts collected by one ion chamber right before the sample). Then the two scans were merged together to yield the whole range. The same procedure was repeated on the background scattering data. After the preprocessing, the background data is subtracted from the sample data to obtain the sample only scattering intensity versus 2θ. Following applied corrections are the sample absorption, polarization, and Compton scattering to obtain the elastic scattering only. The last step is to normalize the elastic scattering by the Q dependent average scattering power of the material to get the total structure factor $S(Q)$, which is then transformed to obtain the experimental $G(r)$ with the formula: $G(r) = \frac{2}{\pi} \int_0^\infty Q[S(Q) - 1] \sin Qr \, \mathrm{d}Q$.

However, the data coming from the image plate are two dimensional images, and thus need to be integrated first to give the multiple column ASCII data. One column should be the intensity, while there should also be one column being either 2θ or Q. The integrated data can then be fed to program PDFgetX2 to obtain the PDF as described above.

A.4.1 Obtain calibration parameters

The image plate data are simply a two dimensional matrix of the intensities. Thus we first need to know the 2θ or Q value of each matrix element, which requires the following parameters: the pixel size, the beam center (x, y), the sample to detector distance, the X-ray energy, and the tilt of the image plate relative to the incident beam. In practice, we know before hand the pixel size that depends on the laser scanning mode during read-out, and either the X-ray energy or the sample to detector distance. The other parameters are obtained through the calibrations with sample standards. The program FIT2D [64] has been our choice of software for obtaining those parameters. One additional parameter, the X-ray polarization factor, will be used during data integration. You can get this number from the instrument scientist. All those parameters are critical to the accuracy of our data, and thus should be kept well. This also means to repeat the calibration whenever the experimental setup changes.

A.4.2 Integrate the IP raw data

The goal here is to get a two column data set equivalent to the conventional angle dispersive scan, where every data point represents the sum of scattering intensities over the same solid angle. In the image plate data, different Q values have different number of corresponding pixels. This necessitates an additional geometric correction to properly normalize the data. The X-ray polarization correction should also be done at this step, because it depends not only on the distance of the pixel from the beam center, but also on the azimuthal angle. Data integration can be done straightforwardly with FIT2D with the choices of above corrections. The integrated data should be saved in "CHI" file format. It's also recommended to save it to GSAS [68] format for later Rietveld analysis.

For each sample, we usually take multiple exposures to achieve better counting

statistics. Since the multiple data sets are measured under identical conditions, we directly sum them together to get the total counts. To avoid too large values, we divide the total counts by the number of exposures .

Batch integration is possible with the FIT2D GUI macro functionality. This becomes necessary when there are a large number of data files to integrate, as is the case for our RA-PDF experiments. A more efficient way is to use the keyboard mode in which program FIT2D can be driven by command line inputs. In this case, we can put all the commands in a macro file, and give the macro file name to FIT2D to achieve the same result. Certainly the macro file should contain information such as the needed processing parameters and the related image plate data file names. Many samples are usually measured with the same experiment setup, thus only the data file names need to be changed in the macro file. In consideration of this, the macro file is designed to take parameter values from variables, and the variable values can be passed when calling FIT2D. The current version of FIT2D macro file is the following for your reference.

```
%!*\ BEGINNING OF mar_integrate.mac MACRO FILE
%!*\ This is a comment line
%!*\ 1) Deduce the file sequence and calculate 2theta step size
DEDUCE
#START_FILE
#END_FILE
CALC
#SCAN_BINS
#MAX_ANGLE
/
VARIABLE
#STEP_2THETA
```

```
EXIT
%!*\ 4) Initialize data and set up experiments
CREATE DATA
3450
3450
EXCHANGE
CREATE DATA
3450
3450
GEOMETRY
KEYBOARD
#X_BEAMCENTER
#Y_BEAMCENTER
#WAVELENGTH
#SAM2DET
#X_PIXELSIZE
#Y_PIXELSIZE
#TILT_ROTATION
#TILT_ANGLE
0.0
%!*\ 5) Read in all data and add them, then divide by number of files
DO #COUNT = ##START, ##END, ##STEP
%!*\ Get MAR_FILE by patching different variables
I2C
#COUNT
NO
##NUM_CHARS
```

```
#CVALUE
CONCATENATION
##PREFIX
#CVALUE
#MAR_FILE
CONCATENATION
#MAR_FILE
##EXTENSION
#MAR_FILE
%!*\ Read in the data file
INPUT DATA
MAR RESEARCH FORMAT
#MAR_FILE
%!*\ Add it to the memory
ADD
EXCHANGE
END DO
%!*\ Make the memory to be the current data
EXCHANGE
%!*\ Calculate number of files
CALC
##START
##END
-
##STEP
/
1/X
```

```
1
+
VARIABLE
#NUM_FILES
EXIT
CDIVIDE
#NUM_FILES
%!*\ 6) Using powder diffraction to integrate the data
FIT
%!*\ 7) Threshold masking of the data, greater than mask
THRESHOLD MASKING
NO
64000.00
POWDER
YES
#X_BEAMCENTER
#Y_BEAMCENTER
#X_PIXELSIZE
#Y_PIXELSIZE
#SAM2DET
#TILT_ROTATION
#TILT_ANGLE
%!*\ Input polarization factor?
YES
#POLARIZATION_FACTOR
%!*\ Lorentzian correction?
PARTIAL POWDER
```

```
%!*\ NONE
%!*\ YES: Euqal angle pixel scan, NO: Equal radial distance
YES
#STEP_2THETA
%!*\ Correct spatial distortion?
NO
%!*\ No to "save powder diffraction data standard file"
NO
%!*\ Exit fit submenu
EXIT
EXCHANGE
OUTPUT
CHI
#CHI_FILE
%!*\ Output rows?
YES
1
OUTPUT
GSAS
#GSAS_FILE
YES
1
EXIT
YES
```

Instead of passing the variable values from the keyboard, a setup file can be used, and is shown below. The meaning of each field is noted by the comments on the same line. Basically, this file contains all the information necessary to integrate the image

plate data. We can simply add more and more data to the list of data to the end.

```
#  Setup for automation of MAR3450 file integration
#  Format:
#   1) You can insert comment lines at any place, starting with "#"
#   2) NO space should be left before the parameter values
#   3) When commenting on the same line, at least ONE space should
#       be left between parameter value and its comment
#  Written by Xiangyun on 07/23/2003
3450                                    # x dimension
3450                                    # y dimension
0.126514                                # X-ray wavelength
0.94                                    # Polarization factor
179.4899                                # Sample to detector distance
100.0                                   # X pixel size
100.0                                   # Y pixel size
1720.870                                # X beam center
1705.101                                # Y beam center
7.866515                                # Tilt rotation angle
0.0234912                               # Tilt angle
44.0                                    # Max angle
3450                                    # Number of points
#
CsIFR6_426_annealed3d_001.mar3450   # Start file to read
CsIFR6_426_annealed3d_007.mar3450   # End file to read
CsIFR6_426_annealed3d.gsa           # GSAS file to save
CsIFR6_key_p-90.chi                 # CHI file  to save
```

The batch FIT2D data integration is initiated by command *mar_integrate.sh* <

setup-file-name under the directory containing all the raw data. The SHELL script *mar_integrate.sh* reads the setup file to extract the parameter values, then calls FIT2D with the macro file and proper variable values. One additional operation in the script is to comment out the first four lines in the integrated CHI files, in order to make it directly readable by the data visualization program KUPLOT [196].

A.4.3 Normalization by the monitor counts

The last step of this preprocessing before using PDFgetX2 is to normalize the data. This is very important because sample and background are usually measured with different exposure time. Even with the same exposure time, the incident beam intensities most likely are still different during the self-decay and re-filling process of the synchrotron storage ring, as well as the unpredictable slight fluctuations. The normalization constant should be the incident beam monitor closest to the sample. There should be no *beam size defining* slits/collimation's after this monitor, otherwise its reading doesn't reflect the real incident beam intensity on the sample. In the case of multiple image plate data being averaged, the corresponding total monitor counts should also be averaged, i.e. divided by the number of data files (exposures). Finishing this, we are ready to use PDFgetX2 to obtain the PDFs.

A.4.4 Additional corrections to the RA-PDF data

The RA-PDF data collection is much quicker (three to four orders of magnitude faster) and requires a simpler experimental setup. However, the data analysis becomes more difficult, in addition to the extra steps to integrate the image plate data. The characteristics of the image plate detector requires some additional corrections, as well as the high background levels. We will focus on two aspects, the lack of energy resolution and the energy dependent response.

Estimation of standard deviations Proper estimation of the standard deviations

(ESD) and their propagation along the data corrections are rather important, as the experimental PDFs are commonly used in least square regression programs for structure refinement [197, 198]. For X-ray photon counting detectors, the ESD of the observed count (after dead time correction) is simply its square root when the count is large (more than a few hundreds). However, the IP detector is not a photon counter. Quite a few experimental factors contribute to the relative uncertainties of IP response, such as the read-out system, and the non-uniformity of the IP, etc. [49, 52]. To complicate the situation, in the published literatures, the ESD is calculated with respect to the noise level of the IP system under study [54, 55]. Fig. A.2 shows the ESD of the IP response as a function of exposure level. It was found that the relative ESD of the IP response is rather close to an ideal photon counter at low exposure levels, while it saturates to a little less than 1% at high exposure levels. The IP response relative to the noise is found to be close to 1-2 per incident photon at the high energies of our interest. Therefore, based on the specifications of the IP system in our experiment (Mar345, sensitivity of 1 X-ray photon per ADC-unit at 8 keV, intrinsic noise 1-2 photon equivalents), we approximate the ESD of each pixel count to be the larger value between its square root and its one hundredth.

Once the ESD of each pixel is determined, we can propagate the ESD through the integration from the two dimensional raw image and geometric corrections. However, program FIT2D does not generate/propagate ESDs, and only gives the two column data: intensity versus the scattering angle 2θ. Thus we need to correctly retrace the procedure done in FIT2D to obtain proper ESDs. The steps are the following. The integrated data from FIT2D are the averaged intensities among the pixels within each bin grid corrected by the geometric factor. As each pixel has the same area, the geometric factor is simply $\cos^3(2\theta)$.

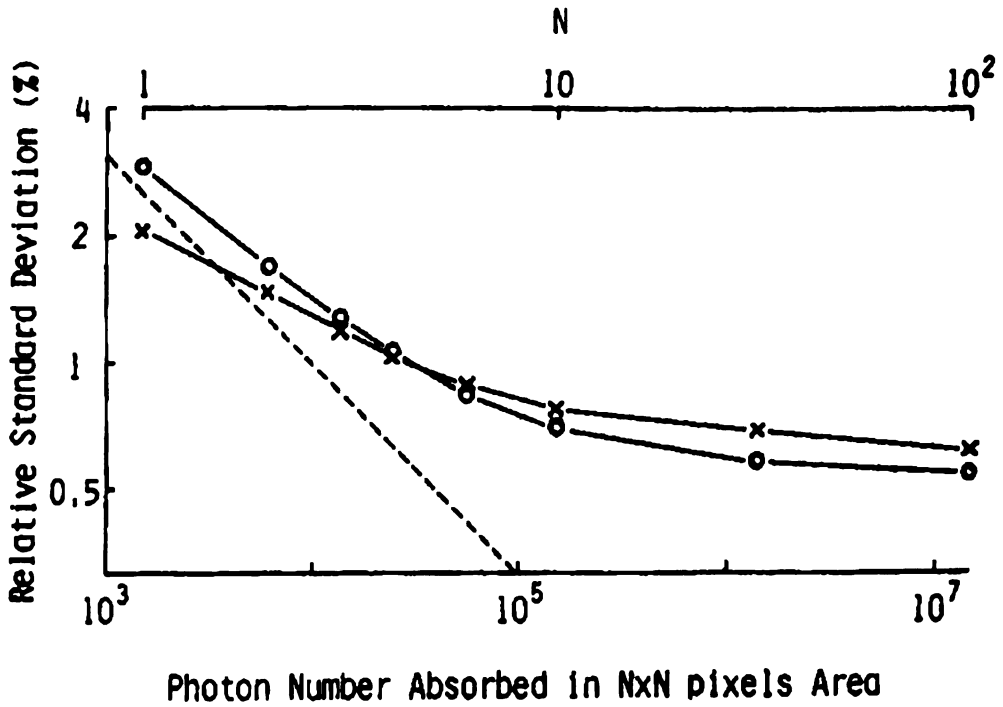

Figure A.2: Estimated relative standard deviations of the IP response among areas of $N \times N$ pixels as a function of photon number absorbed in the area. The scale of N is shown in the upper part. Open circles are for the drum scanner and crosses for BAS2000. Dashed lines represent the relative standard deviation of the photon number absorbed in the area. Taken from [55].

So the first step is to multiply the intensities by $\cos^3(2\theta)$ to get the averaged total counts. Then, we need to compute the number of pixels in each bin grid. For the scattering angle bin width of $\delta 2\theta$, the area for this bin on the IP is approximately $2\pi d^2 \sin(2\theta)/\cos^3(2\theta) \cdot \delta 2\theta$, where d is the sample to detector distance. Dividing the area by each pixel size gives the number of pixels. Given the integrated count c, pixel area A_{pixel}, we obtain

$$ESD = \frac{\sqrt{c \cdot \cos^3(2\theta)}}{\sqrt{2\pi d^2 \sin(2\theta)/\cos^3(2\theta) \cdot \delta 2\theta / A_{pixel}/\cos^3(2\theta)}}, \qquad \text{(A.2)}$$

noting that $\sqrt{c \cdot \cos^3(2\theta)}$ should be replaced by $0.01 \cdot c \cdot \cos^3(2\theta)$ if the latter is larger due to the 1% saturation of relative uncertainties of the IP.

Oblique incident angle This correction accounts for the angular dependence of the scattered photon effective path length in the IP phosphor layer [60], as a direct result of its incomplete absorption of the scattered photons. This correction becomes very significant at high X-ray energies and large incident angles (both present in the RA-PDF experiments). Two parameters are used here. The scattered photon absorption coefficient of the IP phosphor layer and the incident angle (equal to 2θ). The X-ray energy used in our experiments is highly penetrating with the absorption coefficient less than 1%.

Compton intensities at high Q and fluorescence The image plate counts only give the detected X-ray intensities, with no knowledge of the energy of the X-ray. The lack of energy resolution makes it impossible to distinguish between elastic, Compton, and fluorescent photons. This poses rather serious problems to PDF analysis. Early use of image plates to collect diffraction data reached Q_{max} less than 13.0 Å^{-1} [199, 57, 58]. In the low Q region, elastic scattering is usually the strongest signal, thus removal of the parasitic Compton and fluorescence intensities doesn't introduce much error into the analysis. However, elastic scattering decays exponentially with Q; Compton intensity increases with Q; and fluorescent intensity is constant. As a consequence, in the high Q region ($Q_{max} \geq$ 30.0 Å^{-1}), the situation is quite different. For example, even the case of Ni (Z=28) atoms, the Compton scattering is about 4 times as large as the elastic scattering at Q = 30 Å^{-1}. This ratio increases with decreasing Z values. The fluorescent intensities can be effectively suppressed by going to higher incident X-ray energies for low Z elements or just below the edge for high Z elements. However, for the medium to high Z elements, the currently routinely achievable highest energy X-rays still give rather significant fluorescent intensities. Therefore, the extraction of elastic signal in the high Q region is not a trivial task. Small errors on the estimation of Compton or fluorescent

intensities would result in significant deviations to the elastic signal. Another complication is the statistical uncertainty of the extracted elastic intensities, as the uncertainty of both Compton and fluorescent intensities will be added to it. To achieve the same counting statistics as when measuring elastic scattering separately, the total counts from the image plate would have to be $\sim n^2$ times as many (if elastic scattering accounts for $1/n$ of the total intensities).

Energy dependence of the IP response Due to the detection mechanism of the image plate, X-rays with the same number of photons but different energies will result in different counts. Though elastic scattering has the same energy at all Q values, the energy of Compton scattering decreases with increasing Q and the fluorescence intensities usually comprise of several characteristic energy lines. The high Q region data again are sensitive to this effect due to the dominating Compton and/or fluorescent intensities. This energy dependent detection efficiency is not a simple linear function, and in fact is difficult to measure accurately. In program PDFgetX2, either a linear or quadratic empirical formula is used as the energy dependence of the image plate detection efficiency while ensuring the detection efficiency decreases with increasing X-ray energy.

The obtain PDF, $G(r)$, is in a compatible file format for the PDF refinement program PDFFIT [11]. Please refer to the user's guide of the program PDFgetX2 [195] for details.

Bibliography

[1] B. E. Warren, **X-ray diffraction**, *X-ray diffraction*, Dover, New York, 1990.

[2] W. H. Bragg, **X-rays and crystals**, Nature (London) **90**, 219 (1913).

[3] W. H. Bragg, **The specular reflection of X-rays**, Nature (London) **90**, 410 (1913).

[4] W. H. Bragg, **The distribution of the electrons in atoms**, Nature (London) **95**, 344 (1915).

[5] T. Egami and S. J. L. Billinge, **Underneath the Bragg peaks: structural analysis of complex materials**, *Underneath the Bragg peaks: structural analysis of complex materials*, Pergamon Press, Elsevier, Oxford, England, 2003.

[6] E. A. Stern, D. E. Sayers, and F. W. Lytle, **Extended X-ray-absorption fine-structure technique. III. Determination of physical parameters**, Phys. Rev. B **11**, 4836–46 (1975).

[7] R. Prinz and D. Koningsberger, editors, **X-ray absorption: principles, applications techniques of EXAFS, SEXAFS and XANES**, *X-ray absorption: principles, applications techniques of EXAFS, SEXAFS and XANES*, J. Wiley and Sons, New York, 1988.

[8] R. K. Harris, **Nuclear magnetic resonance spectroscopy**, *Nuclear magnetic resonance spectroscopy*, Pitman, London, 1983.

[9] P. Debye, **Dispersion of Rövrtöntgen rays**, Annalen der Physik (Berlin, Germany) **46**, 809–823 (1915).

[10] X. Qiu, E. S. Božin, P. Juhas, T. Proffen, and S. J. L. Billinge, **Reciprocal space instrumental effects on the real space neutron atomic pair distribution function**, J. Appl. Crystallogr. **37**, 110–116 (2004).

[11] Th. Proffen and S. J. L. Billinge, **PDFFIT, a program for full profile structural refinement of the atomic pair distribution function**, J. Appl. Crystallogr. **32**, 572–575 (1999).

[12] L. P. Tarasov and B. E. Warren, **X-ray diffraction study of liquid sodium**, J. Chem. Phys. **4**, 236–8 (1936).

[13] B. E. Warren, H. Krutter, and O. Morningstar, **Fourier analysis of X-ray patterns of vitreous SiO_2 and B_2O_3**, J. Am. Ceram. Soc. **19**, 202–6 (1936).

[14] R. Kaplow, B. L. Averbach, and S. L. Strong, **Pair correlations in solid lead near the melting temperature**, J. Phys. Chem. Solids **25**, 1195 (1964).

[15] H. Ocken and C. N. J. Wagner, **Temperature dependence of the structure of liquid indium**, Phys. Rev. **149**, 122–130 (1966).

[16] S. J. L. Billinge and M. G. Kanatzidis, **Beyond crystallography: the study of disorder, nanocrystallinity and crystallographically challenged materials**, Chem. Commun. , 749–760 (2004).

[17] Th. Proffen, S. J. L. Billinge, T. Egami, and D. Louca, **Structural analysis of complex materials using the atomic pair distribution function - a practical guide**, Z. Kristallogr. **218**, 132–143 (2003).

[18] S. J. L. Billinge, **Real-space rietveld: full profile structure refinement of the atomic pair distribution function**, in *Local Structure from Diffraction*, edited by S. J. L. Billinge and M. F. Thorpe, page 137, New York, 1998, Plenum.

[19] I-K. Jeong, Th. Proffen, F. Mohiuddin-Jacobs, and S. J. L. Billinge, **Measuring correlated atomic motion using X-ray diffraction**, J. Phys. Chem. A **103**, 921–924 (1999).

[20] I. K. Jeong, R. H. Heffner, M. J. Graf, and S. J. L. Billinge, **Lattice dynamics and correlated atomic motion from the atomic pair distribution function**, Phys. Rev. B **67**, 104301 (2003).

[21] Th. Proffen, V. Petkov, S. J. L. Billinge, and T. Vogt, **Chemical short range order obtained from the atomic pair distribution function**, Z. Kristallogr. **217**, 47 (2002).

[22] S. J. L. Billinge, **Local atomic structure and superconducivity of $Nd_{2-x}Ce_xCuO_{4-y}$: a pair distribution function study**, Ph.D Thesis,, 1992.

[23] S. J. L. Billinge, R. G. DiFrancesco, G. H. Kwei, J. J. Neumeier, and J. D. Thompson, **Direct observation of lattice polaron formation in the local structure of $La_{1-x}Ca_xMnO_3$**, Phys. Rev. Lett. **77**, 715–718 (1996).

[24] E. S. Božin, S. J. L. Billinge, H. Takagi, and G. H. Kwei, **Neutron diffraction evidence of microscopic charge inhomogeneities in the CuO_2 plane of superconducting $La_{2-x}Sr_xCu_4$ ($0 \leq x \leq 0.30$)**, Phys. Rev. Lett. **84**, 5856–5859 (2000).

[25] E. S. Božin, S. J. L. Billinge, G. H. Kwei, and H. Takagi, **Charge-stripe ordering from local octahedral tilts: underdoped and superconducting $La_{2-x}Sr_xCuO_4$ ($0 \leq x \leq 0.3$)**, Phys. Rev. B **59**, 4445 (1999).

[26] E. S. Božin, S. J. L. Billinge, and G. H. Kwei, **Reexamination of the second order structural phase transition in $La_{2-x}A_xCuO_4$ (A=Ba,Sr)**, Physica B **241-243**, 795 (1998).

[27] V. Petkov, S. J. L. Billinge, T. Vogt, A. S. Ichimura, and J. L. Dye, **Structure of intercalated Cs in zeolite ITQ-4: an array of metal ions and electrons confined in a pseudo-1D nanoporous host**, Phys. Rev. Lett. **89**, 075502 (2002), (Highlighted in Phys. Rev. Focus: http://focus.aps.org/story/v10/st4).

[28] V. Petkov, P. N. Trikalitis, E. S. Bozin, S. J. L. Billinge, T. Vogt, and M. G. Kanatzidis, **Structure of $V_2O_5.nH_2O$ xerogel solved by the atomic pair distribution function technique**, J. Am. Chem. Soc. **124**, 10157 (2002).

[29] V. Petkov, S. J. L. Billinge, P. Larson, S. D. Mahanti, T. Vogt, K. K. Rangan, and M. G. Kanatzidis, **Structure of nanocrystalline materials using atomic pair distribution function analysis: study of $LiMoS_2$**, Phys. Rev. B **65**, 092105 (2002).

[30] V. Petkov, S. J. L. Billinge, J. Heising, and M. G. Kanatzidis, **Application of atomic pair distribution function analysis to materials with intrinsic disorder. Three-dimensional structure of exfoliated-restacked WS_2: not just a random turbostratic assembly of layers**, J. Am. Chem. Soc. **122**, 11571 (2000).

[31] K. Furukawa, **The radial distribution curves of liquids by diffraction methods**, Rep. Prog. Phys. **25**, 395–440 (1962).

[32] A. Wright, **Diffraction studies of glass structure: the first 70 years**, Glass Physics and Chemistry **24**, 148–179 (1998).

[33] V. Petkov, S. J. L. Billinge, S. D. Shastri, and B. Himmel, **Polyhedral units and network connectivity in calcium aluminosilicate glasses from high energy X-ray diffraction**, Phys. Rev. Lett. **85**, 3436 (2000).

[34] I.-K. Jeong, F. Mohiuddin-Jacobs, V. Petkov, S. J. L. Billinge, and S. Kycia, **Local structure study of $In_xGa_{1-x}As$ semiconductor alloys using high energy synchrotron X-ray diffraction**, Phys. Rev. B **63**, 205202 (2001).

[35] P. F. Peterson, Th. Proffen, I.-K. Jeong, S. J. L. Billinge, K.-S. Choi, M. G. Kanatzidis, and P. G. Radaelli, **Local atomic strain in $ZnSe_{1-x}Te_x$ from high real space resolution neutron pair distribution function measurements**, Phys. Rev. B **63**, 165211 (2001).

[36] R. L. McGreevy and P. Zetterstrom, **To RMC or not to RMC? The use of reverse Monte Carlo modelling**, Curr. Opin. Solid St. M. **7**, 41–47 (2003).

[37] M. G. Tucker, M. T. Dove, and D. A. Keen, **Application of the reverse Monte Carlo method to crystalline materials**, J. Appl. Crystallogr. **34**, 630–638 (2001).

[38] M. G. Tucker, M. P. Squires, M. T. Dove, and D. A. Keen, **Dynamic structural disorder in cristobalite: neutron total scattering measurement and reverse Monte Carlo modelling**, J. Phys.-Condens. Mat. **13**, 403–423 (2001).

[39] A. K. Soper, **Tests of the empirical potential structure refinement method and a new method of application to neutron diffraction data on water**, Mol. Phys. **99**, 1503–1516 (2001).

[40] A. K. Soper, **The radial distribution functions of water and ice from 220 to 673 K and at pressures up to 400 MPa**, Chem. Phys. **258**, 121–137 (2000).

[41] X. Qiu, J. W. Thompson, and S. J. L. Billinge, **PDFgetX2: a GUI driven program to obtain the pair distribution function from X-ray powder diffraction data**, J. Appl. Crystallogr. **37**, 678 (2004).

[42] P. F. Peterson, M. Gutmann, Th. Proffen, and S. J. L. Billinge, **PDFgetN: a user-friendly program to extract the total scattering structure function and the pair distribution function from neutron powder diffraction data**, J. Appl. Crystallogr. **33**, 1192–1192 (2000).

[43] Th. Proffen, T. Egami, S. J. L. Billinge, A. K. Cheetham, D. Louca, and J. B. Parise, **Building a high resolution total scattering powder diffractometer - upgrade of NPD at MLNSC**, Appl. Phys. A **74**, s163–s165 (2002).

[44] I.-K. Jeong, J. Thompson, A. M. P. Turner, and S. J. L. Billinge, **PDFgetX: a program for determining the atomic pair distribution function from X-ray powder diffraction data**, J. Appl. Crystallogr. **34**, 536 (2001).

[45] O. Stachs, T. Gerber, and V. Petkov, **An image plate chamber for X-ray diffraction experiments in Debye-Scherrer geometry**, Rev. Sci. Instrum. **71**, 4007 (2000).

[46] K. Takahashi, **Progress in science and technology on photostimulable BaFX : Eu^{2+} (X = Cl, Br, I) and imaging plates**, Journal of Luminescence **100**, 307–315 (2002).

[47] H. Vonseggern, T. Voigt, W. Knupfer, and G. Lange, **Physical model of photostimulated luminescence of X-ray-irradiated BaFBr:Eu^{2+}**, J. Appl. Phys. **64**, 1405–1412 (1988).

[48] K. Takahashi, K. Kohda, J. Miyahara, Y. Kanemitsu, K. Amitani, and S. Shionoya, **Mechanism of photostimulated luminescence in BaFCl$^-$$Eu^{2+}$, BaFBr$^-$$Eu^{2+}$ phosphors**, Journal Of Luminescence **31-2**, 266–268 (1984).

[49] Y. Amemiya, **Imaging plates for use with synchrotron-radiation**, J. Synchrotron Rad. **2**, 13–21 (1995).

[50] Y. Iwabuchi, C. Umemoto, K. Takahashi, and S. Shionoya, **Photostimulated luminescence process in $BaFBr^{-}Eu^{2+}$ containing $F(Br^{-})$ and $F(F^{-})$ centers**, Journal of Luminescence **48-9**, 481–484 (1991).

[51] J. Miyahara, K. Takahashi, Y. Amemiya, N. Kamiya, and Y. Satow, **A new type of X-ray area detector utilizing laser stimulated luminescence**, Nucl. Instrum. Methods A **246**, 572–578 (1986).

[52] Y. Amemiya, T. Matsushita, A. Nakagawa, Y. Satow, J. Miyahara, and J. Chikawa, **Design and performance of an imaging plate system for X-ray-diffraction study**, Nucl. Instrum. Methods A **266**, 645–653 (1988).

[53] Y. Amemiya, S. Kishimoto, T. Matsushita, Y. Satow, and M. Ando, **Imaging plate for time-resolved X-ray measurements**, Rev. Sci. Instrum. **60**, 1552–1556 (1989).

[54] D. Bourgeois, J. Moy, S. Svensson, and A. Kvick, **The point-spread function of X-ray image-intensifiers CCD-camera and imaging-plate systems in crystallography - assessment and consequences for the dynamic-range**, J. Appl. Crystallogr. **27**, 868–877 (1994).

[55] M. Ito and Y. Amemiya, **X-ray-energy dependence and uniformity of an imaging plate detector**, Nuclear Instruments & Methods In Physics Research Section A-Accelerators Spectrometers Detectors And Associated Equipment **310**, 369–372 (1991).

[56] W. A. Crichton, M. Mezouar, T. Grande, S. Stolen, and A. Grzechnik, **Breakdown of intermediate-range order in liquid $GeSe_2$ at high pressure**, Nature **414**, 622 (2001).

[57] M. Mezouar, P. Faure, W. Crichton, N. Rambert, B. Sitaud, S. Bauchau, and G. Blattmann, **Multichannel collimator for structural investigation of liquids and amorphous materials at high pressures and temperatures**, Rev. Sci. Instrum. **73**, 3570 (2002).

[58] M. J. Kramer, M. F. Besser, N. Yang, E. Rozhkova, D. J. Sordelet, Y. Zhang, and P. L. Lee, **Devitrification studies of Zr-Pd and Zr-Pd-Cu metallic glasses**, J. Non-Cryst. Solids **317**, 62–70 (2003).

[59] M. A. Estermann and W. Steurer, **Diffuse scattering data acquisition techniques**, Phase Transit. **67**, 165–195 (1998).

[60] J. Zaleski, G. Wu, and P. Coppens, **On the correction of reflection intensities recorded on imaging plates for incomplete absorption in the phosphor layer**, J. Appl. Crystallogr. **31**, 302 (1998).

[61] P. J. Chupas, X. Qiu, J. C. Hanson, P. L. Lee, C. P. Grey, and S. J. L. Billinge, **Rapid acquisition pair distribution function analysis (RA-PDF)**, J. Appl. Crystallogr. **36**, 1342–1347 (2003).

[62] S. D. Shastri, K. Fezzaa, A. Mashayekhhi, W.-K. Lee, P. B. Fernandez, and P. L. Lee, **Cryogenically cooled bent double-Laue monochromator for high-energy undulator X-rays (50-200 KeV)**, J. Synchrotron Rad. **9**, 317 (2002).

[63] A. P. Hammersley, S. O. Svenson, M. Hanfland, and D. Hauserman, **Two-dimensional detector software: from real detector to idealised image or two-theta scan**, High Pressure Res. **14**, 235–248 (1996).

[64] A. P. Hammersley, **FIT2D v9.129 reference manual v3.1**, ESRF Internal Report **ESRF98HA01T** (1998).

[65] P. J. Chupas, M. F. Ciraolo, J. C. Hanson, and C. P. Grey, ***in-situ* X-ray diffraction and solid-state NMR study of the fluorination of γ-Al_2O_3 with HCF_2Cl**, J. Am. Chem. Soc. **123**, 1694 (2001).

[66] N. Kim and C. P. Grey, **Probing Oxygen Motion in Disordered Anionic Conductors with ^{17}O and ^{51}V MAS NMR Spectroscopy**, Science **297**, 1317 (2002).

[67] G. Wu, B. L. Rodrigues, and P. Coppens, **The correction of reflection intensities for incomplete absorption of high-energy X-rays in the CCD phospher**, J. Appl. Crystallogr. **35**, 356 (2002).

[68] A. C. Larson and R. B. Von Dreele, **General Structure Analysis System**, Report No. LAUR-86-748, Los Alamos National Laboratory, Los Alamos, NM 87545, 1987.

[69] P. Daniel, A. Bulou, M. Rousseau, J. Noue, J. L. Fourquet, M. Leblanc, and R. Burriel, **A study of the structural phase transitions in AlF_3: X-ray powder diffraction, DSC and Raman scattering investigations of the lattice dynamics and phonon spectrum**, J. Phys.-Condens. Mat. **2**, 5663 (1990).

[70] J. Yan and M. Greenblatt, **Ionic conductivities of $Bi_4V_{2-x}M_xO_{11-x/2}$ (M = Ti, Zr, Sn, Pb) solid solutions**, Solid State Ionics **81**, 225–33 (1995).

[71] P. Norby and J. C. Hanson, **Hydrothermal synthesis of the microporous aluminophosphate $CoAPO_5$; *in-situ* time-resolved synchrotron x-ray powder diffraction studies**, Catal. Today **39**, 301–309 (1998).

[72] Th. Proffen and R. B. Neder, **DISCUS: a program for diffuse scattering and defect-structure simulation**, J. Appl. Crystallogr. **30**, 171–175 (1997).

[73] G. H. Jonker and J. H. van Santen, **Ferromagnetic compounds of manganese with perovskite structure**, Physica (Amsterdam) **16**, 337–49 (1950).

[74] J. H. van Santen and G. H. Jonker, **Electrical conductivity of ferromagnetic compounds of manganese with perovskite structure**, Physica (The Hague) **16**, 599–600 (1950).

[75] C. Zener, **Interaction between the d shells in the transition metals**, Phys. Rev. **81**, 440–444 (1951).

[76] C. Zener, **Interaction between the d-shells in the transition metals. II. Ferromagnetic compounds of manganese with perovskite structure**, Phys. Rev. **82**, 403–405 (1951).

[77] C. Zener, **Interaction between the d-shells in the transition metals. III. Calculation of the Weiss factors in Fe, Co, and Ni**, Phys. Rev. **83**, 299–301 (1951).

[78] P. W. Anderson and H. Hasegawa, **Considerations on double exchange**, Phys. Rev. **100**, 675–81 (1955).

[79] E. O. Wollan and W. C. Koehler, **Neutron-diffraction study of the magnetic properties of the series of perovskite-type compounds $(La_{1-x},Ca_x)MnO_3$**, Phys. Rev. **100**, 545–63 (1955).

[80] P. Schiffer, A. P. Ramirez, W. Bao, and S.-W. Cheong, **Low temperature magnetoresistance and the magnetic phase diagram of $La_{1-x}Ca_xMnO_3$**, Phys. Rev. Lett. **75**, 3336 (1995).

[81] J. B. Goodenough, **Theory of the role of covalence in the perovskite-type manganites [La,M(II)]MnO_3**, Phys. Rev. **100**, 564–573 (1955).

[82] J. Kanamori, **Crystal distortion in magnetic compounds**, J. Appl. Phys. **31**, 14S–23S (1960).

[83] J. Kanamori, **Electron correlation and ferromagnetism of transition metals**, Progr. Theoret. Phys. (Kyoto) **30**, 275–89 (1963).

[84] A. H. Morrish, B. J. Evans, J. A. Eaton, and L. K. Leung, **Ionic ferromagnet (La,Pb)MnO_3. I. Growth and characteristics of single crystals**, Canadian Journal of Physics **47**, 2691–6 (1969).

[85] C. W. Searle and S.-T. Wang, **Ionic ferromagnet (La,Pb)MnO_3. III. Ferromagnetic resonance studies**, Canadian Journal of Physics **47**, 2703–8 (1969).

[86] C. W. Searle and S.-T. Wang, **Ionic ferromagnet (La,Pb)MnO_3. V. Electric transport and ferromagnetic properties**, Canadian Journal of Physics **48**, 2023–31 (1970).

[87] J. Volger, **Further experimental investigations on some ferromagnetic oxide compounds of manganese with perovskite structure**, Physica (The Hague) **20**, 49–66 (1954).

[88] R. M. Kusters, J. Singleton, D. A. Keen, R. McGreevy, and W. Hayes, **Mgnetoresistance measurements on the magnetic semiconductor $NdPbMnO_3$**, Physica B **155**, 362 (1989).

[89] R. von Helmolt, J. Wecker, B. Holzapfel, L. Schultz, and K. Samwer, **Giant negative magnetoresistance in perovskitelike $La_{2/3}Ba_{1/3}MnO_x$ ferromagnetic-films**, Phys. Rev. Lett. **71**, 2331 (1993).

[90] K. Chahara, T. Ohno, M. Kasai, and Y. Kozono, **Magnetoresistance in magnetic manganese oxide with intrinsic antiferromagnetic spin structure**, Appl. Phys. Lett. **63**, 1990 (1993).

[91] H. L. Ju, C. Kown, Q. Li, R. L. Greene, and T. Venkatesan, **Giant magnetoresistance in $La_{1-x}Sr_xMnO_z$ films near room temperature**, Appl. Phys. Lett. **65**, 2108–10 (1994).

[92] S. Jin, T. H. Tiefel, M. McCormack, R. A. Fastnacht, R. Ramesh, and L. H. Chen, **Thousandfold change in resistivity in magnetoresistive La-Ca-Mn-O films**, Science (Washington, DC, United States) **264**, 413–15 (1994).

[93] G.-Q. Gong, C. Canedy, G. Xiao, J. Z. Sun, A. Gupta, and W. J. Gallagher, **Colossal magnetoresistance of 1,000,000-fold magnitude achieved in the antiferromagnetic phase of $La_{1-x}Ca_xMnO_3$**, Appl. Phys. Lett. **67**, 1783–5 (1995).

[94] A. J. Millis, P. B. Littlewood, and B. I. Shraiman, **Double Exchange alone does not explain the resistivity of $La_{1-x}Sr_xMnO_3$**, Phys. Rev. Lett. **74**, 5144 (1995).

[95] J.-H. Park, C. T. Chen, S.-W. Cheong, W. Bao, G. Meigs, V. Chakarian, and Y. U. Idzerda, **Electronic aspects of the ferromagnetic transition in manganese perovskites**, Phys. Rev. Lett. **76**, 4215–4218 (1996).

[96] A. J. Millis, B. I. Shraiman, and R. Müller, **Dynamic Jahn-Teller effect and colossal magnetoresistance in $La_{1-x}Sr_xMnO_3$**, Phys. Rev. Lett. **77**, 175 (1996).

[97] M. Quijada, J. ˇ Cerne, J. R. Simpson, H. D. Drew, K. H. Ahn, A. J. Millis, R. Shreekala, R. Ramesh, M. Rajeswari, and T. Venkatesan, **Optical conductivity of manganites: crossover from Jan-Teller small polaron to coherent transport in the ferromagnetic state**, Phys. Rev. B **58**, 16093 (1998).

[98] S. Satpathy, Z. S. Popović, and F. R. Vukajlović, **Electronic structure of the perovskite oxides: $La_{1-x}Ca_xMnO_3$**, Phys. Rev. Lett. **76**, 960–3 (1996).

[99] E. Dagotto, G. Alvarez, S. L. Cooper, A. L. Cornelius, A. Feiguin, J. Fernandez-Baca, D. Gibbs, J. P. Hill, and T. Hotta, **Nanoscale phase separation and colossal magnetoresistance**, *Nanoscale phase separation and colossal magnetoresistance*, Springer-Verlag, Amsterdam, 2003.

[100] D. S. Dessau and Z.-X. Shen, **Colossal magnetoresistance oxides**, *Colossal magnetoresistance oxides*, chapter 5, Gordon & Breach, New York, 1999.

[101] T. Arima, Y. Tokura, and J. Torrance, **Variation of optical gaps in perovskite-type 3D transition-metal oxides**, Phys. Rev. B **48**, 17006–17009 (1993).

[102] T. Arima, Y. Tokura, and S. Uchida, **Optical-Spectra of $Pr_{2-X}Ce_xCUO_{4-\delta}$ Crystals - Evolution of in-Gap States With Electron Doping**, Phys. Rev. B **48**, 6597–6603 (1993).

[103] T. Saitoh, A. Bocquet, T. Mizokawa, and A. Fujimori, **Systematic variation of the electronic-structure of 3D transition-metal compounds**, Phys. Rev. B **52**, 7934–7938 (1995).

[104] A. Bocquet, T. Mizokawa, T. Saitoh, H. Namatame, and A. Fujimori, **Electronic-structure of 3D-transition-metal compounds by analysis of the 2P core-level photoemission spectra**, Phys. Rev. B **46**, 3771–3784 (1992).

[105] H. Y. Hwang, S.-W. Cheong, P. G. Radaelli, M. Marezio, and B. Batlogg, **Lattice effects on the magnetoresistance in doped $LaMnO_3$**, Phys. Rev. Lett. **75**, 914 (1995).

[106] J. J. Neumeier, M. F. Hundley, J. D. Thompson, and R. H. Heffner, **Substantial pressure effects on the electrical-resistivity and ferromagnetic transition-temperature of $La_{1-x}Ca_xMnO_3$**, Phys. Rev. B **52**, R7006 (1995).

[107] T. Hotta, A. Feiguin, and E. Dagotto, **Stripes induced by orbital ordering in layered manganites**, Phys. Rev. Lett. **86**, 4922 (2001).

[108] T. Hotta, S. Yunoki, M. Mayr, and E. Dagotto, **A-type antiferromagnetic and C-type orbital-ordered state in $LaMnO_3$ using cooperative Jahn-Teller phonons**, (1999), Unpublished. preprint avaialable at http://xxx.lanl.gov/abs/cond-mat/9907034.

[109] J. F. Mitchell, D. N. Argyriou, C. D. Potter, D. G. Hinks, J. D. Jorgensen, and S. D. Bader, **Structural phase diagram of $La_{1-x}Sr_xMnO_{3-\delta}$: Relationship to magnetic and transport properties**, Phys. Rev. B **54**, 6172 (1996).

[110] A. P. Ramirez, **Colossal magnetoresistance**, J. Phys.-Condens. Mat. **9**, 8171 (1997).

[111] M. B. Salamon and M. Jaime, **The physics of manganites: structure and transport**, Rev. Mod. Phys. **73**, 583–628 (2001).

[112] S-W. Cheong and H. Y. Hwang, **Ferromagnetism vs. charge/orbital ordering in mixed-valent manganites**, in *Colossal Magnetoresistant Oxides*, Gordon and Breach, 1999.

[113] M. Roy, J. F. Mitchell, A. P. Ramirez, and P. Schiffer, **Doping-induced transition from double exchange to charge order in $La_{1-x}Ca_xMnO_3$ near $x = 0.5$**, unpublished, 1998.

[114] S. J. L. Billinge, **Polarons in manganites: now you see them, now you don't**, in *Physics of Manganites*, edited by T. A. Kaplan and S. D. Mahanti, page 201, Klewer Academic/Plenum, New York, 1999.

[115] M. Uehara, B. Kim, and S.-W. Cheong, **Phase digram of $La_{1-x}Ca_xMnO_3$**, 2000, personal communication.

[116] J. S. Zhou, J. B. Goodenough, A. Asamitsu, and Y. Todura, **Pressure induced polaronic to itinerant electronic transition in $La_{1-x}Sr_xMnO_3$ crystals**, Phys. Rev. Lett. **79**, 3234 (1997).

[117] R. Senis, V. Laukhin, B. Martínez, J. Fontcuberta, X. Obradors, A. A. Arsenov, and Y. M. Mukovskii, **Pressure and magnetic-field effects on charge ordering in $La_{0.9}Sr_{0.1}MnO_3$**, Phys. Rev. B **57**, 14680 (1998).

[118] H. Y. Hwang, T. T. M. Palstra, S.-W. Cheong, and B. Batlogg, **Pressure effects on the magnetoresistance in doped manganese perovskites**, Phys. Rev. B **52**, 15046–9 (1995).

[119] M. G. Gutmann, E. S. Bozin, S. J. L. Billinge, N. A. Babushkina, L. M. Belova, A. R. Kaul, and O. Y. Gorbenko, **Temperature evolution of the local atomic structure in oxygen isotope substituted $Pr_{0.525}La_{0.175}Ca_{0.3}MnO_3$**, Appl. Phys. A **74**, 892 (2002).

[120] J. P. Franck, I. Isaac, W. Chen, J. Chrzanowski, and J. C. Irwin, **Oxygen-isotope effect of the paramagnetic-insulating to ferromagnetic-metallic transition in $La_{1-x}Ca_xMnO_3$**, Phys. Rev. B **58**, 5189 (1998).

[121] N. A. Babushkina, L. M. Belova, O. Yu. Gorbenko, A. R. Kaul, A. A. Bosak, V. I. Ozhogin, and K. I. Kugel, **Metal-insulator transition induced by oxygen isotope exchange in the magnetoresistive perovskite manganites**, Nature **391**, 159 (1998).

[122] G. M. Zhao, M. B. Hunt, and H. Keller, **Strong oxygen-mass dependence of the thermal expansion coefficient in the manganites $(La_{1-x}Ca_x)_{1-y}Mn_{1-y}O_3$**, Phys. Rev. Lett. **78**, 955 (1997).

[123] A. M. Balagurov, V. Yu Pomjakushin, D. V. Sheptyakov, V. L. Aksenov, N. A. Babushkina, L. M. Belova, A. H. Taldenkov, A. V. Inyushkin, P. Fischer, M. Gutmann, L. Keller, O. Yu Gorbenko, and A. R. Kaul, **Effect of oxygen isotope substitution on magnetic structure of $(La_{0.25}Pr_{0.75})_{0.7}Ca_{0.3}MnO_3$**, Phys. Rev. B **60**, 383 (1999).

[124] G. Zhao, K. Conder, H. Keller, and K. A. Müller, **Giant oxygen isotope shift in the magnetoresistive perovskite $La_{1-x}Ca_xMnO_{3+y}$**, Nature **381**, 676 (1996).

[125] N. A. Babushkina, L. M. Belova, V. I. Ozhogin, O. Y. Gorbenko, A. R. Kaul, A. A. Bosak, D. I. Khomskii, and K. I. Kugel, **Metal-insulator transition induced by isotope exchange in colossal magnetoresistance manganites**, J. Appl. Phys. **83**, 7369 (1998).

[126] J. Rodríguez-Carvajal, M. Hennion, F. Moussa, A. H. Moudden, L. Pinsard, and A. Revcolevschi, **Neutron diffraction study of the Jahn-Teller distortion in stoichiometric $LaMnO_3$**, Phys. Rev. B **57**, R3189 (1998).

[127] Th. Proffen, R. G. DiFrancesco, S. J. L. Billinge, E. L. Brosha, and G. H. Kwei, **Measurement of the local Jahn-Teller distortion in $LaMnO_{3.006}$**, Phys. Rev. B **60**, 9973 (1999).

[128] A. J. Millis, **Cooperative Jahn-Teller effect and electron-phonon coupling in $La_{1-x}A_xMnO_3$**, Phys. Rev. B **53**, 8434 (1996).

[129] E. Araya-Rodriguez, A. Y. Ramos, H. C. N. Tolentino, E. Granado, and S. B. Oseroff, **Local distortion in $LaMnO_3$ across the Jahn-Teller transition**, J. Magn. Magn. Mater. **233**, 88–90 (2001).

[130] M. C. Sánchez, G. Subías, J. García, and J. Blasco, **Cooperative Jahn-Teller phase transition in $LaMnO_3$ studied by X-ray absorption spectroscopy**, Phys. Rev. Lett. **90** (2003).

[131] E. Granado, J. A. Sanjurjo, C. Rettori, J. J. Neumeier, and S. B. Oseroff, **Order-disorder in the Jahn-Teller transition of $LaMnO_3$: a Raman scattering study**, Phys. Rev. B **62**, 11304–11307 (2001).

[132] J.-S. Zhou and J. B. Goodenough, **Paramagnetic phase in single-crystal $LaMnO_3$**, Phys. Rev. B **60**, R15002–R15004 (1999).

[133] M. Tovar, C. Alejandro, A. Butera, A. Caneiro, M. T. Causa, F. Prado, and R. D. Sánchez, **ESR and magnetization in Jahn-Teller-distorted $LaMnO_{3+\delta}$: correlation with crystal structure**, Phys. Rev. B **60**, 10199–10205 (1999).

[134] T. Chatterji, F. Fauth, B. Ouladdiaf, P. Mandal, and B. Ghosh, **Volume collapse in $LaMnO_3$ caused by an orbital order-disorder transition**, Phys. Rev. B **68** (2003).

[135] P. G. Radaelli, G. Iannone, M. Marezio, H. Y. Hwang, S.-W. Cheong, J. D. Jorgensen, and D. N. Argyriou, **Structural effects on the magnetic and transport properties of perovskite $A_{1-x}A'_xMnO_3$ (x =0.25, 0.30)**, Phys. Rev. B **56**, 8265 (1997).

[136] P. Norby, I. G. Krogh, Andersen, E. Krogh Andersen, and N. H. Andersen, **The crystal structure of lanthanum manganate(III), $LaMnO_3$, at room temperature and at 1273 K under N_2**, J. Solid State Chem. **119**, 191–6 (1995).

[137] M. F. Thorpe, V. A. Levashov, M. Lei, and S. J. L. Billinge, **Notes on the analysis of data for pair distribution functions**, in *From semiconductors to proteins: beyond the average structure*, edited by S. J. L. Billinge and M. F. Thorpe, pages 105–128, New York, 2002, Kluwer/Plenum.

[138] M. F. Thorpe, J. S. Chung, S. J. L. Billinge, and F. Mohiuddin-Jacobs, **Advances in pair distribution profile fitting in alloys**, in *Local Structure from Diffraction*, edited by S. J. L. Billinge and M. F. Thorpe, page 157, New York, 1998, Plenum.

[139] T. Chatterji, B. Ouladdiaf, P. Mandal, B. Bandyopadhyay, and B. Ghosh, **Jahn-Teller transition in $La_{1-x}Sr_xMnO_3$ in the low-doping region ($0 < x \leq 0.1$)**, Phys. Rev. B **66**, 054403/1–054403/8 (2002).

[140] G. Matsumoto, **$(La_{1-x}Ca_x)MnO_3$. I. Magnetic structure of $LaMnO_3$**, J. Phys. Soc. Jpn **29**, 606–15 (1970).

[141] G. Matsumoto, **$(La_{1-x}Ca_x)MnO_3$. II. Magnetic properties**, J. Phys. Soc. Jpn **29**, 615–22 (1970).

[142] X. Qiu and S. J. L. Billinge, **PDF form factor – probe the intermediate range structure**, J. Appl. Crystallogr. (2004), unpublished.

[143] J.-S. Zhou, H. Q. Yin, and J. B. Goodenough, **Vibronic superexchange in single-crystal $LaMn_{1-x}Ga_xO_3$**, Phys. Rev. B **63**, 184423/1–184423/5 (2001).

[144] J.-S. Zhou and J. B. Goodenough, **Orbital order-disorder transition in single-valent manganites**, Phys. Rev. B **68** (2003).

[145] J.-S. Zhou and J. B. Goodenough, **Exchange interactions in the perovskites $Ca_{1-x}Sr_xMnO_3$ and $RMnO_3$ (R=La,Pr,Sm)**, Physical Review B: Condensed Matter and Materials Physics **68**, 054403/1–054403/7 (2003).

[146] Y. Moritomo, A. Asamitsu, H. Kuwahara, and Y. Tokura, **Giant magnetoresistance of manganese oxides with a layered perovskite structure.**, Nature (London) **380**, 141–4 (1996).

[147] J. Mitchell, D. Argyriou, A. Berger, K. Gray, R. Osborn, and U. Welp, **Spin, charge, and lattice states in layered magnetoresistive oxides**, J. Phys. Chem. B **105**, 10731–10745 (2001).

[148] A. J. Millis, **Lattice effects in magnetoresistive manganese perovskites**, Nature **392**, 147 (1998).

[149] M. Kubota, H. Fujioka, K. Ohoyama, K. Hirota, Y. Moritomo, and H. Yoshizawa, **Neutron scattering studies on magnetic structure of teh double-layered manganite $La_{2-2x}Sr_{1+2x}Mn_2O_7$ (0.30≤x≤0.50)**, J. Phys. Chem. Solids **60**, 1161 (1999).

[150] C. Ling, J. Millburn, J. Mitchell, D. Argyriou, J. Linton, and H. Bordallo, **Interplay of spin and orbital ordering in the layered colossal magnetoresistance manganite $La_{2-2x}Sr_{1+2x}Mn_2O_7$ (0.5≤x≤1.0)**, Phys. Rev. B **62**, 15096–15111 (2000).

[151] T. Kimura, Y. Tomioka, H. Kuwahara, A. Asamitsu, M. Tamura, and Y. Tokura, **Interplane tunneling magnetoresistance in a layered manganite crystal**, Science (Washington, D. C.) **274**, 1698–1701 (1996).

[152] C. H. Chen and S.-W. Cheong, **Commensurate to incommensurate charge ordering and its real-space images in $La_{0.5}Ca_{0.5}MnO_3$**, Phys. Rev. Lett. **76**, 4042 (1996).

[153] M. Kubota, H. Yoshizawa, Y. Moritomo, H. Fujioka, K. Hirota, and Y. Endoh, **Interplay of the CE-type charge ordering and the A-type spin ordering in half-doped bilayer manganite $LaSr_2Mn_2O_7$**, J. Phys. Soc. Jpn **68**, 2202 (1999).

[154] D. N. Argyriou, H. N. Bordallo, B. J. Campbell, A. K. Cheetham, D. E. Cox, J. S. Gardner, K. Hanif, A. dos Santos, and G. F. Strouse, **Charge ordering and phase competition in the layered perovskite $LaSr_2Mn_2O_7$.**, Phys. Rev. B **61**, 15269–15276 (2000).

[155] T. Kimura, R. Kumai, Y. Tokura, J. Q. Li, and Y. Matsui, **Successive structural transitions coupled with magnetotransport properties in $LaSr_2Mn_2O_7$**, Phys. Rev. B **58**, 11081–11084 (1998).

[156] Y. Tokura, H. Kuwahara, Y. Moritomo, Y. Tomioka, and A. Asamitsu, **Competing instabilities and metastable states in $(Nd,Sm)_{1/2}Sr_{1/2}MnO_3$**, Phys. Rev. Lett. **76**, 3184–7 (1996).

[157] J. B. Goodenough, **Magnetism and the chemical bond**, *Magnetism and the chemical bond*, J. Wiley and Sons, New York, 1963.

[158] T. Akimoto, Y. Moritomo, K. Ohoyama, S. Okamoto, S. Ishihara, S. Maekawa, and A. Nakamura, **Interrelation between orbital polarization and magnetic structure in bilayer manganites**, Phys. Rev. B **59**, 14153 (1999).

[159] R. Maezono and N. Nagaosa, **Complex orbital state in manganites**, Phys. Rev. B **62**, 11576–11580 (2000).

[160] Y. Murakami, J. P. Hill, D. Gibbs, M. Blume, I. Koyama, M. Tanaka, H. Kawata, T. Arima, Y. Tokura, K. Hirota, and Y. Endoh, **Resonant x-ray scattering from orbital ordering in $LaMnO_3$**, Phys. Rev. Lett. **81**, 582–585 (1998).

[161] H. Kuwahara, T. Okuda, Y. Tomioka, A. Asamitsu, and Y. Tokura, **Two-dimensional charge-transport and spin-valve effect in the layered antiferromagnet $Nd_{0.45}Sr_{0.55}MnO_3$**, Phys. Rev. Lett. **82**, 4316 (1999).

[162] D. Louca, G. H. Kwei, and J. F. Mitchell, **Local lattice effects in the layered manganites $La_{1.4}Sr_{1.6}Mn_2O_7$**, Phys. Rev. Lett. **80**, 3811 (1998).

[163] J. E. Millburn, J. F. Mitchell, and D. N. Argyriou, **Extending the $n = 2$ Ruddlesden-Popper solid solution $La_{2-2x}Sr_{1+2x}Mn_2O_7$ beyond $x = 0.5$: synthesis of Mn^{4+}-rich compounds**, Chem. Commun. **3**, 1389 (1999).

[164] J. Medvedeva, V. Anisimov, O. Mryasov, and A. Freeman, **The role of Coulomb correlation in magnetic and transport properties of doped manganites: $La_{0.5}Sr_{0.5}MnO_3$ and $LaSr_2Mn_2O_7$**, J. Phys.-Condens. Mat. **14**, 4533–4542 (2002).

[165] P. G. Radaelli, D. E. Cox, M. Marezio, S.-W. Cheong, P. E. Schiffer, and A. P. Ramirez, **Simultaneous structural, magnetic, and electronic transitions in $La_{1-x}Ca_xMnO_3$ with $x = 0.25$ and 0.5**, Phys. Rev. Lett. **75**, 4488 (1995).

[166] B. Campbell, D. Argyriou, J. Mitchell, R. Osborn, B. Ouladdiaf, and C. Ling, **Enhanced stability of charge and orbital order in $La_{0.78}Sr_{2.22}Mn_2O_7$**, Phys. Rev. B **69**, 104403 (2004).

[167] Y. Moritomo, T. Akimoto, A. Nakamura, K. Ohoyama, and M. Ohashi, **Antiferromagnetic metallic state in the heavily doped region of perovskite manganites**, Phys. Rev. B **58**, 5544 (1998).

[168] S. Okamoto, S. Ishihara, and S. Maekawa, **Orbital structure and magnetic ordering in layered manganites: universal correlation and its mechanism**, Phys. Rev. B **6310**, 104401–6 (2001).

[169] J. B. A. A. Elemans, B. Van Laar, K. R. Van der Veen, and B. O. Loopstra, **Crystallographic and magnetic structures of $La_{1-x}Ba_xMn_{1-x}M_xO_3$ (M= manganese or titanium)**, J. Solid State Chem. **3**, 238–42 (1971).

[170] S. J. L. Billinge, Th. Proffen, V. Petkov, J. Sarrao, and S. Kycia, **Evidence for charge localization in the ferromagnetic phase of $La_{1-x}Ca_xMnO_3$ from high real-space-resolution X-ray diffraction**, Phys. Rev. B **62**, 1203 (2000).

[171] S. J. L. Billinge, **Strain, nano-phase separation, multi-scale structures and function of advanced materials**, in *Intrinsic Multiscale Structure and*

Dynamics of Complex Electronic Oxides, edited by S. Shenoy and A. R. Bishop, pages 25 – 40, Singapore, 2003, World Scientific.

[172] X. Qiu, , S. J. L. Billinge, and J. F. Mitchell, **Orbital occupancy transition in $La_{2-2x}Sr_{1+2x}Mn_2O_7$ at $x = 0.54$**, (2003), unpublished.

[173] K. E. Gray and J. F. Mitchell, unpublished.

[174] S. Derakhshan, A. Assoud, E. Dashjav, X. Qiu, S. J. L. Billinge, and H. Kleinke, **Planar nets of Ti atoms comprising squares and rhombs in the new binary antimonide Ti_2Sb**, J. Am. Chem. Soc. **126**, 8295–8302 (2004).

[175] H. Kleinke and B. Harbrecht, **Combining the structure controlling factors for metal-rich compounds to a structure map**, Zeitschrift Fur Anorganische und Allgemeine Chemie **626**, 1851–1853 (2000).

[176] C. Lee, E. Dashjav, and H. Kleinke, **Structure prediction using our semiempirical structure map: the crystal structure of the new arsenide ZrTiAs**, Chem. Mater. **13**, 4053–4057 (2001).

[177] E. Dashjav, C. Lee, and H. Kleinke, **Crystal structure predictions: the crystal and electronic structure of $Zr_{1-\delta}V_{1+\delta}As$**, J. Solid State Chem. **169**, 96–102 (2002).

[178] P. J. Chupas, C. P. Grey, J. C. Hanson, J.-Y. Kim, J. Rodriguez, X. Qiu, S. J. Billinge, and P. L. Lee, **In-situ time resolved powder diffaction studies in heterogenous catalysis; coupling the study of long range and local structural changes**, Commission on Powder Diffraction Newsletter, International Union of Crystallography , 24–25 (2003).

[179] J. M. Thomas and W. J. Thomas, **Principles and practice of heterogeneous catalysis**, Chemistry & Industry (London) , 952, 954 (1997).

[180] J. A. Rodriguez, J. Y. Kim, J. C. Hanson, M. Perez, and A. I. Frenkel, **Reduction of CuO in H_2: *in situ* time-resolved XRD studies**, Catalysis Letters **85**, 247–254 (2003).

[181] P. J. Chupas, S. Chaudhuri, J. C. Hanson, X. Qiu, P. L. Lee, S. D. Shastri, S. J. L. Billinge, and C. P. Grey, **Probing local and long-range structure simultaneously: an in-situ study of the high-temperature phase transition of α-AlF_3**, J. Am. Chem. Soc. **126**, 4756–4757 (2004).

[182] X. Qiu, S. J. L. Billinge, C. R. Kmety, and J. F. Mitchell, **Evidence for nanoscale inhomogeneities in bilayer manganites in the Mn^{4+} rich region: $0.54 \leq x \leq 0.80$**, J. Phys. Chem. Solids **65**, 1423–1429 (2004).

[183] J. Li, C. Dong, L. Liu, and Y. Ni, **Reentrant charge-ordering transition and phase separation in the layered perovskite $La_{2-2x}Sr_{1+2x}Mn_2O_7$**, Phys. Rev. B **6417**, 4413 (2001).

[184] J. Q. Li, Y. Matsui, T. Kimura, and Y. Tokura, **Structural properties and charge-ordering transition in $LaSr_2Mn_2O_7$**, Phys. Rev. B **57**, 3205 (1998).

[185] J. Dho, W. Rim, H. Choi, E. Chi, and N. Hur, **Re-entrant charge-ordering behaviour in the layered manganites $La_{2-2x}Sr_{1+2x}Mn_2O_7$**, J. Phys.-Condens. Mat. **13**, 3655–3663 (2001).

[186] V. Petkov, I-K. Jeong, J. S. Chung, M. F. Thorpe, S. Kycia, and S. J. L. Billinge, **High real-space resolution measurement of the local structure of $Ga_{1-x}In_xAs$ using X-ray diffraction**, Phys. Rev. Lett. **83**, 4089 (1999).

[187] C. W. Dwiggins, Jr and D. A. Park, **Calculation of the intensity of secondary scattering of X-rays by non-crystalline materials**, Acta Crystallogr. A **27**, 264 (1971).

[188] C. W. Dwiggins, Jr, **Calculation of the intensity of secondary scattering of X-rays by non-crystalline materials. II. Moving sample transmission geometry**, Acta Crystallogr. A **28**, 155 (1972).

[189] R. Serimaa, T. Pitkanen, S. Vahvaselka, and T. Paakkari, **Multiple scattering of X-rays in the case of isotropic samples**, J. Appl. Crystallogr. **23**, 11 (1990).

[190] S. I. Zabinsky, A. Ankudinov, J. J. Rehr, and R. C. Albers, **Multiple scattering calculations of X-ray absorption spectra**, Phys. Rev. B **52**, 2995 (1995).

[191] D. Waasmaier and A. Kirfel, **New analytical scattering factor functions for free atoms and ions**, Acta Crystallogr. A **51**, 416 (1995).

[192] B. J. Thijsse, **The accuracy of experimental radial distribution functions for metallic glasses**, J. Appl. Crystallogr. **17**, 61 (1984).

[193] W. Ruland, **The separation of coherent and incoherent Compton X-ray scattering**, Brit. J. Appl. Phys. **15**, 1301 (1964).

[194] H. H. M. Balyuzi, **Analytic approximations to incoherently scattered X-ray intensities**, Acta Crystallogr. A **A31**, 600–2 (1975).

[195] X. Qiu and S. J. L. Billinge, *PDFgetX2 user's guide*, Michigan State University, Department of Physics and Astronomy, v1.0 edition, 2004.

[196] Th. Proffen, R. B. Neder, and S. J. L. Billinge, **Teaching diffraction using computer simulations over the internet**, J. Appl. Crystallogr. **34**, 767 (2001).

[197] B. H. Toby and T. Egami, **Accuracy of pair distribution function analysis applied to crystalline and noncrystalline materials**, Acta Crystallogr. A **A48**, 336–46 (1992).

[198] B. H. Toby and S. J. L. Billinge, **Determination of standard uncertainties in fits to pair distribution functions**, Acta Cryst. A **60**, 315–317 (2004), to be published.

[199] G. Wu, B. L. Rodrigues, and P. Coppens, **The correction of reflection intensities for incomplete absorption of high-energy X-rays in the CCD phospher**, Nature **35**, 356 (2002).